DISSERTATION

submitted to the

COMBINED FACULTY OF

NATURAL SCIENCES AND MATHEMATICS

OF THE

RUPERTO-CAROLA-UNIVERSITY OF HEIDELBERG,

GERMANY

FOR THE DEGREE OF

DOCTOR OF NATURAL SCIENCES

PUT FORWARD BY

DIPL. PHYS. LUKAS KONSTANDIN

BORN IN: VÖLKLINGEN, GERMANY

ORAL EXAMINATION: 16 OCTOBER 2014

Understanding the statistical properties of supersonic turbulence in hydrodynamic simulations

REFEREES:

PROF. DR. RALF S. KLESSEN

PROF. DR. MATTHIAS BARTELMANN

Für Angelika

Abstract

Turbulence is a dominant feature operating in gaseous flows in a variety of systems, from aerodynamics to highly compressible media common in astrophysical environments. We present a systematic analysis of the influence of different forcing types on the statistical properties of supersonic, isothermal turbulence in both the Lagrangian and Eulerian frameworks. We study a series of high-resolution, hydrodynamical grid simulations and examine the effects of solenoidal (divergence-free) and compressive (curl-free) forcing as well as varying root mean square Mach numbers on the parameters describing the statistical state of the system. The probability density functions of the gas density, velocity, and the velocity increments are measured. Structure functions and power spectra are investigated to quantify the two-point correlation properties of compressible turbulence. We find that the mode of the forcing mechanism has an influence on the all measurements mentioned above. Compressively driven simulations show a more intermittent behaviour, a larger fractal dimension of the most dissipative structures (Chapter 4), a significantly larger density contrast with more pronounced wings of the density PDF (Chapter 5), and steeper power spectra with a decreased influence of the bottleneck effect (Chapter 6), at the same root mean square Mach number.

Zusammenfassung

Turbulenz ist ein wichtiges Phänomen in unterschiedlichen Gasen, von Aerodynamik bis hin zu stark komprimierbaren Medien, welche häufig in astrophysikalischen Zusammenhängen auftreten. Diese Arbeit umfasst eine systematische Studie über den Einfluss von verschiedenen Kraftfeldern auf die statistischen Eigenschaften von isothermer Überschallturbulenz im Lagrange- und Eulerbezugssystem. Wir analysieren eine Reihe von hoch aufgelösten, hydrodynamischen Gitter-Simulationen und bestimmen den Einfluss von quellenfreien (divergenzfreien) und komprimierenden (rotationsfreien) Kraftfeldern, sowie von verschiedenen quadratischen Mitteln der Machzahl, auf die Parameter, die den statistischen Zustand des Systems beschreiben. Die Wahrscheinlichkeitsdichtefunktion der Massendichte, der Geschwindigkeit, als auch der Geschwindigkeitsinkremente werden gemessen. Strukturfunktionen und Leistungsspektren werden untersucht, um die Eigenschaften der Zweipunktkorrelation von Überschallturbulenz zu quantifizieren. Wir zeigen, dass die Art des Kraftfeldes einen Einfluss auf alle gerade genannten Größen hat. Die komprimierend getriebenen Simulationen zeigen ein intermittenteres Verhalten, eine größere fraktale Dimension der dissipativen Strukturen (Kapitel 4), erheblich größere Dichtekontraste mit ausgeprägteren Flanken in der Wahrscheinlichkeitsverteilung der Massendichte (Kapitel 5), und steileren Leistungsspektren mit einem verringerten Flaschenhalseffekt (Kapitel 6) bei gleichem quadratischen Mittel der Machzahl.

List of publications

The following publications are presented in this thesis

1. **Konstandin, L.**; Federrath, C.; Klessen, R. S., Schmidt, W.:
   Statistical properties in supersonic turbulence in the Lagrangian and
   Eulerian frameworks, 2012 , *J. Fluid Mech.*, 692, 183

2. **Konstandin, L.**; Girichidis, P.; Federrath, C.; Klessen, R. S.:
   A new density variance-Mach number relation for subsonic and super-
   sonic isothermal turbulence, 2012 , ApJ, 761, 149

3. **Konstandin, L.**; Shetty, R.; Girichidis, P.; Klessen, R. S.:
   Hierarchical Bayesian analysis of the velocity power-spectrum in super-
   sonic turbulence , 2014 , submitted to MNRAS

The following publications were performed in collaborations

4. Girichidis, P.; **Konstandin, L.**; Whitworth, A.; Klessen, R. S.:
   On the Evolution of the Density Probability Density Function in Strongly
   Self-gravitating Systems, 2014, ApJ, 781, 2

5. Shetty, R.; Kelly, B.; Rahman, N.; Bigiel, F.; Bolatto, A.; Clark, P.;
   Klessen, R. S.; **Konstandin, L.**:
   Indications of a sub-linear and non-universal Kennicutt-Schmidt rela-
   tionship, 2014 , MNRAS, 437, 61-65

6. Bertram, E.; **Konstandin, L.**; Shetty, R.; Glover, S.; Klessen, R. S.:
   Centroid Velocity Statistics of Molecular Clouds, submitted to MNRAS

Contents

Chapter 1

Introduction

Richard Feynman once declared that turbulence is "the most important unsolved problem in classical physics", even tough the appearance of turbulent motions is quite common, present in everyday life such as in the rise of smoke from a cigarette, the air flow passing a runner, the water flow behind a water gate. Yet, a mathematical description of turbulence has been elusive for many years, inspiring Richard Feynman to make his statement.

The cornerstone of the theory was formulated by Kolmogorov (1941a,b) treating fully developed, incompressible turbulence. The intermittency problem of this theory was considered in the seventies by himself (Kolmogorov, 1962), and later by the famous work of Mandelbrot (1972), leading to the intermittency model of She and Leveque (1994), which is still the most successful model describing the stochastic occurrence of the energy transfer and dissipation events with a log-Poisson distribution (Birnir, 2013). The experimental investigation of turbulence was also rapidly evolving during this period starting with the analysis of atmospheric turbulence with only few measuring probes (Gurvitch, 1960), over wind tunnel experiments (Gagne and Hopfinger, 1979), to the advanced and most recent analysis of the "French washing machine" (Mordant et al., 2005). This experiment creates a turbulent flow in a cylindrical container filled with water driven by two counter-rotating disks. The full 3D velocity information gets extracted from the Doppler shift measured by ultrasonic transducers using small, solid particles in the flow. In the nineties the rapid development of the computer technology facilitated the analysis of turbulence in numerical simulations, providing huge datasets.[1] Different approaches can be made for simulating or modelling turbulence, including direct numerical simulations (DNS), large eddies simu-

---

[1] Richardson et al. (1922) developed a mathematical technique for systematically forecasting the weather. It took him three months to predict the weather for the next 24 hours.

lation (LES), turbulent viscosity models (k-ϵ model), Reynold stress models, and probability density function (PDF) methods (Pope, 2000).

Despite of all these developments Richard Feynman's quote still holds and an holistic theory is still missing. For example, the theoretical description of turbulences uses the assumption of a constant density field and therefore only considers velocity fields with $\boldsymbol{\nabla} \cdot \mathbf{v} = 0$. Analytic results without these assumptions are still rare. Just recently Galtier and Banerjee (2011) and Banerjee and Galtier (2013) derived analytically scaling relations for the mass weighted structure functions. Because of difficulties in creating compressible turbulence with a significant varying density field for experiments, astrophysical observations and numerical simulations are the only data sources for analysing fully developed supersonic turbulence. In this thesis we focus on the latter.

The goal of this thesis is to understand fully developed supersonic turbulence, occurring in many astrophysical contexts, by performing direct numerical simulations. We focus on supersonic turbulence present in Giant Molecular Clouds (GMC) yielding a filamentary, hierarchical density field varying over many orders of magnitude and influencing the statistical properties of the star formation process (e.g. the fragmentation degree, the initial mass function, star formation rate).

1.1   Motivation of this Study

> *"One must still have chaos in oneself to be able to give birth to a dancing star."*
>
> Friedrich Nietzsche
> Thus spoke Zarathustra
> A book for all and none
>
> Nietzsche (1883)

The night sky is the astrophysical stage for the cosmic play. The main theme reappearing through the whole plot is the fragmentation and the subsequent collapse of gas due to self-gravity determining the shape and structure over all observable scales. This process leads to a hierarchical clustering of mass starting from the largest scales with galaxy clusters, down to individual galaxies, the interstellar medium (ISM), giant molecular clouds (GMCs), star clusters, protostellar cores, and planets on the smallest scales. In distinct scenes different physical processes adopt the dominant role and exhibit their character. However, our vision of the cosmic play unfolding in front of us is quite limited, where light particles are nearly the only information carrier reaching us

and telling us the storyline. As most observed photons are emitted by stars, a solid understanding of star formation and stellar evolution process, as well as the subsequent interaction of these photons with their environment is essential in nearly all astrophysical disciplines. This ties the properties of stars to the observation of various astrophysical topics and shows the importance of a comprehensive understanding of these objects. Stars are also born in the gas and dust of the interstellar medium (ISM) and the obstetricians are gravity and turbulence dominating the gravo-turbulent fragmentation process. Turbulence plays here a double role, on one side it prevents the collapse of clouds on the GMC scales, visible in the turbulent pressure term, while on the other side, it promotes collapse on the small scales, compressing and collecting large amount of gas by supersonic shocks and is then responsible for the statistical occurrence of star formation.

Stars and clusters of stars are formed in molecular clouds (MC), which are cold (10-20 [K]), dense objects ($\sim 100\,[cm^{-3}]$), enabling the transition from a monatomic composition of the interstellar gas to the molecular one by self-shielding against the background radiation field. Dust works as a catalyst for converting hydrogen into H_2 molecules. H_2 forms primarily on the surface of dust grains and gets destroyed by far ultraviolet (FUV) radiation. The equilibrium abundance of H_2 is therefore controlled by the external FUV radiation field and the local density attenuating it (see Glover and Mac Low, 2007a,b, for a fully time-dependent chemo-dynamical simulation of the GMC formation process). The complete CO survey[2] of the whole Milkyway by Dame et al. (1987, 2001) revealed the large spatial extent of GMCs and their substantial contribution to the mass budget of the ISM. The mass of individual MCs range from $\sim 10^2 M_\odot$ for small clouds above the galactic plane to $\sim 10^7 M_\odot$ in the central molecular zone of the galaxy. GMC have a complex, clumpy and filamentary internal structure such that their mass-density probability distribution function (PDF) spans orders of magnitude (Schneider et al., 2013). Even tough, the mass of different clouds can vary by five orders of magnitude and also internal structure can span orders of magnitude, their surface densities are similar and vary only by factors of a few, $\Sigma \sim 40 - 170 M_\odot\, pc^{-2}$. This is known as one of the famous Larson's laws Larson (1981). A typical GMC with the above given density, temperature, and bulk velocity of $\sim 1\,[\mathrm{km\,s^{-1}}]$, has a Reynolds number of $\sim 10^9$ on the dissipation scale $\sim 0.1 AU$ (see Section 4.2 Dobbs et al., 2013). This high Reynolds number guarantees that the gas motions inside a molecular cloud are turbulent and measurements of the velocity disper-

---

[2]As CO requires even more shielding as H_2 their abundances are correlated and CO can be used as a tracer.

sion indicate Mach numbers of $\sim$ 5–50 (Elmegreen and Scalo, 2004; Scalo and Elmegreen, 2004). These supersonic motions create a turbulent pressure $p = \rho\sigma_v^2$ capable of counteracting gravitational collapse. The virial parameter, which describes the large-scale dynamics of the gas in GMCs, is defined as $\alpha_G = M_{virial}/M_{GMC}$, is a useful guide to predict the evolution of GMCs, where $M_{virial} = 5\sigma_v^2 R/G$. Using the Larson laws $\Sigma_{GMC}(R) \approx const$ and $\sigma_v(R) \propto R^{0.5}$ results in a constant virial parameter $\alpha_G \approx 1$ indicating that GMCs are marginally gravitationally bound objects.

The dynamical properties of the MC, e.g. the supersonic motions ubiquitously observed, have a direct influence on the star formation process (Mac Low and Klessen, 2004; McKee and Ostriker, 2007). The physical properties of the MCs depend on the creation mechanisms, which are still under debate. The main theories describe GMC formation with gravitational instability, localised converging flows, spiral arm induced collisions, magneto-Jeans instability, or Parker instability (for a detailed discussion of the formation processes see Section 3 in Dobbs et al., 2013, and references therein). These formation mechanism have to explain the GMC clumpy and filamentary internal structure and the origin of the non-thermal motions.

It is well known that turbulence decays in a dynamical time scale in the absence of external energy input. What mechanism is driving the turbulent velocities in GMCs is still under debate: (a) The large velocity dispersions are caused by the global gravitational collapse rather than random turbulent motions (Ballesteros-Paredes et al., 2011a,b; Hartmann et al., 2012). (b) This scenario explains the turbulent motions with internal sources of energy, like H II regions, radiation pressure, protostellar outflows, or other feedback mechanism (Dekel and Krumholz, 2013; Krumholz et al., 2014). (c) An alternative explanation is that GMCs are driven externally. Klessen (2011) argues with different processes of cloud formation that drives the internal motions by setting up a turbulent cascade transporting kinetic energy from large to small scales. These processes are diverse and range from accretion flows of extragalactic gas falling on the galactic disc, converging flows of atomic gas triggered by spiral density waves, to supernova explosions. However, GMCs are embedded in a galactic flow, where cloud-cloud collisions in spiral arms or close encounters with shear can also drive the turbulent motions externally. Most likely, all these mechanism play a role and which one is dominating depends on the individual cloud. But, with the scenario (a) one cannot explain the relatively long lifetimes of GMCs ($\gtrsim$ 20 Myr) in comparison to the free-fall time[3] and the inverse P-Cygni line is absent, which is a typical feature of

---

[3]The same argument can be done with the galaxy-average low star formation efficiency or the low galaxy-average star formation rate.

large-scale collapse. Scenario (b) has also two caveats, Brunt (2003); Heyer and Brunt (2004); Brunt et al. (2009) study the principal component analysis, a method to measure the two-point correlation properties of the velocity field similar to structure functions. They find no break in the scaling relations on large scales and concluded that the mechanism driving the turbulent motions in GMCs must operate on scales comparable to the size of the cloud or larger. In addition, there is no correlation between the star formation rate and the strength of the turbulent motions inside molecular clouds (e.g. the Magdalena cloud or the Pipe nebula indicate a low star formation rate, but a significant amount of turbulence (Klessen, 2011)), which one would expect for this scenario.

We close this section with a short sketch of the star formation process. A review about star formation studies in numerical simulations can be found in Klessen et al. (2011) and detailed description of star formation theories and observations can be found (Mac Low and Klessen, 2004; McKee and Ostriker, 2007), who discuss also the importance of magnetic fields creating an additional pressure counteracting the gravitationally collapse. The picture we propose follows mainly this presented in Klessen (2011). Molecular clouds form in the stagnation points of large-scale converging flows. Therefore, the density goes up and shields the gas against the background radiation field. Molecules form and enable the gas to cool efficiently reinforcing the creation of the dense, cool cloud. As the time scale of the large-scale converging flow goes like $T \sim L/V(L)$, L and V are the scale and the velocity of the converging flow, it delivers fresh material and the cloud grows in mass over an extended time. The gravitational collapse, which also sets in, together with the kinetic energy of the converging flow cascade to smaller scales driving the turbulent motions in the cloud. Figure 1.1 (Figure 2, from Klessen, 2011) illustrates the kinetic energy cascade in the context of star formation. We know that the Mach number in an isothermal gas scales linearly with the standard deviation of its density distribution (see Chapter 5 for a detailed discussion). For example a typical cloud with averaged number densities ~ 100 [cm^{-3}] and a Mach number of ~ 30 reaches over-densities of $\sim 10^5$ [cm^{-3}], so a density contrast of $\sim 10^3$. If we zoom in a high-density and cluster forming core with 10^4 [cm^{-3}] we still observe Mach numbers of ~ 5 and therefore still expect high density variation. By chance some of these fluctuations may exceed the critical mass for gravitational collapse such that further fragmentation sets in resulting in a multi stellar population, instead of forming one high-mass star. At even smaller scales the kinetic energy spectrum is so low, that the average turbulent motions are below the sound speed. Therefore they cannot produce over-densities any more and further gravoturbulent fragmentation stops.
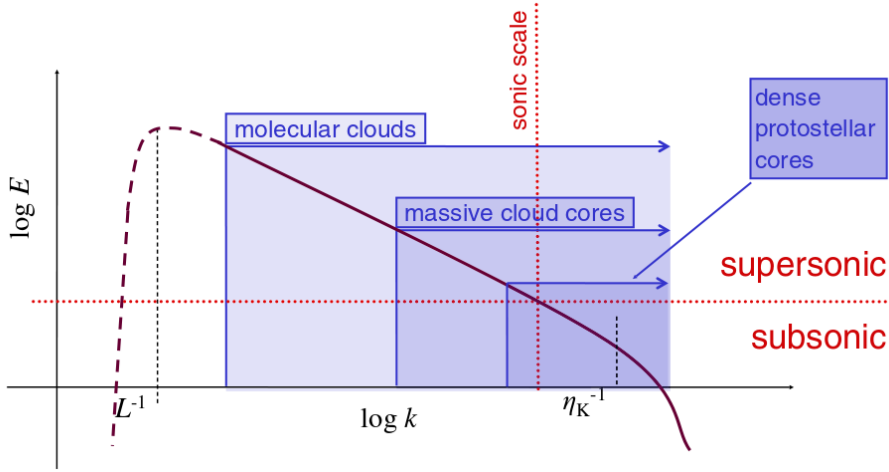
Figure 1.1: Cartoon of the kinetic energy density spectrum as a function of the wave number k with the relation to different cloud structures. The turbulent motions are driven on the larger scales in comparison to the cloud size L and dissipated on the very small scales η_K. (*Figure 2, from* Klessen, 2011)

1.2   Overview of this Study

We analyse different sets of numerical experiments, which are called 'turbulence in a box simulations'. The name refers to the fact that we are assuming periodic boundary conditions and apply a forcing field, which is created in Fourier space to drive the turbulent motions. We solve the *Euler* equations and analyse the statistical properties on all scales.

Chapter 2 gives an introduction in the basic theoretical background. We start with hydrodynamics on the microscopic level in section 2.1. From the *Boltzmann* equation we derive the macroscopic *Euler* and *Navier-Stokes* equations. Next we give a small introduction into turbulence theory in section 2.2, where we provide the theory in a phenomenological manner. We provide a detailed discussion about statistical tools measuring two-point correlations caused by a turbulent velocity field and show the connection between auto-correlation functions, structure functions, and power spectra. We end this chapter with a brief introduction in *Bayesian* statistics.

We collected in Chapter 3 the description of our numerical setup and the definition of the used methods to avoid repetitions.

In Chapter 4 we start discussing our results. We compare structure functions, their scaling exponents, and the probability density functions of the gas density and velocity increments measured in the Eulerian and Lagrangian

frameworks. Additionally, we compare our findings with common intermittency models. There are two underlying ideas of performing a grid simulation and interpolate the hydrodynamical quantities on so called 'tracer particles' and analyse their properties. The first is to close the gap in the comparison of grid based simulations with smoothed particles simulations, as performed by Price and Federrath (2010). The second motivation was to understand the dynamical properties of sink particles, which are implemented in the same way as the tracer particles. Sink particles are normally used in simulations to prevent runaway collapse at the resolution limit in simulations.

In Chapter 5 we analyse the influence of the compressibility of the flow. We do this by studying the connection of the one-point statistical properties. We investigate the linear relation between the root mean square (r.m.s.) Mach number and the standard deviation of the density distribution. In addition, we decompose the velocity field into its longitudinal and transverse component and find that the density distribution can be described with the parameters of the longitudinal velocity field.

In Chapter 6 we introduce a hierarchical Bayesian fitting method to estimate the parameters describing the scaling relations of the velocity power spectrum. We demonstrate the accuracy and other advantages of this technique compared with ordinary linear regression methods.

The last Chapter 7 summaries our findings and provides an outlook.

Chapter 2

Theory

This chapter provides the relevant theoretical basics necessary for a full understanding of this work. We start in Section 2.1 with deriving the equations of hydrodynamics. Beginning with the *collisionless Boltzmann* equation on the microscopic level we derive the *Euler* and the *Navier-Stokes* equations describing the macroscopic behaviour. In 2.2 we introduce incompressible turbulence theory, first put forward by Kolmogorov's seminal work (Kolmogorov, 1941a,b). We also discuss the partial failure of the Kolmogorov's theory leading to the development of intermittency models.

The chapter ends in Section 2.3 with an introduction in statistical data analysis focusing on Bayesian methods.

2.1   Gas dynamics

One common starting point for an analytic treatment in physics is to derive the *dynamical theory* of a system. In a *dynamical theory*, a series of differential equations, governed by a set of basic parameters, can conclusively describe the time evolution of the physical system. That is, the system-parameters at one instant of time, determines its evolution through the set of differential equations. For continuous media the *Navier-Stokes* equation and the initial conditions comprise a *dynamical theory*. Even though, gases and fluids can be described as continuous media following macroscopic equations, they are ultimately made up of molecules or atoms normally electrically neutral[1]. In the astrophysical context the media have often a few particles

---

[1]Heating a gas to very high temperatures, applying an external radiation field, or by passing an electric discharge through it, one can break up the molecules and atoms in the medium into charged particles. Under certain conditions this medium is called a plasma and can be described with the *Vlasov* instead of the *Boltzmann* equation on

per cm^3, so it is questionable if a continuous description is applicable. There-
fore we choose as a starting point the *Boltzmann* equation, which describes
a N particle system on the microscopic level and derive the *Navier-Stokes*
equation, mentioning and scrutinising the assumptions on each level. We
mainly follow the elegant derivations presented in the textbook Choudhuri
(1998).

2.1.1   The *collisionless Boltzmann equation*

Let us consider a dynamical system of N *similar* particles, which can be
described by the classical Hamilton theory[2], and the generalized position
and momentum coordinates are $(q_i, p_i; i \in 1...3N)$. The Liouville theorem
states for such a system, that the time derivative of the density of ensemble
points in phase space is constant,

$$\frac{\mathrm{d}\rho_e}{\mathrm{d}t} = 0 \,.$$

(2.1)

To prove this statement we write down the total differential for the density
of ensemble points,

$$\mathrm{d}\rho_e(t, \mathbf{q}, \mathbf{p}) = \frac{\partial \rho_e}{\partial t}\mathrm{d}t + \frac{\partial \rho_e}{\partial q_i}\mathrm{d}q_i + \frac{\partial \rho_e}{\partial p_i}\mathrm{d}p_i \,,$$

(2.2)

and a generalized version of the continuity equation in $6N$-dimensional phase-
space

$$\frac{\partial}{\partial t}\int_V \rho_e \,\mathrm{d}^{3N}q \,\mathrm{d}^{3N}p = -\oint_{\delta V} \rho_e \,\mathbf{v} \cdot \mathrm{d}\mathbf{f} = -\int_V \boldsymbol{\nabla}_{q,p} \cdot (\rho_e \,\mathbf{v}) \,\mathrm{d}^{3N}q \,\mathrm{d}^{3N}p,$$

(2.3)

where V is any volume in phase-space, δV is its surface with the out-
wards directed normal $\mathrm{d}\mathbf{f}$, and $\mathbf{v}$ is the velocity of the phase-space point
$\mathrm{d}/\mathrm{d}t \,(q_1...q_{3N}, p_1...p_{3N})$. As this equation is true for any V the integrand
have to fulfil,

$$\frac{\partial}{\partial t}\rho_e + \boldsymbol{\nabla}_{q,p} \cdot (\rho_e \,\mathbf{v}) = 0$$

(2.4)

which is the continuity equation in $6N$-dimensional phase-space. Using (2.2),
(2.4), and Hamilton's equations,

$$\frac{\partial \dot{q}_i}{\partial q_i} = \frac{\partial}{\partial q_i}\frac{\partial H}{\partial p_i} = \frac{\partial}{\partial p_i}\frac{\partial H}{\partial q_i} = -\frac{\partial \dot{p}_i}{\partial p_i} \,,$$

(2.5)

---

the microscopic level and end up in the full Magneto Hydrodynamic equations in the
continuous description.

   [2] The assumption of a classical system implies that the de Broglie wavelength's are not
overlapping, so $n^{1/3} \gg h/\sqrt{m\kappa_B T}$, where m is the mass of a particle, κ_B is the Boltzmann
constant, T the temperature, and h the Planck constant.

the Liouville theorem (2.1) follows directly. Suppose that a number of ensemble points fill up the volume $\mathrm{d}^{3N}q\,\mathrm{d}^{3N}p$ and after some time $\mathrm{d}^{3N}q'\,\mathrm{d}^{3N}p'$. Form conservation of ensemble points it follows that

$$\rho_e \mathrm{d}^{3N}q\,\mathrm{d}^{3N}p = \rho'_e \mathrm{d}^{3N}q'\,\mathrm{d}^{3N}p'\,. \tag{2.6}$$

Since $\mathrm{d}\rho_e/\mathrm{d}t = 0$ we see that

$$\mathrm{d}^{3N}q\,\mathrm{d}^{3N}p = \mathrm{d}^{3N}q'\,\mathrm{d}^{3N}p'\,, \tag{2.7}$$

which we will use later.

Now we map the $6N$-dimensional phase-space $\Gamma(q_i,\,p_i;\,i \in 1...3N)$ to a 6-dimensional phase-space $\mu(\mathbf{x},\,\mathbf{u})$. Every point in the Γ-space describes the whole system of the N particles and corresponds to N points in the μ-space. This has the advantage that we can define a density distribution function in μ-space,

$$f(\mathbf{x},\,\mathbf{u},\,t) = \lim_{V \to 0^+} \frac{\delta N}{\delta V}\,, \tag{2.8}$$

where δV is a small volume (compared to the overall spatial extension of the system) and δN is a sufficient large number of particles inside this volume. We used in (2.5) the Hamilton equations to derive the Liouville theorem. Therefore, we define the Hamilton function in μ-space

$$H(\mathbf{x},\,\mathbf{u},\,t) = \frac{1}{2}\mathbf{u}^2 + \phi(\mathbf{x})\,, \tag{2.9}$$

where we assume that $\phi(\mathbf{x})$ is an external potential.[3] With this definition the Liouville theorem can be derived in the μ-space,

$$\frac{\mathrm{d}f}{\mathrm{d}t} = \frac{\partial f}{\partial t} + \dot{\mathbf{x}} \cdot \boldsymbol{\nabla}f + \dot{\mathbf{u}} \cdot \boldsymbol{\nabla}_{\mathbf{u}}f = 0\,, \tag{2.10}$$

which is the famous *collisionless Boltzmann* equation (Boltzmann, 1872).

2.1.2 The full Boltzmann equation

We discuss now how equation (2.10) has to be modified for a a *dilute* gas[4], taking collisions into account. Therefore, we modify equation (2.10) by adding

---

[3]Here we have in fact two constrains. First, we assume that the system is conservative $\partial\phi(\mathbf{x})/\partial\mathbf{u} = 0$, neglecting dissipation, as we are describing the particle level. Second, we neglect the particle interactions, like collisions, which would result in a potential of the form $\phi(\mathbf{x}, \mathbf{x'})$ for $|\mathbf{x} - \mathbf{x'}| \leqslant a$, where a is the collision radius.

[4]We assume a dilute gas and therefore the volume of the particles can be neglected with respect to the total volume $na^3 \ll 1$, where n is the number density of particles and a is the particle radius. This implies that the ideal gas law will be a result later, multi-particle interaction can be neglected, and the mean free path $\lambda \gg a$. In other words, the particles are moving freely most of the time and collisions are instantaneous events.

a source and a sink term on the right-hand side

$$\frac{\mathrm{d}f}{\mathrm{d}t}\mathrm{d}^3x\mathrm{d}^3u = C_{in} - C_{out}\,, \tag{2.11}$$

where C_{in} and C_{out} are the rates at which particles get scattered in and out the volume $\mathrm{d}^3x\mathrm{d}^3u$ in μ-space due to collisions. To calculate these terms we make the Ansatz with the differential cross section, assuming two beams of particles with initial velocities $\mathbf{u}_1$, $\mathbf{u}_2$ and number densities n_1, n_2 and resulting velocities $\mathbf{u}'_1$, $\mathbf{u}'_2$ and number densities n'_1, n'_2. From momentum and energy conversation in a single collision it follows directly

$$|\mathbf{u}_1 - \mathbf{u}_2| = |\mathbf{u}'_1 - \mathbf{u}'_2|\,, \tag{2.12}$$

$$\mathbf{u}_1^2 + \mathbf{u}_2^2 = \mathbf{u}'^2_1 + \mathbf{u}'^2_2\,. \tag{2.13}$$

The number of collisions per unit volume and unit time δn_c that get deflected into the solid angle $\mathrm{d}\mathbf{\Omega}$ is proportional to the densities, the difference in the velocities and the differential cross section $\sigma(\mathbf{u}_1,\,\mathbf{u}_2|\mathbf{u}'_1,\,\mathbf{u}'_2)$ (see e.g. Choudhuri, 1998, Section 2.1 and 2.2),

$$\delta n_c = \sigma(\mathbf{u}_1,\,\mathbf{u}_2|\mathbf{u}'_1,\,\mathbf{u}'_2)\,n_1 n_2\,|\mathbf{u}_1 - \mathbf{u}_2|\,\mathrm{d}\mathbf{\Omega}\,. \tag{2.14}$$

Replacing the number densities $n = f(\mathbf{x},\,\mathbf{u},\,t)\mathrm{d}^3u$ and integrating over all possible velocities of the second beam d^3u_2 and solid angles $\mathrm{d}\mathbf{\Omega}$, results for the rate of particles that get scattered out of the phase-space volume $\mathrm{d}^3x\,\mathrm{d}^3u_1$ in

$$C_{out} = \mathrm{d}^3x\,\mathrm{d}^3u_1\iint \mathrm{d}^3u_2\,\mathrm{d}\mathbf{\Omega}\,\sigma(\mathbf{u}_1,\,\mathbf{u}_2|\mathbf{u}'_1,\,\mathbf{u}'_2)\,|\mathbf{u}_1{-}\mathbf{u}_2|\,f(\mathbf{x},\,\mathbf{u}_1,\,t)\,f(\mathbf{x},\,\mathbf{u}_2,\,t)\,. \tag{2.15}$$

For calculating C_{in} we assume that collisions on the particle level are reversible, what results in a symmetric differential cross section

$$\sigma(\mathbf{u}_1,\,\mathbf{u}_2|\mathbf{u}'_1,\,\mathbf{u}'_2) = \sigma(\mathbf{u}'_1,\,\mathbf{u}'_2|\mathbf{u}_1,\,\mathbf{u}_2)\,. \tag{2.16}$$

With the same Ansatz (2.14), but now considering the reverse collisions with initially $\mathrm{d}^3u'_1$ and $\mathrm{d}^3u'_2$ and resulting d^3u_1 and d^3u_2, we get for the number of particles per unit time C_{in} that get scattered in the volume $\mathrm{d}^3x\,\mathrm{d}^3u_1$

$$C_{in} = \mathrm{d}^3x\,\mathrm{d}^3u_1\iint \mathrm{d}^3u_2\,\mathrm{d}\mathbf{\Omega}\,\sigma(\mathbf{u}_1,\,\mathbf{u}_2|\mathbf{u}'_1,\,\mathbf{u}'_2)\,|\mathbf{u}_1 - \mathbf{u}_2|\,f(\mathbf{x},\,\mathbf{u}'_1,\,t)\,f(\mathbf{x},\,\mathbf{u}'_2,\,t)\,, \tag{2.17}$$

where we used (2.7, with $\mathrm{d}^3x = \mathrm{d}^3x'$), (2.12) and (2.16). Putting (2.15) and (2.17) in (2.11), renaming the indices, and assuming that the differential

cross section is spherically symmetric, we finally have the same result as Boltzmann (1872),

$$\frac{\partial f}{\partial t} + \dot{\mathbf{x}} \cdot \boldsymbol{\nabla} f + \dot{\mathbf{u}} \cdot \boldsymbol{\nabla_u} f = \int \mathrm{d}^3 \widetilde{u} \int \mathrm{d}\boldsymbol{\Omega} \, |\mathbf{u} - \widetilde{\mathbf{u}}| \, \sigma(\boldsymbol{\Omega})(f' \widetilde{f}' - f \widetilde{f}) \,, \quad (2.18)$$

where we substituted $\widetilde{f}' = f(\mathbf{x}, \widetilde{\mathbf{u}}', t)$.

2.1.3 The Maxwellian distribution

A uniform classical gas left to itself relaxes to a Maxwellian distribution Maxwell (1860). This distribution can be derived with the equilibrium solution of the full Boltzmann equation with the collision integral (2.18) (see Section 2.3 in Choudhuri, 1998)

$$f(\mathbf{x}, \mathbf{u}, t) = n(\mathbf{x}, t) \left(\frac{m}{2\pi \kappa_B T(\mathbf{x}, t)} \right)^{3/2} \exp \left[-\frac{m(\mathbf{u}(\mathbf{x}, t) - \mathbf{v})^2}{2\kappa_B T(\mathbf{x}, t)} \right] \quad (2.19)$$

where $f(\mathbf{x}, \mathbf{u}, t)$ is the particle distribution function in 6 dimensional phase space, $n(\mathbf{x}, t)$ is the particle number density, m is the mass of a particle, κ_B is the Boltzmann constant, $T(\mathbf{x}, t)$ is the averaged temperature, $\mathbf{u}(\mathbf{x}, t)$ is the velocity of the particles, and $\mathbf{v}$ is the mean local velocity. Although we assumed for deriving the Maxwell distribution static equilibrium $\partial f / \partial t = 0$ and a uniform medium $\partial f / \partial x = 0$ we keep these dependencies in the general equation (2.19) such that we can refer later to this equation.

2.1.4 The conservation equation

Let's consider a quantity which is conserved in a binary collision $\chi(\mathbf{x}, \mathbf{u}) + \chi(\mathbf{x}, \widetilde{\mathbf{u}}) = \chi(\mathbf{x}, \mathbf{u}') + \chi(\mathbf{x}, \widetilde{\mathbf{u}}')$. By multiplying equation (2.18) with χ and integrate over $\mathrm{d}^3 u$ we get

$$\int \mathrm{d}^3 u \, \chi \frac{\mathrm{d}f}{\mathrm{d}t} = \int \mathrm{d}^3 u \int \mathrm{d}^3 \widetilde{u} \int \mathrm{d}\boldsymbol{\Omega} \, |\mathbf{u} - \widetilde{\mathbf{u}}| \, \sigma(\boldsymbol{\Omega})(f' \widetilde{f}' - f \widetilde{f}) \chi \,. \quad (2.20)$$

The right-hand side of equation (2.20) vanishes (see e.g. Choudhuri, 1998, Section 2.5), so that we can write using (2.10)

$$\frac{\partial}{\partial t} \int \mathrm{d}^3 u \, \chi f + \frac{\partial}{\partial x_i} \int \mathrm{d}^3 u \, \chi u_i f - \int \mathrm{d}^3 u \, u_i f \frac{\partial \chi}{\partial x_i} - \int \mathrm{d}^3 u \, \dot{u}_i f \frac{\partial \chi}{\partial u_i} \int \mathrm{d}^3 u \, f \chi \frac{\partial \dot{u}_i}{\partial u_i} = 0 \,, \quad (2.21)$$

where we used that $\mathrm{d}/\mathrm{d}t\,\chi = 0$ and that the integral $\int \mathrm{d}^3u\,\partial/\partial u_i(\chi \dot{u}_i f)$ can be transformed into a surface integral, which vanishes at infinity assuming $f \to 0$ for $x \to \infty$. By introducing the average of a quantity Q,

$$\langle Q \rangle = \frac{1}{n} \int \mathrm{d}^3u\, Q f\,, \tag{2.22}$$

where $n = \int \mathrm{d}^3u\, f$ is the number density per unit volume, it follows from (2.21) that

$$\frac{\partial}{\partial t}\left(n\,\langle\chi\rangle\right) + \frac{\partial}{\partial x_i}\left(n\,\langle u_i\chi\rangle\right) - n\left\langle u_i\frac{\partial\chi}{\partial x_i}\right\rangle - \frac{n}{m}\left\langle F_i\frac{\partial\chi}{\partial u_i}\right\rangle - \frac{n}{m}\left\langle \chi\frac{\partial F_i}{\partial u_i}\right\rangle = 0\,, \tag{2.23}$$

where we introduced an external force on a particle $F_i = m\dot{u}_i$. This is the so called *conservation equation*, which is of central importance, as it describes how the volume density $n\,\langle\chi\rangle$ of any quantity χ conserved in a binary collision evolves in time. It also provides the important step going from the microscopic particle level towards the macroscopic continuum description.

2.1.5 The moment equations

Deriving the equations describing the time evolution of the mass, momentum, and energy using equation (2.23) one assumes that these quantities are conserved in a binary collision[5]. Further, the force is assumed to be independent of the velocity. Putting $\chi = m$ in (2.23) results in

$$\frac{\partial\rho}{\partial t} + \frac{\partial}{\partial x_i}(\rho v_i) = 0\,, \tag{2.24}$$

where $nm = \rho$ is the local mass-density and $\langle u_i \rangle = v_i$ is the averaged flow velocity. Substituting $\chi = mu_j$ in (2.23) gives

$$\frac{\partial}{\partial t}(\rho v_j) + \frac{\partial}{\partial x_i}(\rho\,\langle u_i u_j\rangle) - nF_j = 0\,, \tag{2.25}$$

which can be further simplified with the definition of the tensor

$$P_{ij} = nm\,\langle (u_i - v_j)(u_j - v_i)\rangle = nm(\langle u_i u_j\rangle - v_i v_j)\,, \tag{2.26}$$

$$\frac{\partial}{\partial t}(\rho v_j) + \frac{\partial}{\partial x_i}(\rho v_i v_j) = -\frac{\partial P_{ij}}{\partial x_i} + \frac{\rho}{m}F_j\,. \tag{2.27}$$

---

[5]The translational kinetic energy is only conserved in binary collisions for monatomic gas particles. For more complex molecules the energy can be transformed in e.g. rotational energy.

Finally, substituting the kinetic energy $\chi = 1/2m\,|\mathbf{u} - \mathbf{v}|^2$ in equation (2.23) gives

$$\frac{\partial}{\partial t}(\rho\epsilon) + \frac{\partial}{\partial x_i}(\rho\epsilon v_i) + \frac{\partial q_i}{\partial x_i} + P_{ij}\Lambda_{ij} = 0\,, \tag{2.28}$$

where

$$\epsilon = \frac{1}{2}\left\langle |\mathbf{u} - \mathbf{v}|^2 \right\rangle \tag{2.29}$$

is the internal energy per unit mass,

$$\mathbf{q} = \frac{1}{2}\rho\left\langle (\mathbf{u} - \mathbf{v})\,|\mathbf{u} - \mathbf{v}|^2 \right\rangle \tag{2.30}$$

is the energy flux, and

$$\Lambda_{ij} = \frac{1}{2}\left(\frac{\partial v_i}{\partial x_j} + \frac{\partial v_j}{\partial x_i} \right)\,. \tag{2.31}$$

We stress here that equations (2.24), (2.27), and (2.28) do *not* constitute a dynamical theory as they are five independent equations for fourteen variables.

2.1.6 The Euler equations

Section 2.1.3 showed that collisions between particles play an important role in establishing a fluid like behaviour, as they tend to set up a Maxwellian velocity distribution. To demonstrate how the Maxwell distribution on the microscopic level and a fluid-like behaviour on the macroscopic level are connected, we assume a medium that fulfils the Maxwell distribution (2.19) on each point. Using equations (2.19) and (2.22) in (2.26), (2.29), and (2.30) gives

$$P_{ij} = p\delta_{ij}\,, \text{with } p = n\kappa_B T\,, \tag{2.32}$$

$$\epsilon = \frac{3}{2}\frac{\kappa_B T}{m}\,, \tag{2.33}$$

$$\mathbf{q} = 0\,, \tag{2.34}$$

where p is the pressure, (2.32) is the equation of state of an ideal gas, and (2.33) is the internal energy of a monatomic gas. Using these results and substituting (2.19) and (2.22) in (2.24), (2.27), and (2.28) gives

$$\frac{\partial \rho}{\partial t} + \boldsymbol{\nabla} \cdot (\rho\mathbf{v}) = 0\,, \tag{2.35}$$

$$\frac{\partial \mathbf{v}}{\partial t} + (\mathbf{v} \cdot \boldsymbol{\nabla})\,\mathbf{v} = -\frac{\nabla p}{\rho} + \mathbf{f}\,, \tag{2.36}$$

$$\rho \left(\frac{\partial \epsilon}{\partial t} + \mathbf{v} \cdot \boldsymbol{\nabla} \epsilon \right) + p \boldsymbol{\nabla} \cdot \mathbf{v} = 0 \,, \tag{2.37}$$

which are the well-known *Euler* equations. Additionally, we assign $\mathbf{f} = \mathbf{F}/m$ as the force per unit mass, instead of the force on a single particle, as we end up with the continuum description of the medium[6]. As we can express the pressure p and the internal energy ϵ with the temperature T and the density ρ (equations 2.32, 2.33) we have five independent variables (ρ, T, $\mathbf{v}$) and five independent scalar equations, which can be considered as a dynamical theory of macroscopic nature. However, some characteristics of real fluids are still lacking, e.g. transport of energy or momentum inside the systems, which is caused by assuming Maxwell distributed velocities at each point.

2.1.7   Transport phenomena

Assuming two locations in a medium separated by the distance L with different temperatures, we expect two different velocity distributions at these locations (2.19). In a position in between, the particles streaming in from the hotter region are faster than these from the colder region, so that the region in between deviates from the initial distribution depending on the temperature difference. Therefore, we make the Ansatz

$$f(\mathbf{x}, \mathbf{u}, t) = f^0(\mathbf{x}, \mathbf{u}, t) + g(\mathbf{x}, \mathbf{u}, t) \tag{2.38}$$

where $f^0(\mathbf{x}, \mathbf{u}, t)$ is the Maxwell distribution and $g(\mathbf{x}, \mathbf{u}, t)$ is a small departure from it. We will not perform here the derivation by putting (2.38) in the full Boltzmann equation (2.18). We refer the reader interested in this complex and complicated topic to Chapman (1916); Enskog (1917) or the textbook Chapman and Cowling (1970). An order-of-magnitude estimate,

---

[6]We introduce here the common nomenclature by defining the force per unit mass f. However, we want to mention that this can be misleading. The $\mathbf{F}/m = \dot{\mathbf{u}}$ term comes from the time derivative of the velocity of a particle, so introducing a force, which is the time derivative of the momentum, is not problematic as the particle cannot change mass. So, the minor mistake of speaking about force instead of force per unit mass, has no effect. But, in the continuum description, where we have a varying density field one has to be more careful. In the derivation of the *Navier-Stokes* equation on the macroscopic level the common Ansatz is to calculate the force on a volume element

$$\delta \mathbf{F} = \delta \mathbf{F}_{surface} + \delta \mathbf{F}_{body} \,.$$

The right-hand side of this equation gives $\int_{\delta V} P_{ij} \mathrm{d} S_j + \mathbf{F}_{body}$, which is the same as the RHS of (2.36) divided by the density, but the LHS gives $\mathrm{d}/\mathrm{d}t(\rho \mathbf{v}) = \mathbf{v}\mathrm{d}/\mathrm{d}t\rho + \rho \mathrm{d}/\mathrm{d}t\mathbf{v}$. Therefore, the minor mistake of dropping the "*per unit mass*" has an impact there.

called BGK equation after Bhatnagar et al. (1954), gives

$$\frac{\mathrm{d}f}{\mathrm{d}t} = \frac{f^0 - f}{\tau}\,, \tag{2.39}$$

where the approximated function f relaxes to the Maxwell distribution f^0 in the collision time τ. The *Chapman-Enskog expansion* approximates the distribution function with

$$f = \sum_{i=0}^{\infty} \left(\frac{\lambda}{L}\right)^i f^i\,, \tag{2.40}$$

where λ is the mean free path and L is a typical length scale. The goal of these approximations is to express g as a function of the already known parameters such that we can put it in (2.26) – (2.30), as we did in the last section with the Maxwell distribution. The zero order approximation for example gives $f = f^0$ and using

$$\frac{\partial f^0}{\partial t} = \frac{\partial f^0}{\partial n}\frac{\partial n}{\partial t} + \frac{\partial f^0}{\partial T}\frac{\partial T}{\partial t} + \frac{\partial f^0}{\partial v_i}\frac{\partial v_i}{\partial t} \tag{2.41}$$

and similar expressions for $\partial f^0/\partial x_i$ and $\partial f^0/\partial u_i$, (2.39) leads to

$$\left(\frac{\partial}{\partial t} + u_i\frac{\partial}{\partial x_i} + \frac{F_i}{m}\frac{\partial}{\partial u_i}\right) f^0 = \frac{g}{\tau}\,. \tag{2.42}$$

After few steps of algebra we end up with

$$P_{ij} = p\delta_{ij} - 2\mu\left(\Lambda_{ij} - \frac{1}{3}\delta_{ij}\boldsymbol{\nabla}\cdot\mathbf{v}\right)\,, \tag{2.43}$$

$$\mathbf{q} = -K\boldsymbol{\nabla}T\,, \tag{2.44}$$

where μ is the the kinematic viscosity and K is the thermal conductivity. With the zero order approximation these parameters are

$$K = \frac{5}{2}\tau n\frac{\kappa_B^2 n}{m} \quad \mu = \tau n\kappa_B T\,, \tag{2.45}$$

which is derived in Choudhuri (1998, Section 3.4, 3.5). The pre-factors of these expressions change, depending on the approximation. But it is noteworthy that with the crude zero order approximation of f one gets results only changing by a factor of few (≈ 3) for these material parameters in comparison with much more complicated derivations with higher orders. Using

these results and assuming that $\partial\mu/\partial x_i = 0$, one gets from the moment equations (2.27) and (2.28)

$$\frac{\partial \mathbf{v}}{\partial t} + (\mathbf{v} \cdot \boldsymbol{\nabla}) \, \mathbf{v} = -\frac{\nabla p}{\rho} + \frac{\mu}{\rho} \left(\boldsymbol{\nabla}^2 \mathbf{v} + \frac{1}{3} \boldsymbol{\nabla}(\boldsymbol{\nabla} \cdot \mathbf{v})^2 \right) + \mathbf{f}, \qquad (2.46)$$

$$\rho \left(\frac{\partial \epsilon}{\partial t} + \mathbf{v} \cdot \boldsymbol{\nabla}\epsilon \right) + \boldsymbol{\nabla} \left(K \boldsymbol{\nabla} T \right) + p\boldsymbol{\nabla} \cdot \mathbf{v} - 2\mu \left(\Lambda_{ij}\Lambda_{ij} - \frac{1}{3} \boldsymbol{\nabla}(\boldsymbol{\nabla} \cdot \mathbf{v})^2 \right) = 0 \,.$$
$$(2.47)$$

These equations can be simplified further by assuming that the $\boldsymbol{\nabla} \cdot \mathbf{v}$ term in (2.46) is usually small and can be neglected. The μ term in (2.47) corresponds to the transformation of kinetic energy into internal energy due to viscosity and can also be neglected in most circumstances. With these assumptions we can write down the full set of hydrodynamic equations for the dynamical theory:

$$\frac{\partial \rho}{\partial t} + \boldsymbol{\nabla} \cdot (\rho\mathbf{v}) = 0 \,, \qquad (2.48)$$

$$\frac{\partial \mathbf{v}}{\partial t} + (\mathbf{v} \cdot \boldsymbol{\nabla}) \, \mathbf{v} = -\frac{\nabla p}{\rho} + \frac{\mu}{\rho} \boldsymbol{\nabla}^2 \mathbf{v} + \mathbf{f} \,, \qquad (2.49)$$

$$\rho \left(\frac{\partial \epsilon}{\partial t} + \mathbf{v} \cdot \boldsymbol{\nabla}\epsilon \right) + \boldsymbol{\nabla} \left(K \boldsymbol{\nabla} T \right) + p\boldsymbol{\nabla} \cdot \mathbf{v} = 0 \,, \qquad (2.50)$$

which are called *Navier-Stokes* equations.

2.2   Turbulence theory

"Big whorls have little whorls, which feed on their velocity, and little whorls have lesser whorls, and so on to viscosity."

Reformulation in the turbulence context by Lewis Richardson, original poem of

De Morgan (1872)

Unlike in other fields of physics where the structural requirements of a dynamical theory yield completely predictable systems, gases and fluids can develop random and chaotic *turbulent* motions, which are completely unpredictable. This is kind of the same problem we had in the last section. All positions and velocities of N particles in a fluid element follow the deterministic description in the Hamilton theory, but it is intuitively clear that this

N-body system is unpredictable after some time. "Chaos theory suggests that even in a deterministic system, if the equations describing its behaviour are non-linear a tiny change of the initial conditions can lead to a cataclysmic and unpredictable result." (Lorre et al., 2013). The reason for this behaviour is that small perturbations on the initial state end up in totally different regions in phase space, such that the trajectories describing the time evolution of the whole system drift apart even if they start very close to each other. However, by transforming the problem in six dimensional phase-space with the Boltzmann distribution function we are able to simplify the problem ending up with the hydrodynamic equations with only few parameters determining the behaviour of a fluid element, consisting of many atoms or molecules. In the derivation we found that the Maxwell distribution function is a statistical treatment of all the particles velocities, so that we can ignore the individual particles velocities and can describe their average influence on the fluid element. In a turbulent medium the situation is the same. For example, the chaotic motions of smoke coming out of a chimney indicate random velocities ranging from the size of the chimney down to the length scales our eye or camera can resolve. But, we can simplify the equations describing e.g. the chemical mixing of the smoke in the air by describing the velocity field with a statistical theory. Even though an overall theory of turbulence remains elusive, the milestone work of Kolmogorov (1941a,b) provides predictions for the averaged behaviour of the velocity field in a turbulent medium in a statistical sense. Unfortunately, this theory is limited to incompressible media, where the density is assumed to be constant. In the astrophysical context, e.g. for understanding the supersonic motions in giant molecular clouds, the motions have to be described with a compressible turbulence theory, where analytic results are even rarer. In addition, compressible turbulence can not be studied efficiently in laboratory experiments such that astrophysical observations and numerical simulations are the only data sources for studying compressible turbulence.

Before we go on with the turbulence theory, we want to mention that we can decompose a velocity field in a mean flow $\overline{\mathbf{v}}$ and a turbulent part $\mathbf{v}$'. We focus in the following discussion on the turbulent part, which fulfils $\overline{\mathbf{v'}} = 0$, and write for it $\mathbf{v}$ without the prime.

2.2.1 Phenomenology of turbulence

The *similarity principle* states that the *Reynolds number*

$$Re = \frac{LV}{\nu}\,, \tag{2.51}$$
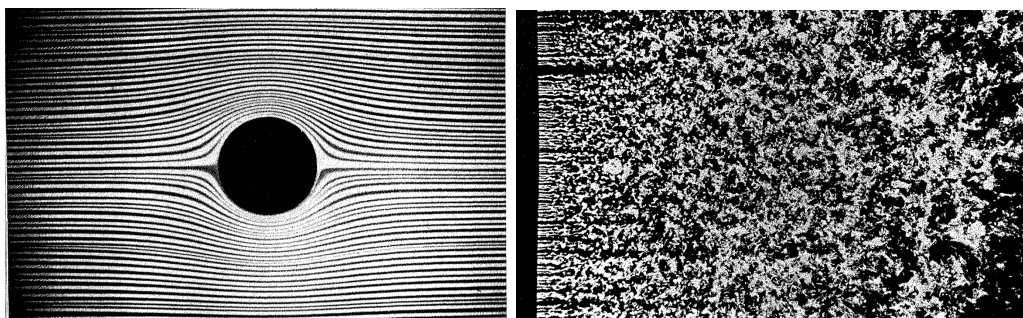
Figure 2.1: Photographs from van Dyke (1982) illustrating the transition from a laminar flow to a chaotic, turbulent one by increasing the Reynolds number. Left: Uniform flow around a cylinder with a Reynolds number $Re \ll 100$. *Photograph by D. H. Peregrin.* Right: Homogeneous, isotropic turbulence behind a grid at large Reynolds number, $Re \gg 100$. *Photograph by T. Corke and Hassan Naghi.*

where L, V, and ν being a characteristic length, velocity and kinematic viscosity, is the only control parameter of a flow for a given geometrical shape of boundary conditions. In Figure 2.1 we show photographs presented in van Dyke (1982) to illustrate the influence of the Reynolds number. The left figure shows a *laminar* flow around a cylinder at low Reynolds number, whereas the right picture provides a turbulent flow at high Reynolds numbers behind a grid. At which Reynolds number this transition happens depends strongly on the properties of the experiment, such as the geometry.

We will use these examples to discuss the symmetries of the *Navier Stokes* equations. We follow mainly the discussion in Frisch (1995) and focus therefore on the invariant group[7] describing incompressible turbulence.

Definition (Symmetry group)
Let $\mathcal{H}$ be the set of all functions solving the *Navier Stokes* equation (2.49) and **G** be a group of transformations acting on $\mathcal{H}$. **G** is called a *symmetry group*, if for all velocity fields solving the *Navier Stokes* equations $\mathbf{v}(\mathbf{x}, t) \in \mathcal{H}$ and all transformations $g \in \mathbf{G}$ the resulting function $g\left(\mathbf{v}(\mathbf{x}, t)\right) \in \mathcal{H}$, so $g : \mathcal{H} \to \mathcal{H}$.

---

[7] Recall that a group is a set G with an operation $(\cdot)$ which has to fulfil the properties: (closure) $\forall a, b \in G, a \cdot b \in G$, (associativity) $\forall a, b, c \in G, a \cdot (b \cdot c) = (a \cdot b) \cdot c$, (identity element) $\exists! e : a \cdot e = e \cdot a = a$.

space translations: $g_{\boldsymbol{\lambda}}$	$t, \mathbf{r}, \mathbf{v}$	$\mapsto$	$t, \mathbf{r} + \boldsymbol{\lambda}, \mathbf{v}$	$\boldsymbol{\lambda} \in \mathbb{R}^3$
time translations: g_{τ}	$t, \mathbf{r}, \mathbf{v}$	$\mapsto$	$t + \tau, \mathbf{r}, \mathbf{v}$	$\tau \in \mathbb{R}$
Galilean transformations: $g_{\mathbf{U}}$	$t, \mathbf{r}, \mathbf{v}$	$\mapsto$	$t, \mathbf{r} + \mathbf{U}t, \mathbf{v} + \mathbf{U}$	$\mathbf{U} \in \mathbb{R}^3$
parity: g_P	$t, \mathbf{r}, \mathbf{v}$	$\mapsto$	$t, -\mathbf{r}, -\mathbf{v}$	
rotation: g_R	$t, \mathbf{r}, \mathbf{v}$	$\mapsto$	$t, \mathrm{R}\mathbf{r}, \mathrm{R}\mathbf{v}$	$\mathrm{R} \in \mathrm{SO}(\mathbb{R}^3)$
scaling(for $\nu = 0$) : g_{γ}	$t, \mathbf{r}, \mathbf{v}$	$\mapsto$	$\gamma^{1-h}t, \gamma\mathbf{r}, \gamma^h\mathbf{v}$	$\gamma \in \mathbb{R}_+$
				$h \in \mathbb{R}$

Table 2.1: List of symmetry groups of the *Navier Stokes* equation.

Table 2.1 provides a list of the known symmetries of the *Navier Stokes* equation (2.49). The scaling transformation plays a special role in turbulence theory and applying it to equation (2.49) shows that all terms get multiplied by γ^{2h-1}, except the viscous term which is multiplied by γ^{h-2}. Therefore the scaling group does in viscous fluids only contain the transformation with $h = -1$, which is the above mentioned *similarity principle*, as this transformation keeps the Reynolds number constant. It is intuitively clear from Figure 2.1 that the laminar flow (left) follows some symmetries that are not present in the turbulent case (right). But these symmetries can be restored by averaging over small volume elements in the turbulent wake, leading Kolmogorov (1941b) to his hypotheses[8]:

Hypothesis (H1)
"In the limit of infinite Reynolds numbers, all the possible symmetries of the Navier Stokes equation, usually broken by the mechanism producing the turbulent flow, are restored in a statistical sense at small scales and away from boundaries." (Frisch, 1995)

Hypothesis (H2)
"Under the same assumptions as H1, the turbulent flow is self-similar at small scales, i.e. it possesses a unique scaling exponent h." (Frisch, 1995)

Hypothesis (H3)
"Under the same assumptions as H1, the turbulent flow has a finite non vanishing mean rate of dissipation ϵ per unit mass." (Frisch, 1995)

---

[8] We use the rather freely reformulations following the description of Frisch (1995) emphasising the modern interpretation in the context of symmetry group theory, dynamical systems, and stochastic differential equations.

When all symmetries are restored in statistical sense, the turbulent flow is called *fully developed*. With this idea of treating turbulence Kolmogorov (1941b) derived an *exact* relation describing the scaling behaviour of the third order longitudinal structure function, known as the *four-fifths law*:

"*In the limit of infinite Reynolds number, the third order longitudinal structure function of homogeneous, isotropic turbulence, evaluated for increments ℓ small compared to the integral scale, is given in terms of the mean energy dissipation rate per unit mass ϵ (assumed to be finite and non vanishing) by*

$$\left\langle (\delta v_\parallel (\mathbf{r}, \boldsymbol{\ell})^3 \right\rangle = -\frac{4}{5}\epsilon \ell ."$$ (2.52)

(Kolmogorov, 1941b)

(We will discuss structure functions, their definition, interpretation, and connection to other two-point measurements in detail in the next section 2.2.2 and focus here more on the main results of the Kolmogorov theory.)

To understand this result we have to look at the energy budget of the flow. Subtraction of the continuity equation (2.48) multiplied by $1/2v_i v_i$ and equation (2.43) in (2.27) by v_i gives for the kinetic energy (equation 4.1 in Kida and Orszag, 1990)

$$\frac{\partial}{\partial t}E_{kin} = -\frac{\partial}{\partial x_i}(v_i E_{kin}) - v_i \frac{\partial p}{\partial x_i} + 2\mu v_i \frac{\partial}{\partial x_i}\left(\Lambda_{ij} - \frac{1}{3}(\boldsymbol{\nabla}\cdot\mathbf{v})^2\right) + \rho v_i f_i$$
$$= (AD) + (PD) + (VD) + (F),$$ (2.53)

where the four terms on the RHS are called advection (AD), pressure dilatation (PD), viscous-dissipation (VD), and forcing (F) terms, respectively. By assuming incompressibility the PD term vanishes and by performing a spatial and time average we get

$$\left\langle \frac{\partial}{\partial t}E_{kin} \right\rangle = \langle AD \rangle + \langle VD \rangle + \langle F \rangle ,$$ (2.54)

where the AD term vanishes by using the "Gauss's theorem" to transform the volume integral in a surface integral and assuming that the velocity field vanishes at infinity. In the state of fully developed turbulence the LHS is zero such that the viscous transfer of energy from kinetic towards internal has to balance the energy input rate of the external forcing. Kolmogorov (1941a) confined now the forcing mechanism on much larger scales and the influence of viscosity on much smaller scales as he wanted to describe in his theory. Therefore, the AD term causes an energy transfer trough the scales

but is not influencing the global averaged energy budget. It can be shown by multiplying the *Navier Stokes* equation with $v_i(\mathbf{r} + \boldsymbol{\ell})$ that the energy transfer trough the scales $\epsilon(\ell)$ is (see e.g. Section 6.2 Frisch, 1995)

$$
\begin{aligned}
\epsilon(\ell) &= -\frac{1}{4}\boldsymbol{\nabla}_\ell \cdot \left\langle |\delta\mathbf{v}(\boldsymbol{\ell})|^2\, \delta\mathbf{v}(\boldsymbol{\ell})\right\rangle \\
&= -\frac{\partial}{\partial t}\frac{1}{2}\left\langle \mathbf{v}(\mathbf{r})\cdot\mathbf{v}(\mathbf{r}+\boldsymbol{\ell})\right\rangle + \left\langle \mathbf{v}(\mathbf{r})\cdot\frac{1}{2}(\mathbf{f}(\mathbf{r}+\boldsymbol{\ell})+\mathbf{f}(\mathbf{r}-\boldsymbol{\ell}))\right\rangle \\
&\quad + \nu\boldsymbol{\nabla}_\ell^2\left\langle \mathbf{v}(\mathbf{r})\cdot\mathbf{v}(\mathbf{r}+\boldsymbol{\ell})\right\rangle ,
\end{aligned}
\tag{2.55}
$$

assuming $\rho = const$ and where $\boldsymbol{\nabla}_\ell$ denotes partial derivatives with respect to the increment $\boldsymbol{\ell}$. Comparing (2.54) with the second line of (2.55) shows that the advection term is causing this energy transfer. These equations lead to the picture of the Richardson cascade (Richardson, 1920), we mentioned in the introduction (see Figure 1.1). In this picture the energy gets injected on the largest scales, creates a constant energy flux through the scales (hypothesis H3), and is taken out of the system by viscosity on the smallest scales.

To derive phenomenologically some scaling relations, we indicate for the rest of this Section with $\sim$ an equality within an order unity constant. Lets denote with ℓ the scale under consideration and v_ℓ the typical velocity associated with this scale. For the integral scale L_0, where the energy gets injected, with the corresponding velocity V_0, the integral time scale is

$$
T_0 = \frac{L_0}{V_0} .
\tag{2.56}
$$

To get a rough limit of the scale of the smallest possible eddies, we assume a Reynolds number of order unity, i.e.

$$
\ell_D v_D \sim \nu .
\tag{2.57}
$$

The energy transfer rate can be estimated by

$$
\epsilon \sim \frac{v_\ell^2}{\tau_\ell} \sim \frac{v_\ell^3}{\ell} ,
\tag{2.58}
$$

so that for the scaling invariance group $h = 1/3$ can be directly inferred. Using (2.57) and (2.58) for the smallest scales results in

$$
l_D \sim \left(\frac{\nu^3}{\epsilon}\right)^{1/4} , \quad v_D \sim (\nu\epsilon)^{1/4}
\tag{2.59}
$$
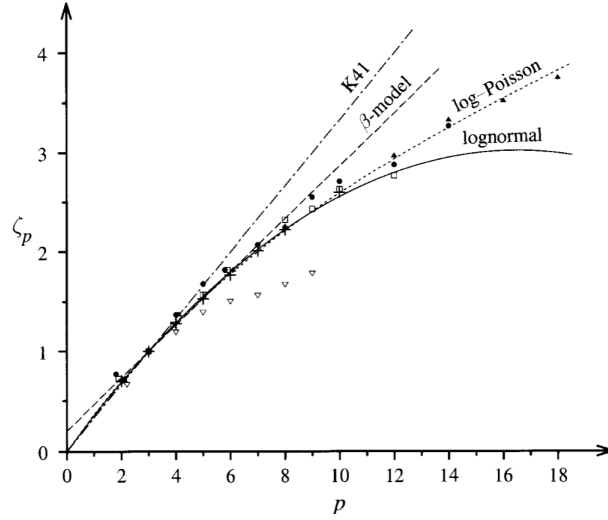
Figure 2.2: Scaling exponent ζ_p of structure functions as a function of the order p. Data of van Atta and Park (1972) have open triangles and Anselmet et al. (1984) filled circles, open squares and filled triangles. The lines correspond to different intermittency models as indicated in the figure. *Figure from* Anselmet et al. (1984).

By using the same trick for the integral scale we get

$$\frac{L}{l_D} \sim Re^{3/4} , \quad \frac{V}{v_D} \sim Re^{1/4} , \tag{2.60}$$

indicating that the separation between the integral scale and the viscous scale increases with the Reynolds number with the power of 3/4.

We close this Section with a discussion about the intermittency problem. With the four fifths law and his second hypotheses (H2) one can conclude that $h = 1/3$. By using the scale invariance transformation one can derive the scaling law for the p's order structure function $\langle (\delta v(\ell)^p \rangle \propto \ell^{p/3}$. Measurements of the scaling behaviour of higher order structure functions revealed partial failure of Kolmogorov's theory (Gurvitch, 1960). But Kolmogorov (1962) and later his collaborator Obukhov (1962) became the first pioneers in the investigation of the 'intermittency' problem with random cascade models, softening the assumption of the constant energy flux. Many intermittency models were derived afterwards to explain the measurements of the scaling exponents, which had a rapid increase in precision (van Atta and Park, 1972; Anselmet et al., 1984; Maurer et al., 1994) (see Figure 2.2). Fractal and log normal models (see Section 8 in Frisch, 1995) showed devi-

ations to the experimental results, whereas log-poisson models of Dubrulle (1994); She and Leveque (1994) do agree. Most recently, the log-poisson processes were used in a mathematical, statistical description for velocity increments (Birnir, 2013) and verified with numerical simulations of incompressible turbulence (Wilczek, 2010; Wilczek et al., 2011) and experiments (Sreenivasan and Dhruva, 1998; Chen et al., 2005; Xu et al., 2006).

2.2.2 Two-point statistics

We will provide in this Section the definition of the covariance, correlation, autocorrelation, structure functions, velocity increments, and power spectra, as these are the main tools for analysing a turbulent medium.

Definition (Correlation, covariance, as used in statistics)
The correlation coefficient $c_{x,y}$ of two random variables x, y with expectation values μ_x, μ_y and standard deviations σ_x, σ_y, is defined as

$$c_{x,y} = corr(x,\, y) = \frac{cov(x,\, y)}{\sigma_x\, \sigma_y} = \frac{E\left((x - \mu_x)(y - \mu_y)\right)}{\sigma_x\, \sigma_y}\,, \qquad (2.61)$$

where $cov(x,\, y)$ is the covariance function and $E()$ is the expected value.

Definition (Auto-Correlation, as used in turbulence theory)
The autocorrelation tensor of the turbulent velocity field is defined as

$$R_{ij}(\ell) = \langle v_i(\mathbf{r}) v_j(\mathbf{r} + \boldsymbol{\ell}) \rangle\,, \qquad (2.62)$$

where the brackets indicate the average over all positions $\mathbf{r}$. It follows from homogeneity that the autocorrelation tensor is independent of $\mathbf{r}$ and from isotropy that it can only depend of the magnitude of $\boldsymbol{\ell}$ and not its direction.

We can directly conclude from this definition that for $\boldsymbol{\ell} = 0$ the diagonal elements of the autocorrelation tensor are $\langle v_i^2 \rangle$, which is the squared standard deviation of the turbulent velocity field and a measure of its total turbulent kinetic energy

$$E_{turb} = \frac{1}{2}\left\langle v^2 \right\rangle = \frac{3}{2}\left\langle v_i^2 \right\rangle\,. \qquad (2.63)$$

On the other hand, assuming that $\boldsymbol{\ell} \to \infty$ the velocities are uncorrelated resulting in

$$\lim_{r \to \infty} \langle v_i(\mathbf{r}) v_j(\mathbf{r} + \boldsymbol{\ell}) \rangle = \langle v_i(\mathbf{r}) \rangle \langle v_j(\mathbf{r} + \boldsymbol{\ell}) \rangle = 0\,. \qquad (2.64)$$

Therefore, the autocorrelation is only non-zero in a limited range. Thus with the autocorrelation tensor the strength and the *correlation length* of turbulence can be measured.

Karman and Howarth (1938) showed that assuming homogeneity, isotropy, and preserving parity, the autocorrelation tensor can be written in the form

$$R_{ij}(\ell) = A(\ell)r_i r_j + B(\ell)\delta_{ij}\,, \tag{2.65}$$

with the scalar functions $A(\ell)$ and $B(\ell)$. We decompose the velocity auto-correlation into the part parallel and perpendicular to $\boldsymbol{\ell}$, called longitudinal and transverse respectively. Hence

$$R_{ll}(\ell) = A(\ell)r^2 + B(\ell) = \left\langle v_i^2 \right\rangle f(\ell)\,, \tag{2.66}$$

$$R_{tt}(\ell) = B(\ell) = \left\langle v_i^2 \right\rangle g(\ell)\,, \tag{2.67}$$

with the scalar functions $f(\ell)$, $g(\ell)$, which fulfil $f(0) = g(0) = 1$. Using these definitions we can write for (2.65)

$$R_{ij}(\ell) = \frac{2}{3}E_{turb}\left(\frac{f(\ell) - g(\ell)}{\ell^2}\ell_i\ell_j + g(\ell)\delta_{ij}\right) \tag{2.68}$$

Besides the assumption of homogeneity and isotropy Kolmogorov designed his theory for an incompressible medium such that $\boldsymbol{\nabla} \cdot \mathbf{v} = 0$. It is easy to see that

$$\frac{\partial R_{ij}}{\partial \ell_i} = \frac{\partial R_{ij}}{\partial \ell_j} = \left\langle v_i(\mathbf{r})\frac{\partial v_j(\mathbf{r} + \boldsymbol{\ell})}{\partial \ell_j}\right\rangle = 0\,, \tag{2.69}$$

leading to

$$g(\ell) = f(\ell) + \frac{1}{2}\ell\frac{\mathrm{d}f}{\mathrm{d}\ell}\,. \tag{2.70}$$

In the next step we consider the Fourier transformation of the autocorrelation tensor

$$\phi_{ij}(k) = \frac{1}{(2\pi)^3}\int R_{ij}(\ell)\exp\left(i\mathbf{k}\cdot\boldsymbol{\ell}\right)\mathrm{d}^3\ell\,, \tag{2.71}$$

where we used the spherical symmetry in $\mathbf{k}$-space. We can make the same Ansatz for ϕ as in real-space (2.65)

$$\phi_{ij}(k) = C(k)k_i k_j + D(k)\delta_{ij} \tag{2.72}$$

and with the incompressibility condition in Fourier space

$$k_i\phi_{ij} = k_j\phi_{ij} = 0 \tag{2.73}$$

we get

$$D(k) = -C(k)k^2\,, \tag{2.74}$$

so that we can write ϕ as a function of only one scalar function $E(k)$

$$\phi_{ij}(k) = \frac{E(k)}{4\pi k^4}(k^2\delta_{ij} - k_i k_j) \,. \qquad (2.75)$$

The physical interpretation of ϕ becomes clear by considering the total kinetic energy

$$E_{turb} = \frac{1}{2}\left\langle v^2 \right\rangle = \frac{1}{2}R_{ii}(0) = \frac{1}{2}\int \phi_{ii}(k)\mathrm{d}^3k \,, \qquad (2.76)$$

where we sum over the index $i \in [x,\, y,\, z]$. Replacing $\mathrm{d}^3k = 4\pi k^2\mathrm{d}k$ we obtain

$$E_{turb} = \int_0^\infty E(k)\mathrm{d}k \qquad (2.77)$$

where $E(k)$ is the kinetic energy spectrum of turbulence.

Now we define velocity increments and structure functions

$$S_{ij}^p(\ell) = \left\langle |\delta v_{ij}(\ell)|^p \right\rangle = \left\langle |v_i(\mathbf{r} + \boldsymbol{\ell}) - v_j(\mathbf{r})|^p \right\rangle \,, \qquad (2.78)$$

known as the structure function of order p of the velocity increment $\delta v(\ell)$. For the second order we get

$$\left\langle |\delta v_{ij}|^2 \right\rangle = \left\langle v_i^2(\mathbf{r} + \boldsymbol{\ell}) \right\rangle + \left\langle v_j^2(\mathbf{r}) \right\rangle - 2\left\langle v_i(\mathbf{r} + \boldsymbol{\ell})v_j(\mathbf{r}) \right\rangle \,, \qquad (2.79)$$

which we can transform assuming homogeneity, isotropy and using equation (2.62) to

$$\frac{1}{2}S_{ij}^2(\ell) = \frac{2}{3}E_{turb} - R_{ij}(\ell) \,. \qquad (2.80)$$

To summarise, the autocorrelation, the power spectrum, and the second order structure function contain all exactly the same information, as they can be derived from each other. They connect the total amount of kinetic energy in turbulent motions with the scale dependent statistical properties of the velocity field, where the energy spectrum can be directly interpreted as energy density distribution as a function of the scale. The structure functions of different orders can be interpreted as the higher moments of the velocity increment PDF as a function of the lag variable ℓ. With the assumption (2.64) that the autocorrelation function vanishes at infinity one can show that the distribution functions converge to a Gaussian function on large scales (we do this in section 4.8 to normalize the measurements of the structure functions). The scaling exponents are playing in the interpretation now a crucial role, as they tell how the relation between the different orders change with the lag ℓ. So they tell how the form of the distribution function changes from a Gaussian PDF on large ℓ towards the peaky, intermittent PDF on small scales.

2.3   Bayesian statistics

One of the most fascinating experiences in life is observing a kid exploring its environment and surrounding. The learning process of assimilating information, cause relations and the connection between events in the external environment and then updating the existing knowledge based on that information is the natural behaviour of humans from the early beginning and determines our picture and interpretation of the world.
In modern science the analysed processes are getting more complex and complicated, but the learning process itself stays the same. Learning by revising beliefs in light of new information and data that become available lies also in the heart of the Bayesian framework. Bayes' theorem provides the formal means of putting that mechanism into action and the resulting probabilities are interpreted as degree of beliefs.

The Likelihood function

The Likelihood function is *the* fundamental quantity in the Bayesian framework and therefore we introduce it on an easy example. Assuming we observe the radioactive lifetime Θ of an isotope and we measure the number of decayed atoms in a sample per second x_1, $x_2...x_N$ in N measurements. The joint density function of a given value of Θ is

$$p(x_1,\, x_2...x_N|\Theta) \tag{2.81}$$

which defines the probability of observing the decay rates x_i in N measurements assuming a value of Θ and is known as the likelihood function. Assuming the number of decays follow a Poisson distribution $p(X = k) = \frac{\Theta^k}{k!}\exp\left(-\Theta\right)$ for $k \in \mathbb{N}$ then we can write down the likelihood

$$p(x_1,\, x_2...x_N|\Theta) = \Pi_{i=1}^{N}p(X = x_i|\Theta) = \Pi_{i=1}^{N}\frac{\Theta^{x_i}}{x_i!}\exp\left(-\Theta\right). \tag{2.82}$$

The *maximum likelihood* for the value of Θ yielding the set of measurements can be determined by setting the derivative of equation (2.82) in respect to Θ equal to zero. Knowing that a function and its logarithm have the same maxima and few steps of algebra result in

$$\Theta = \frac{\Sigma_{i=1}^{N}x_i}{N}\,, \tag{2.83}$$

which is the mean of the decay rates per time interval. Assuming that the decay rates are Gaussian distributed instead of Poisson and performing the

same calculations we end up with the well known formula for the mean and standard deviation.

Now, we return to the Bayesian theorem. It follows directly from the basic equations of conditional probability theory,

$$
\begin{aligned}
\mathcal{P}(\boldsymbol{\theta}, \mathbf{D}) &= \mathcal{P}(\boldsymbol{\theta}|\mathbf{D}) \, \mathcal{P}(\mathbf{D}) \\
&= \mathcal{P}(\mathbf{D}|\boldsymbol{\theta}) \, \mathcal{P}(\boldsymbol{\theta})
\end{aligned}
$$
$$
\Rightarrow \mathcal{P}(\boldsymbol{\theta}|\mathbf{D}) = \mathcal{P}(\mathbf{D}|\boldsymbol{\theta}) \, \mathcal{P}(\boldsymbol{\theta})/\mathcal{P}(\mathbf{D}) \,, \tag{2.84}
$$

where $\mathcal{P}(\mathbf{D}|\boldsymbol{\theta})$ is the above defined likelihood function of the set of parameters $\boldsymbol{\theta}$ given the set of data $\mathbf{D}$ and $\mathcal{P}(\boldsymbol{\theta})$ is the probability of the parameter called prior probability distribution. $\mathcal{P}(\mathbf{D})$ is the probability distribution of the set of data and acts here as a normalisation. We can transform this term a bit further

$$
\mathcal{P}(\mathbf{D}) = \int \mathrm{d}\boldsymbol{\theta} \; \mathcal{P}(\mathbf{D}, \boldsymbol{\theta}) \tag{2.85}
$$
$$
= \int \mathrm{d}\boldsymbol{\theta} \; \mathcal{P}(\mathbf{D}|\boldsymbol{\theta})\mathcal{P}(\boldsymbol{\theta}) \,. \tag{2.86}
$$

With these replacements Bayes rule reads:

$$
\underbrace{\mathcal{P}(\boldsymbol{\theta}|\mathbf{D})}_{\text{posterior}} = \underbrace{\mathcal{P}(\mathbf{D}|\boldsymbol{\theta})}_{\text{likelihood}} \quad \underbrace{\mathcal{P}(\boldsymbol{\theta})}_{\text{prior}} / \int \underbrace{\mathrm{d}\boldsymbol{\theta} \; \mathcal{P}(\mathbf{D}|\boldsymbol{\theta})\mathcal{P}(\boldsymbol{\theta})}_{\text{evidence}} \,. \tag{2.87}
$$

The likelihood function contains the model and the relation between the parameters. In the above stated example the model was that the number of decays can be described by a Poisson distribution. The prior reflects our beliefs of the behaviour of the parameters before taking the data into account. The priors can be divided into two groups the uninformative and the informative priors. If one has no preliminary beliefs and constrains on the parameter one takes an totally uninformed prior. In the above example we know that the number of decays per time has to be positive, so a wide prior containing this information is a uniform distribution from zero to infinity, stating that we believe that every value in $[0 : \infty]$ could be the true value with the same probability. The evidence works here just as an normalisation and is only used in the comparison of different models. The posterior provides a probability distribution for the parameters containing the information of the data under the assumption of the model. For a detailed introduction to Bayesian data analysis we refer the reader to standard textbooks like Gelman et al. (2004); Kruschke (2011); Wakefield (2013).

Chapter 3

Numerical setup and methods

3.1 Numerical setup

3.1.1 Properties of the simulations

To model the dynamics of a turbulent gaseous flow, we solve the equations of hydrodynamics, consisting of the continuity equation, the Euler equation with a stochastic forcing term $\mathbf{F}$ per unit mass, and the equation of state:

$$\frac{\partial \rho}{\partial t} + (\mathbf{v} \cdot \nabla)\rho = -\rho \nabla \cdot \mathbf{v}\,, \tag{3.1}$$

$$\frac{\partial \mathbf{v}}{\partial t} + (\mathbf{v} \cdot \nabla)\mathbf{v} = -\frac{\nabla p}{\rho} + \mathbf{F}\,, \tag{3.2}$$

$$p = \kappa \rho^{\Gamma}\,. \tag{3.3}$$

Here, ρ denotes the mass density, $\mathbf{v}$ the velocity field, p the pressure, κ the polytropic constant, and Γ the polytropic index. Observations indicate that the dense interstellar medium and molecular clouds behave as an isothermal flow due to efficient cooling processes (Elmegreen and Scalo, 2004). Accordingly, we simulate an isothermal medium throughout this study, assuming $\Gamma = 1$, $\kappa = c_s{}^2$, following $p = \rho c_s{}^2$, with the sound speed c_s.

We employ the FLASH code (version 3 and 4) (Fryxell et al., 2000; Dubey et al., 2008) to solve the set of partial differential equations (3.1) – (3.3). We use the piecewise parabolic method (PPM) (Colella and Woodward, 1984) in Chapter 4, 5 and HLL5R solver (Waagan et al., 2011) in Chapter 6 on a uniform three-dimensional grid. To distinguish between physical and numerical effects, we run simulations with 256^3, 512^3, and 1024^3 grid cells.

We compute the random forcing field $\mathbf{F}$ in Fourier space as described by (Schmidt et al., 2009),

$$d\widehat{\mathbf{F}}(\mathbf{k}, t) = \frac{F_0}{T_{ac}}(\mathbf{k}, T_{ac})\mathcal{P}^\zeta(\mathbf{k})d\mathbf{W}(t) - \widehat{\mathbf{F}}(\mathbf{k}, t)\frac{dt}{T_{ac}},\qquad(3.4)$$

where the $d\mathbf{W}(t)$ is a three-dimensional standardised Gaussian random increment. $\mathcal{P}^\zeta(\mathbf{k})$ is a projection tensor in Fourier space as a function of the wave number $\mathbf{k}$. In index notation, this operator is

$$\mathcal{P}^\zeta{}_{ij}(\mathbf{k}) = \zeta\mathcal{P}^\perp{}_{ij}(\mathbf{k}) + (1 - \zeta)\mathcal{P}^\parallel{}_{ij}(\mathbf{k}),\qquad(3.5)$$

where $\mathcal{P}^\perp = \delta_{ij} - k_ik_j/k^2$ and $\mathcal{P}^\parallel = k_ik_j/k^2$ are the fully solenoidal and compressive projection operators respectively and i, j are $\in [x, y, z]$. The forcing has finite autocorrelation time scale, T_{ac}, so that it is smooth in space and time. The forcing amplitude $F_0(\mathbf{k})$ is a three-dimensional power-law (parabolic)[1] function.   The forcing only occurs on the large integral scales $1 \leqslant |\mathbf{k}| \leqslant 2(\leqslant 3)^1$, peaking at $k = 1$ $(k = 2)$, which corresponds to (half of)[1] the box size L $(L/2)^1$, as we measure k in units of $2\pi/L$. The autocorrelation time-scale of the forcing algorithm is set equal to the dynamical time-scale $T_{ac} = T = L/(2c_s\overline{\mathcal{M}})$ and we adjust the amplitude of the forcing field, such that the root mean square Mach numbers are $\overline{\mathcal{M}} \approx 0.1, 0.5, 2, 5.5, 15$. As one of our goals is to study the influence of the forcing scheme, we use the projection tensor in Fourier space to get a purely solenoidal (divergence-free, $\nabla \cdot \mathbf{F} = 0$) and a purely compressive (curl-free, $\nabla \times \mathbf{F} = 0$) vector field.

We start with homogeneously distributed gas at rest and let it evolve for several dynamical time scales (15 or 10). The physical quantities in the simulations are scale-free so that we define $L = 1$, the mean mass-density $\langle\rho\rangle = 1$ and $c_s = 1$. We store the relevant quantities every $0.1\,T$ and the fluid reaches the equilibrium state after about three turbulent crossing times.

The parameters of these simulations are described in Konstandin et al. (2012a,b, 2014), and a detailed description of the forcing is presented in Schmidt et al. (2009) and Federrath et al. (2010).

3.1.2   Tracer particles

Tracer particles are analysed only in Chapter 4. We start with uniformly distributed tracer particles at rest. Afterwards they can move freely within the computational domain. The velocity and density of the tracer particles are calculated with a cloud-in-cell interpolation from the grid at the beginning of

---

[1]The description in the brackets refer to the study in Chapter 4 and 5, as we changed the forcing routine for the last study in Chapter 6.

each time step. Given the interpolated velocity, the tracer particles are then moved with an Euler method, based on the hydrodynamical time step. The tracers thus follow the gas flow in the Lagrangian frame of reference. Instead of the linear interpolation of the neighbouring grid points, a second-order (triangular-shaped cloud) and third-order (tricubic) space interpolation, as well as a higher-order temporal integration scheme (predictor-corrector type) were tested, but they did not lead to statistically significant differences. As the tracer particles have no influence on the fluid, they are passive tracers of the fluid motion.

3.2 Methods

3.2.1 Relation between the *Eulerian* and *Lagrangian* frameworks

Here we introduce two different kinds of time derivatives. The *Eulerian* derivative denoted by $\partial/\partial t$ is the differentiation at a fixed point in space, whereas the *Lagrangian* denoted by $\mathrm{d}/\mathrm{d}t$, is a differentiation of a quantity moving with a fluid element. Looking at a quantity $Q(\mathbf{X}) \in \mathbb{R}$ as a function of $\mathbf{X} \in \mathbb{R}^N$ the total differential is defined as

$$\mathrm{d}Q(\mathbf{X}) = \sum_{i=1}^{N} \frac{\partial Q(\mathbf{X})}{\partial X_i} \mathrm{d}X_i \tag{3.6}$$

and defining $\mathbf{X} \equiv (\mathbf{r}, t)$ it follows

$$\frac{\mathrm{d}Q}{\mathrm{d}t} = \frac{\partial Q}{\partial t} + \sum_{i=1}^{3} \frac{\partial Q}{\partial r_i} \frac{\mathrm{d}r_i}{\mathrm{d}t} = \frac{\partial Q}{\partial t} + \mathbf{v} \cdot \nabla Q \,, \tag{3.7}$$

which is a useful relation between the *Eulerian* and *Lagrangian* frameworks.

3.2.2 Helmholtz-decomposition theorem

We present here the Helmholtz-Decomposition theorem, as one aspect of this thesis is to analyse the influence of the different modes of a decomposed vector field on the statistical properties of supersonic turbulence. In summary it states that under specific circumstances every vector field $\mathbf{a}(\mathbf{r})$ is uniquely described by its source field $\nabla \cdot \mathbf{a}(\mathbf{r})$ and its curl field $\nabla \times \mathbf{a}(\mathbf{r})$ and can be expressed by the sum of these two fields.

Helmholtz-Decomposition theorem

Let $\mathbf{a}(\mathbf{r})$ be a vector field in $\mathbb{R}^3$, which is twice continuously differentiable, and $\mathbf{a}(\mathbf{r})$ vanishes faster than $1/r$ as $r \to \infty$. Then $\mathbf{a}(\mathbf{r})$ can be decomposed into a curl-free component and a divergence-free component:

$$\mathbf{a}(\mathbf{r}) = -\nabla\phi + \nabla \times \mathbf{A} \tag{3.8}$$

where

$$\phi(\mathbf{r}) = \frac{1}{4\pi} \int \frac{\nabla' \cdot \mathbf{a}(\mathbf{r}')}{|r - r'|} \mathrm{d}^3 r' \tag{3.9}$$

$$\mathbf{A}(\mathbf{r}) = \frac{1}{4\pi} \int \frac{\nabla' \times \mathbf{a}(\mathbf{r}')}{|r - r'|} \mathrm{d}^3 r' \tag{3.10}$$

If additionally the vector field $\mathbf{a}(\mathbf{r})$ vanishes as $r \to \infty$, then the decomposition is unique.

3.2.3   The power spectrum

The Fourier spectrum of the velocity field is defined as

$$\mathcal{P}(k)\mathrm{d}k = 4\pi k^2 \hat{\mathbf{v}}(k) \cdot \hat{\mathbf{v}}^*(k)\,\mathrm{d}k\,, \tag{3.11}$$

where $\hat{\mathbf{v}}$ is the Fourier-transformed velocity field and $\hat{\mathbf{v}}^*$ its complex conjugation. With this definition the integral over the whole k-range corresponds to the square of the Mach number,

$$\mathcal{M}^2 = \int_0^\infty \mathcal{P}(k)\mathrm{d}k\,, \tag{3.12}$$

and the zero'th mode contains the averaged velocity field for velocity components $i \in x, y, z$,

$$\langle v_i \rangle = \mathcal{P}_i(0) = \frac{1}{L^3} \int_0^\infty v_i(\mathbf{r})\,\mathrm{d}^3\mathbf{r}\,. \tag{3.13}$$

In addition to the above mentioned *total* spectrum, we calculate the spectra of the decomposed velocity field using the same decomposition as we use for the forcing field (3.5) and refer to these as the *longitudinal* and the *transverse* spectra for the curl-free and divergence-free velocity components, respectively.

3.2.4 Statistical Moments

In order to calculate the higher-order moments of the PDFs in Section 4.2, we use the following definition for the first four standardised central moments:

$$\text{mean} \qquad \langle q \rangle = \sum q\, p(q)\, \Delta_q$$

$$\text{standard deviation} \quad \sigma_q = \sqrt{\langle (q - \langle q \rangle)^2 \rangle}$$

$$\text{skewness:} \qquad \mathcal{S}_q = \frac{\langle (q - \langle q \rangle)^3 \rangle}{\sigma^3}$$

$$\text{kurtosis:} \qquad \mathcal{K}_q = \frac{\langle (q - \langle q \rangle)^4 \rangle}{\sigma^4}\,,$$

where Δ_q is the bin width of the PDF $p(q)$. With this definition a Gaussian has a skewness $\mathcal{S}_q = 0$ and a kurtosis $\mathcal{K}_q = 3$.

3.2.5 The Multivariate normal distribution

The multivariate normal distributed vector $\mathbf{x} \sim \mathcal{N}(\boldsymbol{\mu}, \boldsymbol{\Sigma})$, $\mathbf{x} \in \mathbb{R}^n$ has a density

$$p(\mathbf{x}|\boldsymbol{\mu}, \boldsymbol{\Sigma}) = (2\pi)^{n/2} |\boldsymbol{\Sigma}|^{-1/2} \exp\left(-\frac{1}{2}(\mathbf{x} - \boldsymbol{\mu})^T \boldsymbol{\Sigma}^{-1}(\mathbf{x} - \boldsymbol{\mu})\right), \qquad (3.14)$$

where $\boldsymbol{\mu} \in \mathbb{R}^n$ is the mean vector and $\boldsymbol{\Sigma} \in \mathbb{R}^{n \times n}$ is the positive semi-definite covariance matrix. The diagonal elements of $\boldsymbol{\Sigma}$ are the variances of the components of $\mathbf{x}$ and the off-diagonal elements are the covariances introduced in the definition of the correlation (2.61). As the indices i, j commute, $\boldsymbol{\Sigma}$ is symmetric and contains $n(n-1)/2$ independent elements. Two important properties, which follow from the definition, are. First, for any vector $\boldsymbol{\alpha} \in \mathbb{R}^n$ is the quantity $y = \boldsymbol{\alpha} \cdot \mathbf{x}$ (univariate) normal distributed. Second, it exist a vector $\mathbf{z} \in \mathbb{R}^m$ with *independent* standard normal random variables as components, a vector $\boldsymbol{\mu} \in \mathbb{R}^n$, and a matrix $\mathbf{A} \in \mathbb{R}^{n \times m}$ with

$$\mathbf{x} = \mathbf{A}\,\mathbf{z} + \boldsymbol{\mu}\,. \qquad (3.15)$$

The matrix $\mathbf{A}$ has to fulfil $\boldsymbol{\Sigma} = \mathbf{A}\mathbf{A}^T$ and m is the rank of $\boldsymbol{\Sigma}$, which defines the number of basis vector of the parameter space.

Chapter 4

Statistical properties of supersonic turbulence in the Lagrangian and Eulerian frameworks

The co-authors of this study are Christoph Federrath, Ralf S. Klessen and Wolfram Schmidt (Konstandin et al., 2012a). The simulations and the implementation of the tracer particles were provided by C. Federrath.

In this study we present a systematic analysis of the influence of different forcing types on the statistical properties of supersonic, isothermal turbulence in both the Lagrangian and Eulerian frameworks. We analyse a series of high-resolution, hydrodynamical grid simulations with Lagrangian tracer particles and examine the effects of solenoidal (divergence-free) and compressive (curl-free) forcing on structure functions, their scaling exponents, and the probability density functions of the gas density and velocity increments. Compressively driven simulations show a significantly larger density contrast, a more intermittent behaviour, and larger fractal dimension of the most dissipative structures at the same root mean square Mach number. We show that the absolute values of Lagrangian and Eulerian structure functions of all orders in the integral range are only a function of the root mean square Mach number, but independent of the forcing. With the assumption of a Gaussian distribution for the probability density function of the velocity increments on large scales, we derive a model that describes this behaviour.

4.1   Motivation

Knowledge of the statistical characteristics of turbulence is a key prerequisite for understanding turbulent flows on virtually all scales (Lesieur, 1993; Frisch, 1995). While common terrestrial flows are incompressible, astrophysical flows are highly supersonic and compressible. For example, the birth of stars in the interstellar medium is thought to be controlled by supersonic turbulence (Mac Low and Klessen, 2004; Scalo and Elmegreen, 2004; McKee and Ostriker, 2007). As turbulence is by definition a process characterised by a chaotic and irregularly fluctuating velocity field, there is a scale-dependent spatial and temporal correlation of fluid quantities (Ishihara et al., 2009). The scale-dependent energy, density and velocity distributions, and the dynamical evolution thereof, are strongly influenced by the properties of the turbulence. While large improvements were made in the understanding of incompressible turbulence in the last few years (e.g. with new techniques like superstatistics and Lagrangian statistics, Beck, 2004; Toschi and Bodenschatz, 2009), there are still open questions in our understanding of compressible turbulence. The non-local, inter-scale processes of compressible turbulence arising for example in shock fronts change the Richardson-Kolmogorov picture of the energy cascade of incompressible turbulence, where scale-locality is crucial for the existence of universal statistics in the inertial range. Basic questions as the existence of the inertial range, the associated scaling laws, and the influence of intermittency are still open. Guided by the idea of basic physical quantities like the momentum and the kinetic energy, there is a trend using mass-weighted velocity increments to describe turbulence in a compressible medium. For example, Kritsuk et al. (2007), Schmidt et al. (2008), and Galtier and Banerjee (2011) describe the intermittency appearing in their supersonic, compressible, numerical simulations with a phenomenological model using mass-weighted velocity increments. Since Lagrangian tracer particles are designed to follow the turbulent flow and thus the mass flux in numerical simulations, they are a powerful tool to study compressible turbulence, with an intrinsic mass-weighting. Furthermore, phenomenological models treating intermittency arising in compressible turbulence were developed in the last years. Boldyrev et al. (2002) used the multifractal phenomenological model of She and Leveque (1994), which describes the most dissipative structures in incompressible turbulence as filaments, and modified it such that the most dissipative structures are sheets instead of filaments. Nevertheless, despite of these improvements over the last years, the theoretical understanding of compressible turbulence is still poor and analytical derivations are rare.

Three spatial or temporal ranges have to be distinguished for turbulence: the

viscous dissipation range at small scales, the inertial range at intermediate scales, and the range above the turbulent injection scale, the so-called integral range. The velocity structure functions, an average of the difference of two velocities separated by an increment in space or time, increase from the dissipation range to the integral range. Here, we also consider the statistics of turbulence in the integral range, where temporal correlations of the velocity field are exponentially damped, and the structure functions saturate over several integral time scales. A complete understanding of the statistical properties in this range is necessary as a solid foundation for further studies of the complex and complicated behaviour of turbulence in the inertial range. In this paper we shed some light on this unattended topic. We compute Lagrangian statistics of the density and velocity fields of supersonic turbulence, using data from high-resolution, three-dimensional simulations of driven turbulence with up to 1024^3 grid cells and up to 512^3 tracer particles. By calculating probability density functions and structure functions, we analyse the sensitivity of compressible turbulence on the forcing of the turbulence. In particular, we compare two limiting cases of purely solenoidal (divergence-free) and purely compressive (curl-free) forcing. We present a detailed analysis of the scaling properties of the velocity structure functions and intermittency in the inertial subrange. We show that a simple analytic formula describes the saturated structure functions of all orders in the integral range, with the r.m.s. Mach number as single input parameter. This formula can be used to check the convergence of the structure functions.

4.2   General properties of the simulations

As discussed in Federrath et al. (2009, 2010) and Price and Federrath (2010), the fluid reaches an equilibrium state of fully-developed, supersonic turbulence after about two turbulent crossing times, $t \approx 2\,T$. We therefore restrict our analysis to times $t \geqslant 2\,T$. Figure 5.1 shows the time evolution of the mass-weighted r.m.s Mach number and the mass-weighted averaged density, calculated with the data of the tracer particles. As the tracer particles are advected by the flow, their density is correlated with the mass density. As a consequence, the average of a quantity over all tracer particles is mass-weighted. We denote quantities calculated with this quasi Lagrangian statistics with a subscript M. Figure 5.1 demonstrates that at $t \approx 2\,T$, a regime of statistically fully-developed turbulence is reached. The right panel of Figure 5.1 shows that the compressive forcing yields a nearly eight times larger mass-weighted mean density and fluctuations thereof. The mean values in-
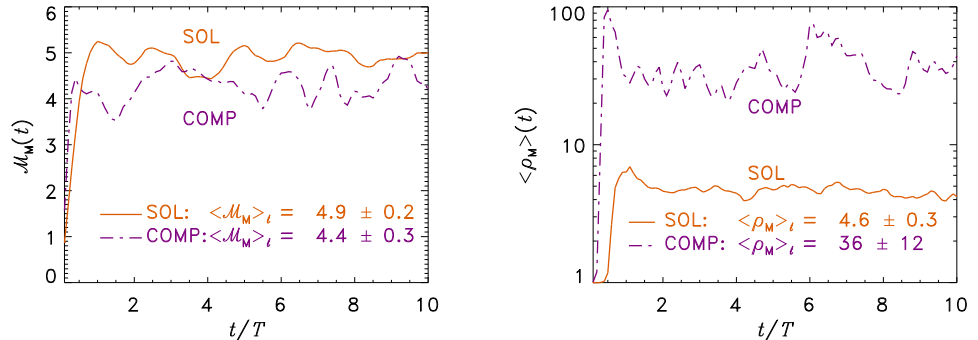
Figure 4.1: Mass-weighted r.m.s Mach number (left), and averaged mass-weighted density (right), as a function of the dynamical time, calculated by averaging over all tracer particles. Within the first $2\,T$, a statistically steady state was reached for both solenoidal (sol) and compressive (comp) forcing. The mean values were averaged over $t \in [2, 10]\,T$ and the errors are the $1\,\sigma$ variations in time.

dicated in Figure 5.1 are averaged over the interval $2\,T \leq t \leq 10\,T$, and the errors are the $1\,\sigma$ variations in time. In the state of fully-developed turbulence, the time-averaged r.m.s Mach number on the tracer particles is $\langle \mathcal{M}_{\mathrm{sol},M} \rangle_t = 4.9$ (subscript t for time average) with solenoidal forcing, and $\langle \mathcal{M}_{\mathrm{comp},M} \rangle_t = 4.4$ with compressive forcing. In Federrath et al. (2008, Table 1), the volume-weighted Mach number of this simulation was measured ($\langle \mathcal{M}_{\mathrm{sol},V} \rangle_t = 5.3$, $\langle \mathcal{M}_{\mathrm{comp},V} \rangle_t = 5.6$). Clearly, the intrinsic mass-weighting of the tracer particles influences the statistical properties, discussed in more detail below. The values of the volume-weighted and mass-weighted r.m.s. Mach number for the different forcings are summarised in Table 4.1 (first row). To illustrate the different flow patterns for solenoidal and compressive forcing, we show a randomly selected slice through the mid plane of the computational domain at $t = 6\,T$ in Figure 4.2. It shows the logarithm of the mass density computed on the grid cells in this slice, as well as the norm of the velocity of the tracer particles that are in one slice with thickness of 0.1 grid cells. Each dot represents a tracer particle with the colour corresponding to the norm of the velocity. The density fluctuations are more space-filling with solenoidal forcing, and have smaller amplitude, while compressive forcing yields larger voids and denser regions. The bottom panel of Figure 4.2 shows a magnification of a head-on collision of two flows that leads to a strong shock in the simulation with compressive forcing. The density field shows a sharp, well-defined shock front. In these compressed regions,
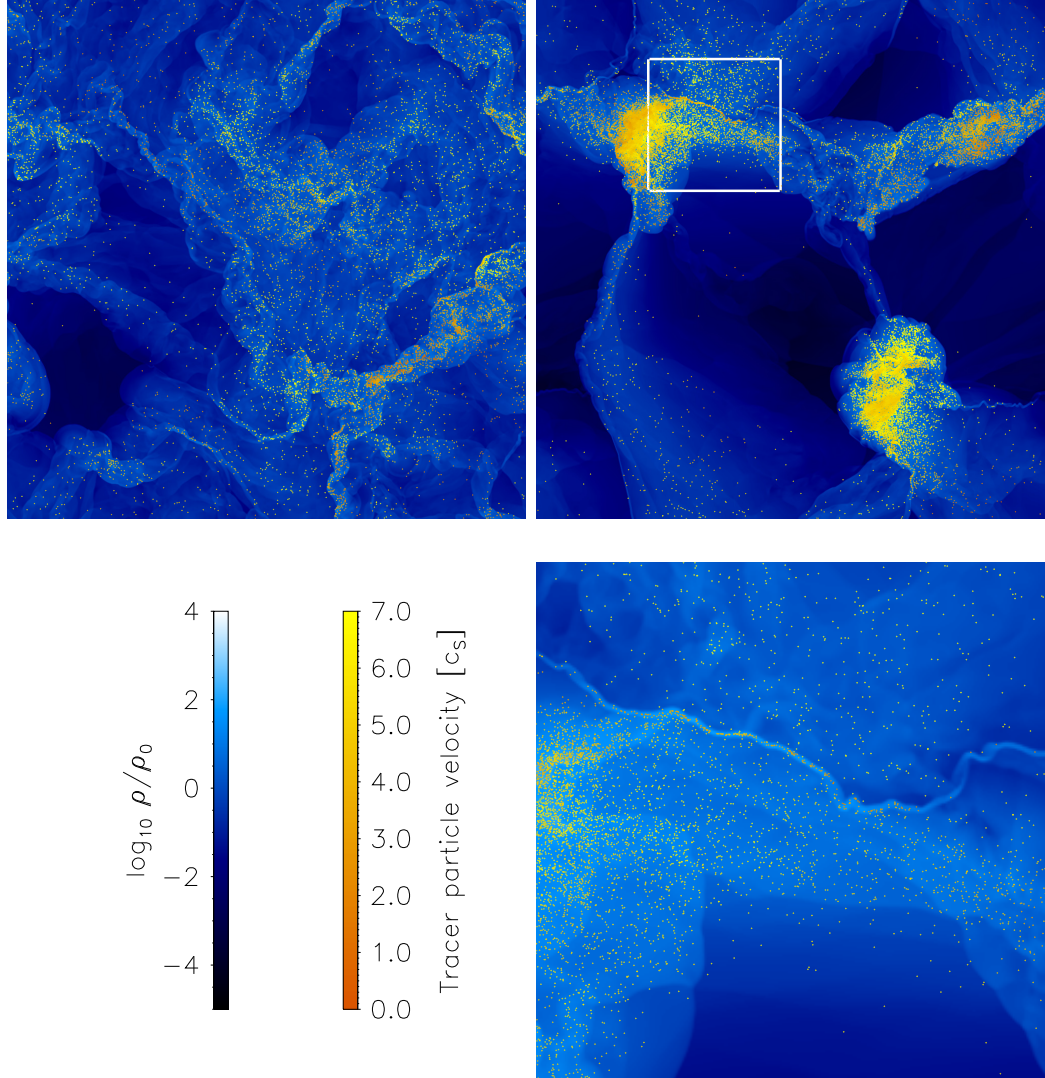
Figure 4.2: Top panels: Slice in the xy-plane at $z = 0.5$ and time $t = 6\,T$ as an example for the regime of statistically fully-developed, compressible turbulence. The logarithm of the mass density of the grid cells in this slice (blue) as well as the norm of the velocity of the tracer particles (red) in one slice with thickness of 0.1 grid cell are displayed for solenoidal (left) and compressive forcing (right). Bottom right: Magnified slice of a shock front in the simulation with compressive forcing (see white box in upper right panel).

the tracer particles accumulate and have a significantly lower Mach number, $\mathcal{M}_M \approx 1 - 2$. These stagnation points, showing a correlation of high density with low velocities (e.g. Ballesteros-Paredes et al., 2003; Klessen et al., 2005), are important in the theory of star formation (Mac Low and Klessen, 2004), as they are good candidates for the formation of dense-cores, which are the progenitors of individual stars and binary stellar systems. This correlation in the stagnation points causes the mass-weighted values of the Mach number to be smaller than the volume-weighted ones. Compressive forcing excites more head-on collisions and shock fronts, so this effect has a stronger influence in that case.

4.3   The probability density function of the gas density

The probability density function (PDF) of the gas density $p(\rho)$ and its standard deviation σ_ρ are important quantities in astrophysics. For instance, Padoan and Nordlund (2002) and Hennebelle and Chabrier (2008, 2009) relate the density PDF to the mass distribution of dense gas cores and stars. Padoan et al. (1997) and Passot and Vázquez-Semadeni (1998) have shown that the standard deviation grows proportional to the Mach number of the turbulent flow, if the density PDF is close to a log-normal distribution (see Price et al., 2011, for a recent, extended study). Federrath et al. (2010) demonstrated that the density PDF is not only influenced by the r.m.s Mach number, but also by the forcing parameter ζ, and presented a modification of the existing expression, which takes the ratio of solenoidal and compressive modes of the forcing into account. In many numerical experiments of driven, supersonic, isothermal turbulence with solenoidal and/or weakly compressive forcing, it was found that the density PDF is close to a log-normal distribution (e.g. , Padoan et al., 1997; Klessen, 2000; Lemaster and Stone, 2008; Federrath et al., 2008),

$$p(s) = \frac{1}{\sqrt{2\pi}\sigma_s} \exp\left(\frac{-(s - \langle s \rangle)^2}{2\sigma_s^2}\right), \tag{4.1}$$

where $s = \log_{10}(\rho/\langle\rho\rangle_V)$ is the logarithm of the density divided by the volume-weighted mean density. Li et al. (2003) argued that the mass-weighted density distribution is also a log-normal, with the same standard deviation as the volume-weighted distribution. With the assumption of a log-normal density PDF, the authors derived a relation between the mass-weighted and

the volume-weighted quantities,

$$\langle s \rangle_V = -\langle s \rangle_M = -\frac{\sigma_s^2}{2}. \qquad (4.2)$$

Figure 4.3 presents the time-averaged ($t \in [2, 10] \, T$) PDF of the quantity s_M, calculated on the tracer particles in linear (left panel) and logarithmic scaling (right panel). The first four standardised central moments (see Section 3.2.4) of the density PDF $p_M(s)$ are summarised in Table 4.1 together with the volume-weighted moments calculated in Federrath et al. (2010, Table 1). Compressive forcing yields a significantly broader mass-weighted density distribution with standard deviation, $\sigma_{s,M}$ about 1.5 times larger at the same volume-weighted Mach number than solenoidal forcing ($\sigma_{s,\mathrm{sol},M} = 1.23$, $\sigma_{s,\mathrm{comp},M} = 1.77$). The peak is shifted to larger values of the logarithmic density ($\langle s \rangle_{\mathrm{sol},M} = 0.81$, $\langle s \rangle_{\mathrm{comp},M} = 2.37$). The PDF is compatible with a Gaussian distribution for solenoidal forcing. However, the Gaussian fit (black dashed line) shows that the density PDF has weak non-Gaussian contributions in the wings of the distribution. On the other hand, in the density PDF obtained from compressive forcing, the discrepancy to the Gaussian distribution in both wings is more prominent. The deviations from the log-normal distribution for the compressive forcing is caused by both a physical and a numerical effect. Price and Federrath (2010) analysed the influence of measuring the density PDF by using a grid-based simulation and an SPH simulation and found that the PDF of the SPH particles increases slightly in the high-density tail with increasing resolution and decreases in the low-density tail. We expect that this effect will decrease the deviations from a log-normal distribution for both forcing types in our simulation as the resolution is increased. Federrath et al. (2010, Figure 6) analysed the volume-weighted density PDFs for resolutions of 256^3, 512^3, and 1024^3, showing that changing the resolution affects solenoidal and compressive forcing in roughly the same way. Schmidt et al. (2009) also argue that the deviations from a log-normal PDF produced by compressive forcing are a genuine effect. From this we can conclude that the stronger non log-normal features seen for compressive forcing likely have a physical origin rather than a purely numerical one. The higher moments of the distribution with compressive forcing ($\mathcal{S}_{\mathrm{comp},M} = -0.57$, $\mathcal{K}_{\mathrm{comp},M} = 3.50$) show larger deviations from the Gaussian values ($\mathcal{S} = 0$, $\mathcal{K} = 3$) than for solenoidal forcing ($\mathcal{S}_{\mathrm{sol},M} = -0.13$, $\mathcal{K}_{\mathrm{sol},M} = 2.95$). Checking the relation (4.2) between the mean value and the standard deviation demonstrates that for solenoidal forcing, the assumption of a log-normal PDF is nearly fulfilled ($\sigma_{s,\mathrm{sol},M}^2/2 = 0.76$). In contrast, we find larger discrepancy for compressive forcing ($\sigma_{s,\mathrm{comp},M}^2/2 = 1.57$). Measuring the volume-weighted PDF, Feder-

rath et al. (2010) also reported small deviations from a Gaussian distribution for solenoidal forcing ($\mathcal{S}_{\mathrm{sol},V} = -0.10$, $\mathcal{K}_{\mathrm{sol},V} = 3.03$) and larger deviations for compressively-driven turbulence ($\mathcal{S}_{\mathrm{comp},V} = -0.26$, $\mathcal{K}_{\mathrm{comp},V} = 2.91$). The mass-weighted quantities show larger discrepancy from the Gaussian values than the volume-weighted quantities.

Padoan et al. (1997) and Passot and Vázquez-Semadeni (1998) motivated a linear relation between the r.m.s Mach number and the standard deviation of the linear density,

$$\sigma_\rho/\rho_0 = b\,\mathcal{M}\,, \tag{4.3}$$

with a proportionality constant b. Several measurements of b were obtained from different simulations and with different types of forcing, and yielded b between 0.26 and 1.05 (Passot and Vázquez-Semadeni, 1998; Li et al., 2003; Kritsuk et al., 2007; Beetz et al., 2008; Federrath et al., 2008; Schmidt et al., 2009; Price et al., 2011). From the distribution $p_M(s)$ shown in Figure 4.3, we calculate $p_M(\rho)$. Since equation (4.3) was derived with volume-weighted quantities, we have to transform our results using the relation (see, Li et al., 2003),

$$p_M(\rho) \propto \frac{\mathrm{d}M}{\mathrm{d}V}\frac{\mathrm{d}V}{\mathrm{d}\rho} \propto \rho\,p_V(\rho)\,, \tag{4.4}$$

where $p_M(\rho)$ and $p_V(\rho)$ are the mass-weighted and the volume-weighted PDFs of the gas density, respectively. We find $\sigma_{\rho,\mathrm{sol},V} = 1.90$ for purely solenoidal and $\sigma_{\rho,\mathrm{comp},V} = 6.03$ for purely compressive forcing. With the volume-weighted Mach number of this simulation, we get $b_{\mathrm{sol}} = 0.36$ for solenoidal forcing and $b_{\mathrm{comp}} = 1.08$ for compressive forcing, in good agreement with Federrath et al. (2008).

4.4   Velocity increments and structure functions

In order to calculate the increments, we use the following definition of the time-dependent, Lagrangian velocity increment

$$\delta v_i^m(t,\tau) = v_i^m(t+\tau) - v_i^m(t), \tag{4.5}$$

where τ is a temporal increment and $v_i^m(t)$ is the velocity in spatial direction $i \in \{x,y,z\}$ of the mth tracer particle at the time t. The space-dependent, Eulerian velocity increments are defined as

$$\delta v_i^{mn}(\mathbf{r},\boldsymbol{\ell}) = v_i^m(\mathbf{r}+\boldsymbol{\ell}) - v_i^n(\mathbf{r}) \tag{4.6}$$

	solenoidal		compressive	
	mass-weighted	volume-weighted	mass-weighted	volume-weighted
$\mathcal{M}$	4.9 ± 0.2	5.3 ± 0.2	4.4 ± 0.3	5.6 ± 0.3
$\langle s \rangle$	0.81 ± 0.04	-0.83 ± 0.05	2.37 ± 0.24	-3.40 ± 0.43
σ_s	1.23 ± 0.03	1.32 ± 0.06	1.77 ± 0.09	3.04 ± 0.24
$\mathcal{S}_s$	-0.13 ± 0.05	-0.10 ± 0.11	-0.57 ± 0.17	-0.26 ± 0.20
$\mathcal{K}_s$	2.95 ± 0.07	3.03 ± 0.17	3.50 ± 0.33	2.91 ± 0.43

Table 4.1: Mass-weighted and volume-weighted r.m.s. Mach number (first row) and the first four standardised central moments of the PDF $p_M(s)$ (column 1 and 3) and $p_V(s)$ (column 2 and 4) for solenoidal and compressive forcing. These quantities are averaged in time when the equilibrium state of fully-developed, supersonic turbulence is reached (see Section 4.2 and 4.3) and the errors are the standard deviation in time.
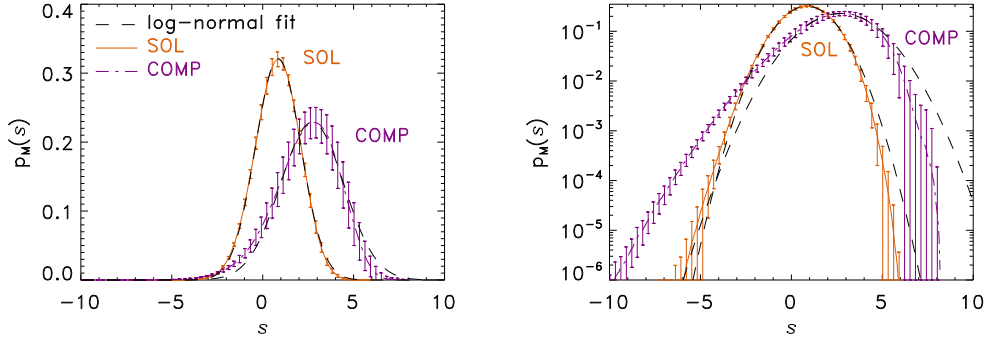
Figure 4.3: Mass-weighted PDF $p_M(s)$ of the logarithmic mass density $s = \log_{10}(\rho/\langle\rho\rangle_V)$ for solenoidal (solid line) and compressive (dashed-dotted line) forcing in linear (left panel) and logarithmic scaling (right panel), calculated on the tracer particles. The PDFs are calculated for 81 time steps in the state of fully-developed turbulence $t \geqslant 2T$ and averaged. The error bars indicate the standard deviation of the temporal fluctuations. The dashed lines show log-normal fits with the mean value and the standard deviation as fitting parameters.

$$\delta v_{\parallel}^{mn}(\mathbf{r}, \boldsymbol{\ell}) = v_{\parallel}^{m}(\mathbf{r} + \boldsymbol{\ell}) - v_{\parallel}^{n}(\mathbf{r}) \,, \tag{4.7}$$

where $\mathbf{r}$ is the position of the tracer n, $\boldsymbol{\ell}$ is the spatial increment between the tracer particles m and n, and $v_{\parallel} = \mathbf{v} \cdot \hat{\boldsymbol{\ell}}$ with $\hat{\boldsymbol{\ell}} = \boldsymbol{\ell}/\ell$ being the unit vector in the direction $\boldsymbol{\ell}$. The Lagrangian structure function (LSF)

$$LS^{p}(\tau) = \langle \langle |\delta v_x^m(t,\tau)|^p \rangle_m + \langle |\delta v_y^m(t,\tau)|^p \rangle_m + \langle |\delta v_z^m(t,\tau)|^p \rangle_m \rangle_t / 3 \tag{4.8}$$

is obtained by averaging the velocity increments over the different tracer particles m, the three directions of the coordinate system x, y, z and over $t \in [2, 10]\, T$. This is reasonable because of the time invariance and isotropy in the state of fully-developed turbulence.

In practise, we randomly select 5×10^6 tracer particles for all 801 time samples with $t \geqslant 2\,T$ in the fully-developed state for the averaging procedure (4.8). We checked the validity of this approach by doing these calculations also with all 512^3 tracer particles for one time-line starting at $t = 2\,T$ to ensure that the used number of sampling pairs has no statistically significant influence on our results (see Appendix 4.11). For calculating the Eulerian structure functions (ESFs)

$$ES^p(\ell) \equiv \langle \langle |\delta v_x^{mn}(\mathbf{r},\ell)|^p \rangle_{mn} + \langle |\delta v_y^{mn}(\mathbf{r},\ell)|^p \rangle_{mn} + \langle |\delta v_z^{mn}(\mathbf{r},\ell)|^p \rangle_{mn} \rangle_t / 3 \tag{4.9}$$

$$ES_{\parallel}^p(\ell) \equiv \langle |\delta v_{\parallel}^{mn}(\mathbf{r},\ell)|^p \rangle_{mn,t} \tag{4.10}$$

the simulation box was divided in 16^3 sub boxes. For m, a fixed number of tracer particles is chosen homogeneously distributed over all sub boxes. To obtain a constant sampling of the ESF with ℓ, for each m, a subset $\propto 1/r^2$ of tracer particles of every sub box is selected for n, where r is the distance from m to the centre of the sub box. As the number of sub boxes increases proportional to r^2, this procedure ensures that for each lag ℓ, roughly the same number of sampling pairs is used. The selection procedure is normalised in a way that for m, nearly the same number of tracer particles is selected as for n. The ESFs are calculated for 81 snapshots in time intervals of $\Delta t = T/10$ each with about 10^{10} sampling pairs. We tested our results with different numbers of sub boxes, where with insufficient sub boxes ($\lesssim 8^3$) we have to calculate the ESFs with many more sampling pairs to get a good statistic on the smallest scales. Using more than 16^3 sub boxes showed no effective improvement of the distribution. With 16^3 sub boxes, we calculate the ESFs with different numbers of sampling pairs to ensure that increasing the sampling pairs has no statistically significant influence on our results. We provide detailed convergence tests in Appendix 4.11. Since all increments are calculated on the tracer particles, the structure functions are intrinsically mass-weighted.

4.5 The probability density functions of velocity increments

The simplest set of correlation functions to quantify the statistical properties in a compressible, supersonic turbulent flow is the distribution of the velocity increments and its higher moments, the structure functions, defined by (4.8 to 4.10). The deviation of the structure function scaling exponents from the predicted values of the Kolmogorov model (Kolmogorov, 1941b) is an effect of intermittency (e.g., She and Leveque, 1994). A property of intermittency is that the PDFs of the velocity fluctuations become more and more non-Gaussian on smaller and smaller scales (Gotoh et al., 2002; Mordant et al., 2002).

Figure 4.4 shows the PDF of the velocity increment δv_i in the Lagrangian framework for five temporal increments $\tau \in \{0.01, 0.08, 0.4, 2, 4\}T$ and in the Eulerian framework for six spatial increments $\ell \in \{0.006, 0.02, 0.06, 0.12, 0.25, 0.49\}L$. The PDFs follow a Gaussian distribution for $\tau \to T$ and $\ell \to L$. Decreasing the spatial or temporal increment, the Gaussian PDFs vary continuously towards distributions with exponential wings indicating the intermittent behaviour of the turbulent velocity field. Figure 4.5 shows the kurtosis (see Section 3.2.4) of the distributions of the Lagrangian (left panel) and Eulerian (right panel) velocity increments, calculated with the structure functions

$$\mathcal{K}(\tau) = LS^4(\tau)/[LS^2(\tau)]^2 \qquad (4.11)$$

(solid and dash-dotted lines) and the values calculated with the PDFs (crosses and stars). The kurtosis can be used as a measure for the deviations of the distributions of the velocity increments from a Gaussian distribution. In the Lagrangian framework, the kurtosis obtained with solenoidal forcing converges towards the Gaussian value ($\mathcal{K} = 3$) on times comparable with the dynamical time scale, $\tau \approx 1\,T$. The compressive forcing yields PDFs converging already on smaller temporal lags, $\tau \approx 0.7\,T$ than solenoidal forcing. Compressive forcing develops a more intermittent behaviour with larger kurtosis than the solenoidal forcing for times $\tau \lesssim 0.08\,T$. As the non-Gaussian wings of PDFs of the density and/or velocity is caused by intermittency (see Federrath et al., 2010), this analysis of the kurtosis and the more intermittent behaviour of the compressive forcing confirm our observation of the density PDF and its deviation from the log-normal distribution (see Section 4.3).

In the Eulerian framework, compressive forcing yields a more intermittent behaviour with a larger kurtosis on nearly all spatial scales than solenoidal forcing. However, the kurtosis obtained with compressive forcing converges at the same scale ($\ell \approx 0.23\,L$) towards the Gaussian value as the kurtosis of
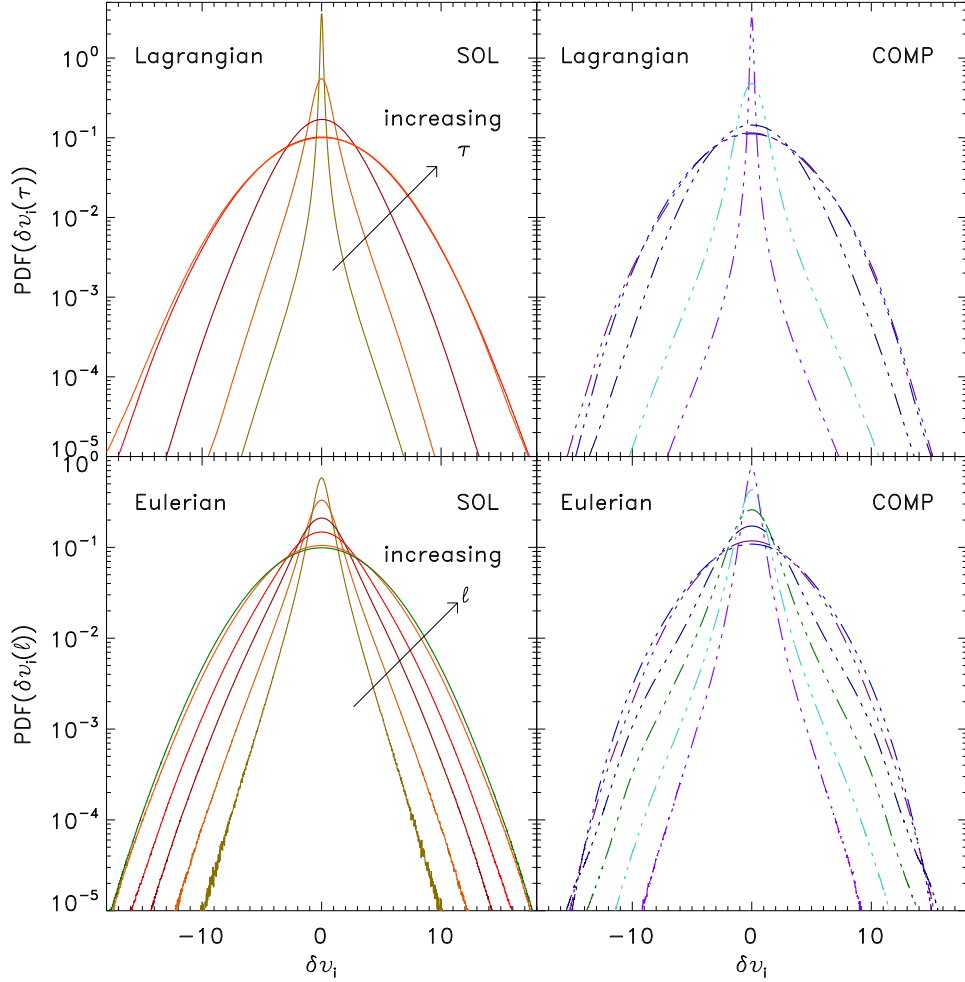
Figure 4.4: Top panel: PDFs of the velocity increment δv_i in the Lagrangian framework for solenoidal (left panel) and compressive forcing (right panel). It shows the PDFs with five different temporal increments $\tau \in \{0.01, 0.08, 0.4, 2, 4\}T$. Bottom panel: PDFs of the velocity increment δv_i in the Eulerian framework for solenoidal (left panel) and compressive forcing (right panel). It shows the PDFs with six different spatial increments $\ell \in \{0.006, 0.02, 0.06, 0.12, 0.25, 0.49\}L$. For small temporal or spatial lags, τ and ℓ, respectively, the PDFs differ from a Gaussian distribution because of intermittency. For large τ or ℓ, they converge towards a Gaussian distribution.
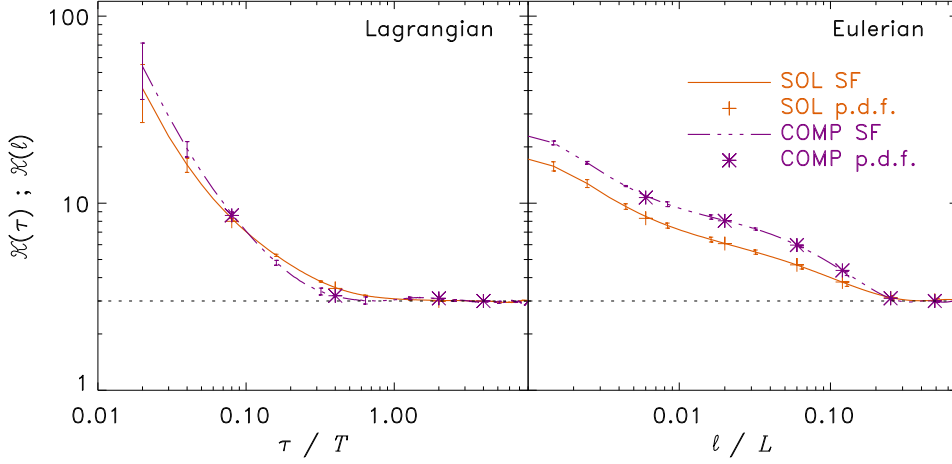
Figure 4.5: Kurtosis as a function of the temporal or spatial increment τ (left) and ℓ (right). The solid and dashed-dotted lines are respectively, the values for solenoidal and compressive forcing, calculated from (4.11). The crosses and stars are respectively the values for solenoidal and compressive forcing, calculated with the five PDFs shown in Figure 4.4. The horizontal, dotted line is the value of a Gaussian distribution.

the solenoidal forcing. Comparing the kurtosis of the Lagrangian and Eulerian structure functions strengthens the conclusion that Lagrangian statistics are more intermittent than Eulerian ones (here shown for two limiting types of forcing) as already observed by Benzi et al. (2010), but only for purely solenoidal forcing. In the region, where the kurtosis is converged towards the Gaussian value ($\tau \geqslant 2.5\,T$ for the Lagrangian framework and $\ell \geqslant 0.4\,L$ for the Eulerian framework), we average the structure functions to calculate the mean value of the saturated structure functions, as discussed in Section 4.6.

4.6 Lagrangian and Eulerian structure functions

Figure 4.6 shows the LSF and ESF up to order $p = 7$ for solenoidal and compressive forcing. We calculate the saturation values of the structure functions on the largest scales by averaging them in the range $\tau \in [2.5, 5]\,T$ for the LSFs and $\ell \in [0.4, 0.7]\,L$ for the ESFs. The result is displayed as

black lines in Figure 4.6. The compressive forcing yields structure functions that converge to Gaussian values already on smaller scales, as observed in Figure 4.5. For the two forcings, the saturation values are different. This can be explained with the different mass-weighted r.m.s Mach number $\mathcal{M}_M$, observed in Figure 5.1, because the structure functions S of order p for infinite increments are $S^p(\infty) \propto \mathcal{M}_M^p$ (see discussion in Section 4.8).

In turbulence theory, the structure functions follow a power law in the inertial range

$$LS(p) \propto \tau^{\xi(p)}, \quad ES(p) \propto \ell^{\zeta(p)}, \tag{4.12}$$

with the scaling exponents $\xi(p)$ and $\zeta(p)$. To calculate these scaling exponents, we use the inertial range as constrained by Federrath et al. (2009, 2010) ($0.067 \lesssim \ell/L \lesssim 0.2$), and transform it to the Lagrangian framework ($0.16 \lesssim \tau/T \lesssim 0.34$) with $\tau \propto \ell^{2/3}$. This relation follows directly from the Kolmogorov *four-fifth* law (e.g., Frisch, 1995), implying that the third-order structure function scales linearly with ℓ in the Eulerian framework. In Burgers turbulence, $\tau \propto \ell$, which follows from the assumption of a constant averaged energy transport through the scales, $\bar{\epsilon} \propto E(\ell)/\tau \propto v(\ell)^2/\tau$, and assuming Burgers scaling for the second-order velocity increment, $\delta v^2(\ell) \propto v^2(\ell) \propto \ell$. Using Burgers scaling for τ in the transformation of the inertial range leads to ($0.067 \lesssim \tau/T \lesssim 0.2$) in the Lagrangian framework. The so-called method of extended self-similarity (ESS) proposed by Benzi et al. (1993) allows for an increased scaling range between the smallest scales, influenced by the resolution, and the largest scales with a direct influence of the forcing. Using ESS, we thus extend the fitting range to $0.067 \lesssim \tau/T \lesssim 0.34$, which covers both the transformation with $\tau \propto \ell^{2/3}$ and $\tau \propto \ell$. For the Eulerian structure functions, we extended the scaling range to ($0.05 \lesssim \ell/L \lesssim 0.22$) for which we obtain a reasonable power-law scaling with ESS. Figure 4.7 shows the ESS scaling plots, i.e., plots of the logarithm of the structure functions calculated with equations (4.8) and (4.9) for the different orders as a function of the logarithm of the second- and third-order structure function in the Lagrangian and Eulerian framework, respectively. The black lines indicate linear fits for the ESS-measurement of the relative scaling exponents,

$$Z_L(p) = \frac{\xi(p)}{\xi(2)}, \quad Z_E(p) = \frac{\zeta(p)}{\zeta(3)}, \tag{4.13}$$

which are summarised in Table 4.2 for the Lagrangian framework (2th and 3th columns) and the Eulerian framework (5th and 6th columns) for solenoidal and compressive forcing, respectively.

To compare our results with data from incompressible turbulence, we refer in Table 4.2 to the data of numerical simulations of subsonic turbulence published by Benzi et al. (2010, Table 2, Reynolds$_\lambda \sim 600$, BBFLT10)

	Lagrangian			Eulerian				
p	$Z_L(p)$ sol.	$Z_L(p)$ comp.	BBFLT10 comp.	$Z_E(p)$ sol.	$Z_E(p)$ comp.	SFK08 sol.	SFK08 comp.	GFN02 (transversal)
1	0.57 ± 0.02	0.55 ± 0.04		0.422 ± 0.008	0.45 ± 0.02	0.539	0.605	0.369 ± 0.004
2	1.0	1.0	1.0	0.75 ± 0.02	0.78 ± 0.03	0.840	0.869	0.701 ± 0.01
3	1.30 ± 0.05	1.30 ± 0.09		1.0	1.0	1.0	1.0	0.998 ± 0.02
4	1.51 ± 0.07	1.5 ± 0.1	1.66 ± 0.02	1.20 ± 0.04	1.13 ± 0.07	1.080	1.066	1.26 ± 0.03
5	1.67 ± 0.09	1.6 ± 0.1		1.36 ± 0.05	1.19 ± 0.09	1.112	1.100	1.49 ± 0.04
6	1.8 ± 0.1	1.6 ± 0.2	2.10 ± 0.10	1.49 ± 0.07	1.2 ± 0.1	–	–	1.69 ± 0.05
7	1.9 ± 0.1	1.6 ± 0.2		1.61 ± 0.09	1.2 ± 0.2	–	–	1.86 ± 0.05

Table 4.2: Relative scaling exponents of the structure functions $LS^p(\tau)$ and $ES^p(\ell)$ calculated with the ESS method (Benzi et al., 1993) for solenoidal and compressive forcing in the Lagrangian (2th and 3th columns) and Eulerian (5th and 6th columns) frameworks. For a comparison with the scaling exponents of the structure functions in an incompressible turbulent medium, we refer to the data of numerical simulations published by Benzi et al. (2010) (BBFLT10, 4th column) and Gotoh et al. (2002) (GFN02, 9th column). The 7th and 8th columns show the relative scaling exponents of the transversal structure function of our simulation, but calculated with the velocities measured on the grid and mass-weighted with $\rho^{1/3}$ published in Schmidt et al. (2008)(SFK08).

and Gotoh et al. (2002, Table 3, Reynolds$_\lambda$ = 381, GFN02). We only show the data of the transverse structure functions of GFN02 in the Eulerian framework, because the differences between the longitudinal and transverse structure function are negligible compared to the differences between the supersonic and the subsonic results. We expect that our results of the structure function, averaged over the three directions of the coordinate system are in-between the results of the longitudinal and transverse structure function. Additionally, we compare our results calculated with tracer particles, discussed here, with the results of the same simulations, but calculated with the $\rho^{1/3}$ mass-weighted velocities measured on the grid published by Schmidt et al. (2008) (SFK08, 7th and 8th columns). These scaling exponents are also calculated for the transverse structure functions. The mass-weighting $\rho^{1/3}$, used by many authors (see e.g., Kritsuk et al., 2007; Kowal and Lazarian, 2007; Schmidt et al., 2008; Galtier and Banerjee, 2011), follows from the assumption of a constant mean volume energy transfer rate in a statistically steady state, $\rho v^2 v/\ell$, so that $\rho v^3 \propto \ell$. With the data in Table 4.2 we can analyse the influence of the different forcings in each framework. The relative scaling exponents show only a significant difference between the scaling behaviour of the solenoidal and compressible forcing in the Lagrangian framework for the highest order. The scaling exponents of the compressive forcing are slightly below the scaling exponents of the solenoidal forcing for higher orders. However, in the Eulerian framework, this effect is stronger and the compressive forcing causes scaling exponents to stay nearly constant above an order $p > 4$, such that there is a significant difference between the scaling exponents of the solenoidal and compressive forcing. With the measured scaling exponents, we can quantify the intermittency in the different frameworks by calculating the differences to the predicted Kolmogorov (1941b, K41) scaling. In the Lagrangian framework and for the highest order, $p = 7$, the scaling exponents are $46 \pm 3\%$ and $54 \pm 6\%$ smaller than the K41 value for the solenoidal and compressive forcing, respectively. In the Eulerian framework, the scaling exponents are $31 \pm 4\%$ and $49 \pm 9\%$ smaller than the K41 value. For solenoidal forcing, the scaling exponents show a more intermittent behaviour in the Lagrangian framework than in the Eulerian one. This is consistent with our analysis of the kurtosis in Figure 4.5 and the results of Benzi et al. (2010). For compressive forcing, we have an intermittency of the same order for both frameworks. The intense density fluctuations in the simulation with compressive forcing cause a more intermittent behaviour and scaling exponents that deviate stronger from the K41 values. The stronger influence of the compressive forcing on the intermittency in the Eulerian framework is an important result that needs further studies.
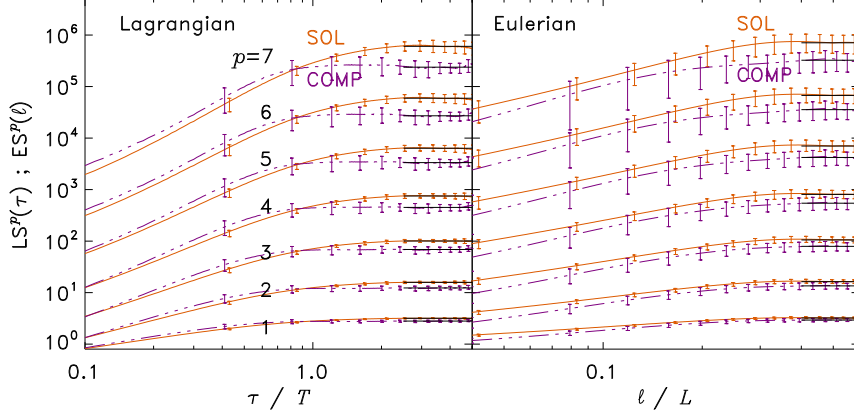
Figure 4.6: Lagrangian (left) and Eulerian (right) structure functions up to the order of $p = 7$ for solenoidal and compressive forcing, calculated with the velocity increment of the tracer particles. The error bars of the structure functions indicate the standard deviation in time. To calculate the absolute values of the saturated structure functions, the Lagrangian structure functions were averaged in the range $\tau \in [2.5, 5]\, T$, and the Eulerian structure functions were averaged in the range $\ell \in [0.4, 0.7]\, L$, indicated by the horizontal black lines in the integral range.

To estimate the influence of shocks and other non-local, inter-scale processes arising in supersonic, compressible turbulence, we compare our results with the data of other subsonic, incompressible simulations. Our scaling exponents are below those for incompressible media in both frameworks and are significantly different from the data of BBFLT10 and GFN02. This indicates a more intermittent behaviour in our supersonic, compressible, turbulent flow, which is even stronger for the simulations with compressive forcing. The comparison of the scaling exponents of the tracer particles with the $\rho^{1/3}$ mass-weighted results of the grid in the Eulerian framework shows that the $\rho^{1/3}$ multiplier does not have the same effect as the averaging over tracer particles. The intrinsic mass-weighting of the tracer particles shows a less intermittent behaviour for both forcings than the results of SFK08.
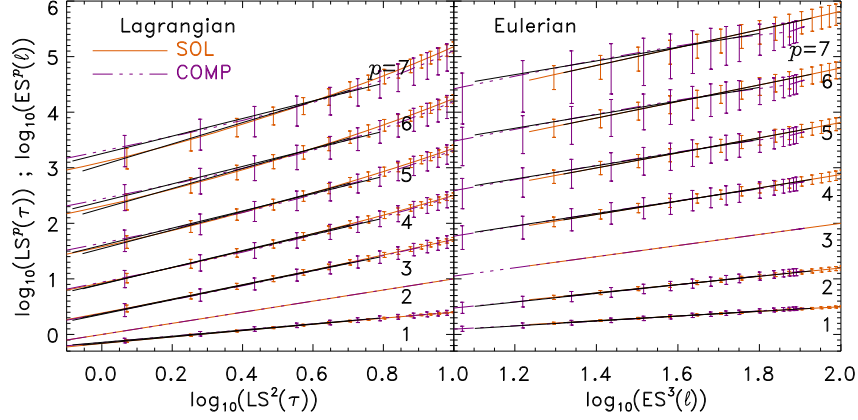
Figure 4.7: Extended self-similarity for the Lagrangian (left panel) and Eulerian (right panel) structure function for solenoidal and compressive forcing. The black lines indicate a linear fit for the calculation of the relative scaling exponents, which are summarised in Table 4.2.

4.7   Intermittency models for inertial range scaling

With the relative scaling exponents of the last Section, we can compare our results with the predictions of intermittency models. We use the generalised equation of the phenomenological model of She and Leveque (1994) introduced by Dubrulle (1994) for the scaling exponents in the Eulerian framework

$$Z_E(p) = (1 - \Delta_E)\frac{p}{3} + \frac{\Delta_E}{1 - \beta_E}(1 - \beta_E^{p/3}) \, . \tag{4.14}$$

With the assumptions $\tau \propto \ell^{2/3}$ and $LS^p \propto \langle \epsilon_\tau^{p/2} \rangle \tau^{p/2}$, where $\langle \epsilon_\tau^p \rangle$ are the moments of the energy dissipation at the time scale τ, one can show a similar equation for the Lagrangian framework, using the same arguments and derivations of She and Leveque (1994):

$$Z_L(p) = (1 - \Delta_L)\frac{p}{2} + \frac{\Delta_L}{1 - \beta_L}(1 - \beta_L^{p/2}) \, . \tag{4.15}$$

For simplicity we use $\tau \propto \ell^{2/3}$ for the transformation into the Lagrangian framework, instead of $\tau \propto \ell$, and treat the influence of compressibility in both frameworks by having different values for Δ and β compared to the K41 theory (see e.g., Boldyrev et al., 2002; Schmidt et al., 2008). Figure 4.8

shows the measured scaling exponents and the fits with equation (4.14) and (4.15). For the fitting procedure we follow the idea of Schmidt et al. (2008, 2009) and set $\Delta = 1$, which follows from Burgers scaling, $\tau \propto \ell$, as used in the last Section, leaving us with only one free fitting parameter. With the measured β we can calculate the co-dimension of the most dissipative structures $C = \Delta/(1-\beta)$, which is connected to the actual dimension of the most dissipative structures via $D = 3 - C$. The latter quantifies how volume-filling the most dissipative structures are in the turbulent medium. From our fits we get $D_{L,\mathrm{sol}} = 0.87$, $D_{L,\mathrm{comp}} = 1.17$ in the Lagrangian framework and $D_{E,\mathrm{sol}} = 1.11$, $D_{E,\mathrm{comp}} = 1.55$ in the Eulerian one. In the Eulerian framework, the most dissipative structures are between filamentary structures ($D = 1$, as in She and Leveque (1994)) and sheet-like structures ($D = 2$, as proposed by Boldyrev et al. (2002) for the Kolmogorov-Burgers model). In the Lagrangian framework and for solenoidal forcing, the most dissipative structures are close to filamentary structures. Compressive forcing yields a larger fractal dimension than solenoidal forcing in both frameworks. Although the whole turbulent flow is more space filling for solenoidal forcing, as observed in Figure 4.2, the most dissipative structures of the compressive forcing have a larger dimension and are thus more space filling. However, it is unclear how to interpret these results in the one-dimensional Lagrangian framework of temporal increments rather than spatial increments as in the Eulerian framework. In the Eulerian framework, we can compare our results with the dimensions we get by calculating the scaling exponents with the mass-weighted velocities of the grid. Schmidt et al. (2008) measured $D_{\mathrm{sol}} = 1.82$ and $D_{\mathrm{comp}} = 1.92$, showing the same trend between the solenoidal and compressive forcing, but larger than the values we measured on the tracer particles. The reason for these differences is the more intermittent behaviour of the scaling exponents, as discussed above (see also Table 4.2).

4.8 A statistical theory of the large-scale velocity increments

In this Section, we show that the statistical properties of the velocity increments in a turbulent flow on large scales can be described with only one parameter, the r.m.s Mach number. This is valid for velocity increments in the Lagrangian and Eulerian framework. The structure functions defined by (4.8) to (4.10) can be expressed as the moments of the PDFs of the velocity increment, which are functions of τ or ℓ, so we can write for a general
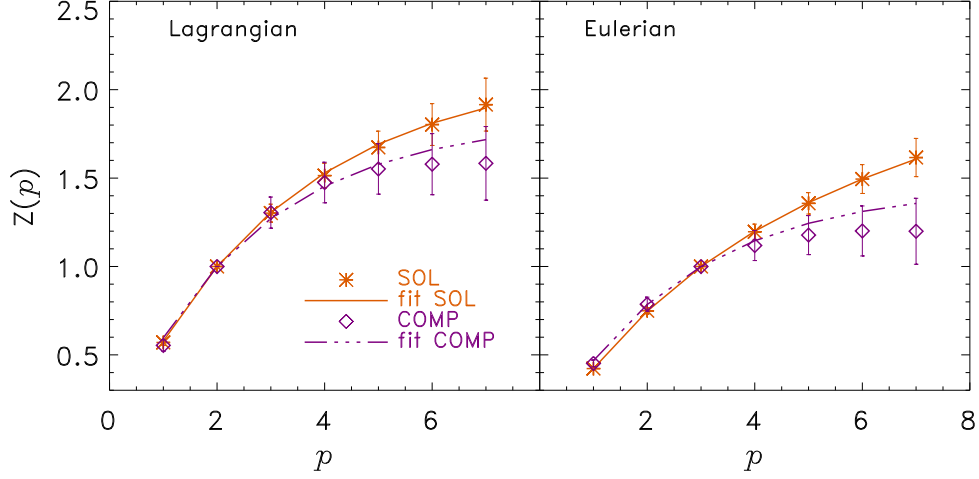
Figure 4.8: Relative scaling exponents for the Lagrangian (left panel) and Eulerian (right panel) structure function for solenoidal and compressive forcing. The lines indicate a fit with the intermittency model proposed by Dubrulle (1994) with the assumption of Schmidt et al. (2008), $\Delta = 1$. In the Lagrangian framework, we get a dimension of the most dissipative structures $D_{L,\mathrm{sol}} = 0.87$ and $D_{L,\mathrm{comp}} = 1.17$ for solenoidal and compressive forcing respectively. In the Eulerian framework we get $D_{E,\mathrm{sol}} = 1.11$ and $D_{E,\mathrm{comp}} = 1.55$. The compressive forcing and the associated stronger density fluctuations cause a higher dimension of the most dissipative structures.

structure function,

$$S^p(\alpha) = \int |\delta v|^p\, P(\delta v, \alpha) \mathrm{d}(\delta v)\,, \tag{4.16}$$

where $P(\delta v, \alpha)$ is the probability density of δv with the increment α. In the last Section, we showed that the PDFs of the velocity increments converge towards a Gaussian distribution on the largest scales. The Gaussian form can be understood analytically as a consequence of the central limit theorem, assuming that the two velocities, $v^m(\mathbf{r} + \ell)$ and $v^n(\mathbf{r})$ in space or $v^m(t + \tau)$ and $v^m(t)$ in time, are independent for large spatial or temporal increments. With the Gaussian assumption, we can express the structure functions on large scales as

$$
\begin{aligned}
S^p(\alpha \to \infty) \quad &= \quad \frac{2}{\sigma\sqrt{2\pi}} \int_0^\infty (\delta v)^p e^{-\frac{(\delta v)^2}{2\sigma^2}} \, \mathrm{d}\,(\delta v) \\
&= \quad \frac{\Gamma\left(\frac{p+1}{2}\right)}{\sqrt{\pi}} (\sqrt{2}\sigma)^p \,, \qquad (4.17)
\end{aligned}
$$

where $S^p(\alpha)$ stands for any structure function of (4.8) to (4.10), α is the temporal or spatial increment, σ is the standard deviation of the Gaussian distribution, and Γ is the Gamma function. Equation (4.17b) describes the moments of the Rayleigh distribution, which is also the result for the moments of the total structure function with a velocity increment $\delta\mathbf{v} = \sqrt{\delta v_x^2 + \delta v_y^2 + \delta v_z^2}$, if the increments δv_i follow a Gaussian distribution. Stutzki et al. (1998) showed that

$$
\langle(\delta v(\ell \to \infty))^2\rangle = 2\mathcal{M}_M^2 c_\mathrm{s}^2 \,, \qquad (4.18)
$$

where they used homogeneity and the fact that the autocorrelation vanishes for large spatial increments. In our case, the quantity $\mathcal{M}_M$ is a mass-weighted value, because the average in (4.18) is taken over the velocity increments of the tracer particles. Furthermore, we assume that the second-order structure function is proportional to the kinetic energy for large increments and as the longitudinal structure function and the structure function averaged over the three directions of the coordinate system have only one-third degree of freedom compared with the total structure function,

$$
\langle(\delta v)^2\rangle = \langle\delta v_x^2 + \delta v_y^2 + \delta v_z^2\rangle = 3\langle(\delta v_i)^2\rangle = 3\langle(\delta v_\parallel)^2\rangle\,. \qquad (4.19)
$$

If we combine this with (4.17) and (4.18), we get a relation between the standard deviations of the Gaussian distributions and the r.m.s Mach number $\mathcal{M}_M$:

$$
\langle(\delta v)^2\rangle = 2\mathcal{M}_M^2 c_\mathrm{s}^2 = 3\sigma_i^2 = 3\sigma_\parallel^2\,. \qquad (4.20)
$$

The second-order moment can thus be used as a normalisation for our formula (4.17) to predict the saturation level of the pth-order structure function

$$
S^p(\alpha \to \infty) = \frac{\Gamma\left(\frac{p+1}{2}\right)}{\sqrt{\pi}} (\frac{2}{\sqrt{3}}\mathcal{M}_M)^p\,. \qquad (4.21)
$$

Figure 4.9 shows the structure functions of Figure 4.6, but renormalised with equation (4.21) to the r.m.s. Mach number of the solenoidal forcing. The differences between the structure functions, driven by solenoidal and compressive forcing, vanishes in the integral range, what implies that the different
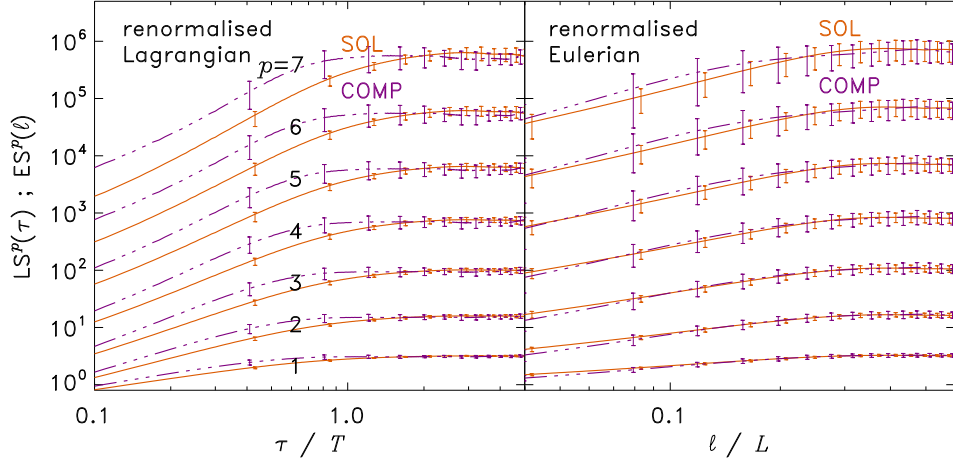
Figure 4.9: Same as Figure 4.6, but with structure functions of the compressive forcing normalised to the r.m.s. Mach number of the solenoidal forcing, using our model prediction (4.21). The differences of the structure functions between the solenoidal and compressive forcing thus vanish in the integral range.

forcings have no influence on the statistical properties of the structure functions in the integral range. Additionally, we verify this model by calculating the saturation behaviour with the measured r.m.s Mach number and compare the result with the saturation values extracted from Figure 4.6. The result is summarised in Figure 4.10. The measurements show an excellent agreement with the predicted values, for both solenoidal and compressive forcing.

4.9   Summary and conclusions

We have investigated the influence of solenoidal (divergence-free) and compressive (curl-free) forcing on the structure functions and density PDFs of a supersonic, compressible, turbulent flow using tracer particles in a set of three-dimensional numerical simulations. We analysed the density PDF, the PDFs of velocity increments, and the structure functions in the Lagrangian and Eulerian frameworks. As all of these quantities were measured on tracer particles, we analysed mass-weighted statistics. Our main results and conclusions are:

- The solenoidal forcing yields a density PDF close to a log-normal dis-
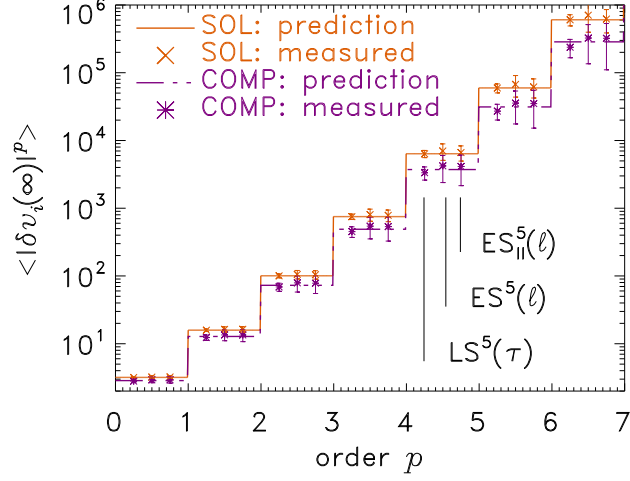
Figure 4.10: Values of the saturated structure functions measured from the simulation (crosses, stars, and error bars) and the values predicted from formula (4.21) (solid and dashed-dotted lines) for different orders p. The values are shown to the left of their respective order and the crosses and stars are from left to right the values of the Lagrangian, Eulerian, and the longitudinal Eulerian structure function. The error bars of the measured saturation values are the averaged errors of the structure functions.

tribution. In contrast, the compressive forcing yields distributions of the mass density that show stronger deviations from the log-normal shape in the wings of the distribution.

- The compressive forcing excites stronger head-on collisions and shock fronts, which show a correlation between high density and low velocity, affecting the mass-weighted r.m.s Mach number, such that it becomes smaller than the volume-weighted Mach number. Similar holds for the solenoidal forcing, but the effect is weaker, as solenoidal forcing yields smaller density contrasts at the same r.m.s. Mach number.

- The Lagrangian framework exhibits a more intermittent behaviour than the Eulerian one, measured with the deviations of the relative scaling exponents from the predicted intermittency-free K41 values and also with the kurtosis as an example for the higher moments of the PDF of the velocity increments. This analysis also shows that the turbulent medium, driven by the compressive forcing, is more intermittent than a

medium, driven by solenoidal forcing. A comparison with simulations of incompressible turbulence shows that intermittency is stronger in a supersonic, compressible medium.

- The influence of the different forcings are stronger in the Eulerian than in the Lagrangian framework, measured with the relative scaling exponents and the kurtosis of the velocity increments.

- The fractal dimension of the most dissipative structures are larger for compressive than for solenoidal forcing. The dimensions are around those of filamentary structures ($D = 1$) in the Lagrangian framework and between filamentary and sheet-like structures ($1 < D < 2$) in the Eulerian framework. Although the whole turbulent flow driven by the solenoidal forcing is more space filling the most dissipative structures of the compressive forcing are more space filling.

- The behaviour of the structure functions of all orders on the largest scales is determined by the r.m.s. Mach number of the system. With the assumption of a Gaussian distribution for the velocity increments on the largest scale, we derived an analytic relation, predicting the absolute values of the structure functions in the integral range of turbulence. The statistical properties of the velocity increments are indistinguishable in the integral range for both forcings types and follow our derived formula (4.21). The different values of the saturated structure functions observed in Figure 4.10 are caused by the different Mach numbers ($\mathcal{M}_{\mathrm{sol},M} = 4.9 \pm 0.2$ and $\mathcal{M}_{\mathrm{comp},M} = 4.4 \pm 0.3$), and not by different statistical properties obtained by the different forcings. Thus, the predictions based on equation (4.21) are independent of the energy injection mechanism of the turbulence, but only depend on the mass-weighted r.m.s. Mach-number.

4.10   Appendix I: Influence of the numerical grid resolution

Figure 4.11 (left panel) shows the LSF of order $p = 7$ for both forcing types and with the grid resolutions 256^3, 512^3, and 1024^3. The right panel shows the same for the ESF. The LSFs are calculated with $128^3 \approx 2.1$, $512^3 \approx 16.8$ and 5 million tracer particles for the different grid resolutions, respectively. The ESFs are calculated with 16^3 sub boxes and with 10^{10} sampling pairs. Figure 4.11 shows that the structure functions of order $p = 7$ differ by about 15%, caused by the different grid resolutions. This is of the same order as
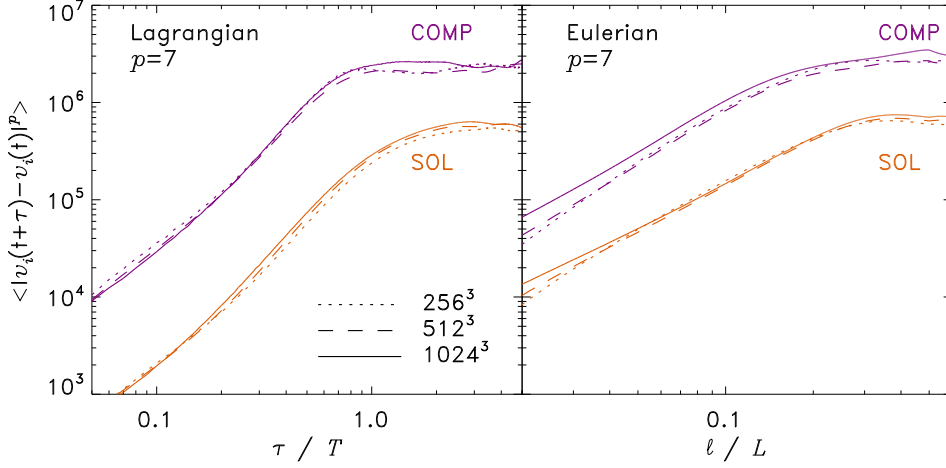
Figure 4.11: Structure functions of order $p = 7$ for different grid resolutions, shown for both forcing types. The LSF (left panel) with a low grid resolution of 256^3 and 512^3 were calculated with 128^3 and 256^3 tracer particles and the simulation with 1024^3 grid cells was calculated with 5×10^6 tracer particles. The ESF (right panel) was calculated with 16^3 sub boxes and 10^{10} sampling pairs. The structure functions of the compressive forcing was multiplied with a factor of 10 so that the structure functions are distinguishable.

the 1σ variations in time of the structure functions indicated as error bars in Figure 4.6. Therefore, the influence of the resolution is smaller than the temporal variations.

4.11 Appendix II: Convergence test for the structure functions

In order to verify that our calculations are converged with a sufficient number of data pairs to sample the structure functions, we show that the structure functions do not change significantly by further increasing the number of sampling pairs. As large velocity fluctuations have a stronger influence on the higher orders of the structure functions and these events are very rare, the statistical convergence of the higher orders is slower compared with the lower orders. Thus, if we can demonstrate convergence for the higher order structure functions, this automatically holds for all lower orders. Figure 4.12 (left panel) shows the Eulerian structure function of order $p = 7$ for solenoidal and compressive forcing. The structure function of the compressive forcing
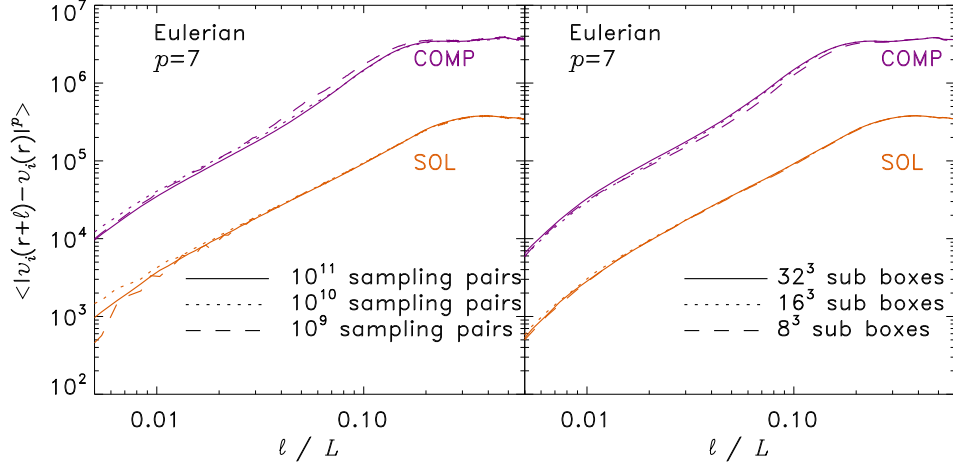
Figure 4.12: Left panel: ESF of order $p = 7$ for both forcing types, 16^3 sub boxes and different numbers of sampling pairs. The structure functions are converged on large scales for more than 10^{10} sampling pairs. Right panel: Same as left panel, however with 10^{11} sampling pairs and different numbers of sub boxes. In both Figures, the structure functions of the compressive forcing was multiplied by a factor of 10.

is multiplied by a factor of 10, so that the structure functions of the different forcings are distinguishable. In order to check the convergence, we use one random time sample ($t = 4T$) in the state of fully-developed turbulence, 16^3 sub boxes and different numbers of sampling pairs (10^9, 10^{10}, 10^{11}). Increasing the number of sampling pairs further only influences small scales, $\ell < 0.07\,L$. The structure functions are converged on larger scales. For the Eulerian structure function, we also verified that the method of selecting tracer particles for the calculation with our procedure of sub boxes has no significant influence on the results. Therefore, we calculated the structure function with 10^{11} sampling pairs and different numbers of sub boxes (8^3, 16^3 and 32^3). Figure 4.12 (right panel) shows that further increasing the number of sub boxes also only influences scales $\ell < 0.05\,L$, and with 16^3 sub boxes, the structure functions are converged.

For the Lagrangian structure function, we also have to verify that the structure functions do not change significantly with the number of sampling pairs. We calculate the LSF for all 512^3 tracer particles for one time-line from $t = 2T$ to $t = 10\,T$ and compare it with the LSF calculated with 5 and 10 million tracer particles. The results are shown in Figure 4.13, where the
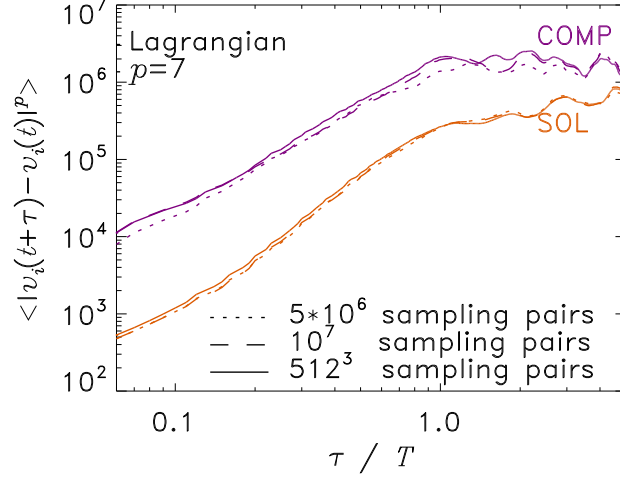
Figure 4.13: LSF of order $p = 7$ for both forcing types and 5, 10, and $512^3 \approx 134$ million sampling pairs. The structure functions calculated with solenoidal forcing are converged on all scales. The structure functions calculated with compressive forcing show a small influence of the number of used sampling pairs. The structure function of the compressive forcing was multiplied by a factor of 10.

structure functions with compressive forcing are multiplied with a factor of 10. The structure functions calculated for solenoidal forcing are converged on all scales, and the structure functions calculated for compressive forcing show only small variations with the number of sampling pairs. The reason for the large fluctuations in the integral range in Figure 4.13 is that the LSF was here calculated with one time-line only. Figure 4.13 shows that the time evolution of the forcing module has a direct influence on the amplitudes of the velocity increments in the integral range, but these fluctuations are smaller than the variations in time, we use as errors in Figure 4.6. However, this direct influence vanishes on average by using different staring times for calculating the LSF. In the inertial range with $\tau < 1\,T$, the structure functions in Figure 4.6 have a factor of about 700 more sampling pairs for each bin. This large statistic we used there ensures that our structure functions are also converged in the inertial range.

Chapter 5

A new density variance - Mach number relation for subsonic and supersonic, isothermal turbulence

The co-authors of this study are Philipp Girichidis, Christoph Federrath, and Ralf S. Klessen (Konstandin et al., 2012b). The simulations were provided by C. Federrath.

The probability density function (PDF) of the gas density in subsonic and supersonic, isothermal, driven turbulence is analysed with a systematic set of hydrodynamical grid simulations with resolutions up to 1024^3 cells. We performed a series of numerical experiments with root mean square (r.m.s.) Mach number $\mathcal{M}$ ranging from the nearly incompressible, subsonic ($\mathcal{M} = 0.1$) to the highly compressible, supersonic ($\mathcal{M} = 15$) regime. We study the influence of two extreme cases for the driving mechanism by applying a purely solenoidal (divergence-free) and a purely compressive (curl-free) forcing field to drive the turbulence. We find that our measurements fit the linear relation between the r.m.s. Mach number and the standard deviation of the density distribution in a wide range of Mach numbers, where the proportionality constant depends on the type of the forcing. In addition, we propose a new linear relation between the standard deviation of the density distribution σ_ρ and the standard deviation of the velocity in compressible modes, i.e. the compressible component of the r.m.s. Mach number $\mathcal{M}_{\mathrm{comp}}$. In this relation the influence of the forcing is significantly reduced, suggesting a linear relation between σ_ρ and $\mathcal{M}_{\mathrm{comp}}$, independent of the forcing, ranging from the subsonic to the supersonic regime.

5.1 Motivation

Understanding the intricate interplay between interstellar turbulence and self-gravity is one of the key problems in star formation theory. The supersonic turbulent velocity field is likely responsible for the complex and filamentary density structures observed in molecular clouds. It creates dense regions that can become gravitationally unstable and collapse into dense cores, and eventually turn into new stars (Elmegreen and Scalo, 2004; Mac Low and Klessen, 2004; McKee and Ostriker, 2007). Statistical quantities, describing this process, such as the initial mass function, the core mass function (Padoan and Nordlund, 2002; Hennebelle and Chabrier, 2008, 2009), and the star formation rate (Hennebelle and Chabrier, 2011; Padoan and Nordlund, 2011) depend on the standard deviation (std. dev.) of the density of the molecular cloud. The pioneering works by Padoan et al. (1997) and Passot and Vázquez-Semadeni (1998) have shown that the std. dev. σ_ρ of the probability density function(PDF) of the mass-density grows proportional to the root mean square (r.m.s.) Mach number $\mathcal{M}$ of the turbulent flow

$$\sigma_\rho / \langle \rho \rangle_V = b \, \mathcal{M} \,, \tag{5.1}$$

where $\langle \rho \rangle_V$ is the volume-weighted mean density and b is a proportionality constant. A solid understanding of the interplay between the highly turbulent velocity field and the resulting statistical properties of the density distribution is not just important for models of star formation theory, but also for other fields of astrophysics, such as the diffuse interstellar medium (e.g. Hill et al., 2008; Burkhart et al., 2010; Gaensler et al., 2011), galaxy evolution (e.g. Bigiel et al., 2008), or galactic and protogalatic dynamos (e.g. Beck, 1996; Schober et al., 2012). Federrath et al. (2008, 2010) explained the dependence of σ_ρ on b by taking the modes of the forcing into account that drive the turbulent velocity field. This model predicts for purely solenoidal forcing $b = 1/3$ and for purely compressive forcing $b = 1$, and explains the large deviations of b ranging from $b = 0.26$ to $b = 1.05$ in previous works (e.g. Padoan et al., 1997; Passot and Vázquez-Semadeni, 1998; Li et al., 2003; Kritsuk et al., 2007; Beetz et al., 2008; Schmidt et al., 2009; Price et al., 2011; Burkhart and Lazarian, 2012; Konstandin et al., 2012a; Molina et al., 2012). We follow up on this work and discuss the physical origin of this dependency and introduce a new relation, similar to equation (5.1), however, correlating the compressible component of the r.m.s Mach number $\mathcal{M}_{\mathrm{comp}}$ with σ_ρ.
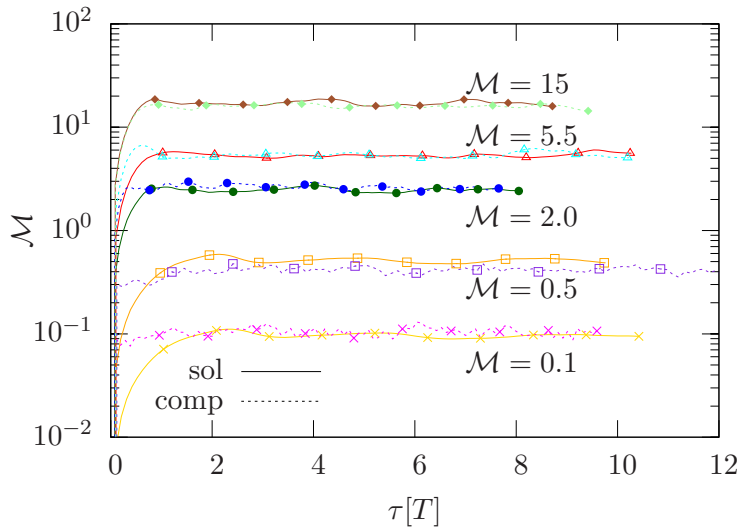
Figure 5.1: R.m.s. Mach number of all simulations as a function of the dynamical time scale, calculated by averaging over all grid cells for both types of forcing.

5.2 State of fully developed turbulence

Figure 5.1 shows the time evolution of the r.m.s. Mach numbers $\mathcal{M}$ in all simulations. The fluid reaches the equilibrium state of fully developed turbulence after about two turbulent crossing times $t \approx 2T$. We thus average all the following analyses for $2 \leq t/T$.

5.3 Volume- and mass-weighted probability density functions

It is well-known that the PDF of the logarithm of the mass density $p(s)$ in a turbulent, isothermal medium is close to a Gaussian distribution (see e.g. Vazquez-Semadeni, 1994; Passot et al., 1994; Padoan et al., 1997; Klessen, 2000; Kritsuk et al., 2007; Federrath et al., 2008; Konstandin et al., 2012a)

$$p(s) = \frac{1}{\sqrt{2\pi}\sigma_s} \exp\left(\frac{-(s - \langle s \rangle)^2}{2\sigma_s^2}\right). \tag{5.2}$$

Li et al. (2003) showed with the assumption of a Gaussian, volume-weighted PDF of s that the mass-weighted PDF of s is also Gaussian with the same std. dev. and with a shifted mean value

$$\langle s \rangle_V = -\langle s \rangle_M = -\frac{\sigma_s^2}{2}. \tag{5.3}$$

Figure 5.2 (left) shows the volume- and mass-weighted PDFs (the volume-
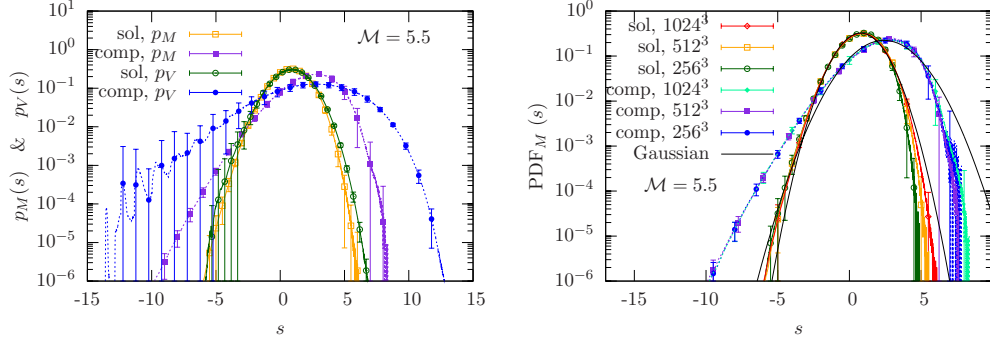
Figure 5.2: Left: Mass-weighted and volume-weighted PDFs of the logarithm of the mass density in the simulations with $\mathcal{M} = 5.5$, 1024^3 grid cells and both types of forcing. Right: Mass-weighted PDFs of s of the simulations for $\mathcal{M} = 5.5$, different resolutions and both types of forcing. The black solid lines are Gaussian functions with mean value and std. dev. calculated with the highest resolution.

weighted PDF is shifted with $\langle s \rangle_M - \langle s \rangle_V = \sigma_s^2$ for a better comparison) for the simulation with $\mathcal{M} = 5.5$ for both types of forcing. The PDFs are averaged over 81 time snapshots in the state of fully developed stationary turbulence for $t \geqslant 2T$ and the error bars indicate the std. dev. of the temporal fluctuations. The variance of the volume-weighted PDFs is larger than the variance of the mass-weighted distributions. This effect is stronger for the compressive forcing than for the solenoidal forcing. The volume-weighted PDFs show a larger variation with time in the low-density wing of the distribution than the mass-weighted distributions. This low-density wing also shows higher probabilities than one would expect from the underlying Gaussian distribution extrapolated from the high density wing. This effect is stronger for the compressive than for the solenoidal forcing. We assume that this behaviour is caused by our forcing scheme. As the time correlation of the forcing field is equal to the dynamic time scale on the largest scales, the forcing has enough time to produce very low densities in large regions of diverging flows. This process causes the volume-weighted PDF of s to have a tail at low densities with higher probabilities than the distribution for the case of turbulence, which is not driven on the largest scales. As this effect is proportional to the amplitude of the forcing field, which increases stronger than the r.m.s. Mach number in the statistically state of fully developed turbulence, it becomes more important for higher r.m.s. Mach numbers and the deviations in the low-density tail influence the calculated std. dev. of these distributions. This effect is less pronounced measuring the mass-weighted distributions, as

the very low density grid cells carry only little mass. We note that there are other potential processes, which could lead to non-Gaussian wings in the PDF, such as turbulent intermittency or self-gravity (e.g. Klessen, 2000; Kritsuk et al., 2007; Burkhart et al., 2009; Federrath et al., 2010).

5.4 Resolution effects on the probability density functions

Figure 5.2 (right) shows the mass-weighted PDF of the quantity s with an r.m.s. Mach number $\mathcal{M} = 5.5$ and different resolutions. The PDF of s shows deviations from the Gaussian shape and a dependency on the resolution only in the high-density tails of the distribution. We interpret the deviations of our measured PDFs from the Gaussian distribution in the supersonic regime for both types of forcing as a sign of numerical dissipation and finite sampling. In the highly supersonic regime the medium is dominated by shock fronts, high-density gradients and strong intermittent fluctuations, which are building up in the high-density tail and require high resolution to converge. As the high-density tail is always truncated due to limited numerical resolution (see Hennebelle and Audit, 2007; Kowal et al., 2007; Kitsionas et al., 2009; Price and Federrath, 2010; Federrath et al., 2010) we do not fully resolve them in the $\mathcal{M} = 5.5$ case and an additional dissipation occurs. This effect is stronger in the simulations with compressive forcing and becomes stronger with increasing r.m.s. Mach number for both types of forcing (not shown here). However, increasing the resolution has only little influence on the deviations from the Gaussian distribution in the low-density tail of the mass-weighted PDFs.

With the assumption of a log-normally distributed mass density, it can be shown that the std. dev. of the Gaussian-distributed quantity s is (see Price et al., 2011)

$$\sigma_s^2 = \ln\left(1 + \sigma_\rho^2\right). \tag{5.4}$$

Figure 5.3 shows σ_ρ as a function of σ_s for our volume-weighted (left panel) and mass-weighted (right panel) distributions. The volume- and the mass-weighted measurements of the std. dev. of s show increasing deviations from equation (5.4) with increasing r.m.s. Mach numbers for both types of forcing. However, the deviations are smaller in the mass-weighted case than in the volume-weighted one. The assumption of Gaussianity, which is implied in equation (5.4), is better fulfilled for the mass-weighted case. Figure 5.3 also shows that our measurements with $\mathcal{M} = 15$ are not converged with resolution
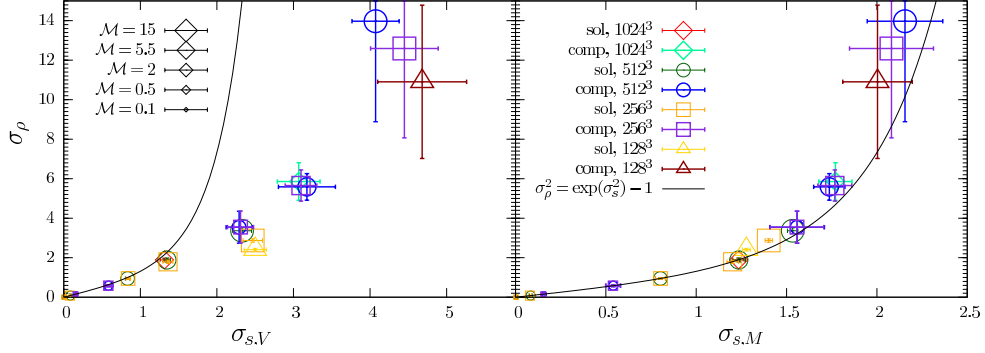
Figure 5.3: Std. dev. of the mass-density σ_ρ as a function of the std. dev. of the logarithm of the mass-density σ_s, measured volume-weighted (left panel) and mass-weighted (right panel). The deviations of the measurements from the black solid lines, equation (5.4), quantify the deviations from a log-normally distributed mass density.

for both types of forcing. Our measurements are in agreement with Price et al. (2011), who showed that direct measurements of σ_ρ show a stronger dependency on resolution than measurements of σ_s.

All volume-weighted measurements show a clear trend towards the relation (5.4) with increasing resolution. However, the data points do not fit relation (5.4) for $\mathcal{M} = 15$ with solenoidal forcing and in all the supersonic cases with compressive forcing, although the data points with $\mathcal{M} = 2$ and $\mathcal{M} = 5.5$ with compressive forcing are nearly converged with resolution. Considering that the std. dev. $\sigma_{s,M}$ of the mass-weighted PDF is more compatible with the scaling for a log-normal PDF, equation (5.4), and that the resolution dependence of $\sigma_{s,M}$ is weaker that for $\sigma_{s,V}$, we prefer to use $\sigma_{s,M}$ as estimate for the turbulent density fluctuations in the following.

5.5 The probability density function of the density and of the compressible modes in the velocity field

Figure 5.4 shows the mass-weighted PDFs of the quantity s (left panels) and the volume-weighted PDFs of the compressible modes of the velocity field normalised to the sound speed $M_{\mathrm{comp}} = v_{\mathrm{comp}}/c_s$ (right panels) for different r.m.s. Mach numbers and both types of forcing. The PDFs of the
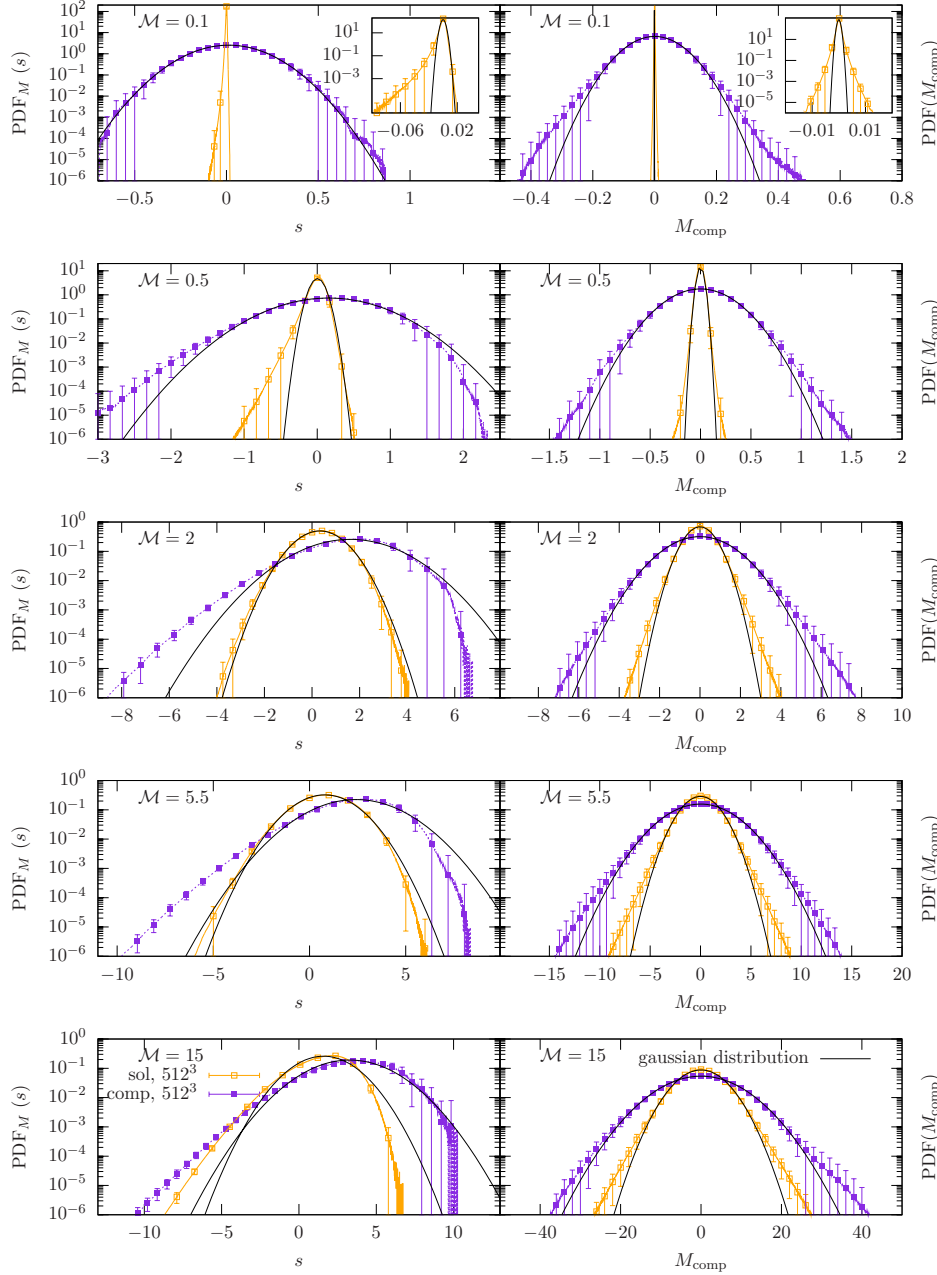
Figure 5.4: The mass-weighted PDFs of the logarithm of the mass density (left panels) and the compressible part of the local Mach number (right panels) for different r.m.s. Mach numbers, resolutions and both types of forcing. In the inset, a magnification of the PDFs obtained with solenoidal forcing for $\mathcal{M} = 0.1$ are shown. The error bars in each panel indicate the std. dev. of the temporal fluctuations.

logarithm of the density largely follow Gaussian distributions for all super-
sonic r.m.s. Mach numbers. We added Gaussian functions (black solid lines),
with the first- and second-order moments calculated from our distributions in
Figure 5.4. The high-density tails of the distributions show deviations from
the Gaussian shape, which increase with increasing r.m.s. Mach number.
Also the deviations from the Gaussian distribution in the low-density tail, as
discussed in Section 5.3, get more pronounced with increasing r.m.s. Mach
number. Thereby, we have large deviations of our measurement from the
Gaussian distributions in the $\mathcal{M} = 15$ case and the calculated std. dev. does
not correspond to the std. dev. of the underlying Gaussian distribution.

The density distributions of the simulations driven by solenoidal forcing in
the subsonic regime show significant deviations from the log-normal shape,
which become stronger as $\mathcal{M}$ decreases. These distributions become more
asymmetric and more peaked. The different behaviour of the PDFs in the
subsonic regime especially for the solenoidal forcing is caused by the different
physical processes acting here. In the subsonic regime sound waves trans-
fer information faster than the averaged flow of the medium, such that the
thermal pressure increases before two converging flows can collide. This pro-
cess prevents colliding flows from producing high-density regions and causes
the sharp edge at the high-density wing of the distributions. The thermal
pressure also decelerates the velocities in compressible modes, such that the
PDF of M_{comp} also shows a narrow, peaky and intermittent behaviour for the
solenoidal forcing. This process is just visible for solenoidal forcing, because
in the compressive forcing case the velocities in compressible modes are re-
injected by the forcing to hold the r.m.s. Mach number constant. This is the
reason why the thermal pressure does not have such a strong influence there.
The right panels of Figure 5.4 show the PDFs of M_{comp}, where M_{comp} is
calculated by transforming the velocity field into Fourier space and apply-
ing the same projection tensor we use for the forcing field, $P_{ij}^{\parallel} = k_i k_j / k^2$.
After transforming it back into real space, we calculate the std. dev. of the
components, which we average afterwards over the three directions of the co-
ordinate system x, y, z. The distributions of M_{comp} are symmetric with zero
mean and have an increasing std. dev. with increasing r.m.s. Mach number.
The distributions obtained with compressive forcing are always broader than
with solenoidal forcing at the same r.m.s. Mach number. The PDFs of M_{comp}
are Gaussian (black solid lines) with deviations in both wings. These are the
signpost of turbulent intermittency. The deviations do not show a clear trend
with the r.m.s. Mach number.

The PDF of M_{comp} obtained with solenoidal forcing in the subsonic regime
with $\mathcal{M} = 0.1$ shows the strongest deviations from the Gaussian shape with
a narrow, peaky, intermittent distribution. These deviations are caused by

the thermal pressure, as discussed above.

5.6 Relation between the r.m.s. Mach number and the standard deviation of the density

In Padoan et al. (1997) and Passot and Vázquez-Semadeni (1998) the authors found that the std. dev. of the PDF of the mass density σ_ρ is proportional to the r.m.s. Mach number in a turbulent flow. The std. dev. of the mass density is an important quantity especially in astrophysics, where the Mach number dependency of density fluctuations is used to derive analytic expressions for the core mass function (CMF) and the stellar initial mass function (IMF) (e.g., Padoan and Nordlund, 2002; Hennebelle and Chabrier, 2008, 2009). On galactic scales it is used to reproduce the Kennicutt-Schmidt relation (Tassis, 2007), and Elmegreen (2008) suggests that the star formation efficiency is a function of the density PDF. Figure 5.5 (upper left panel) shows the measured std. dev. of the mass density as a function of the r.m.s. Mach number for different resolutions and both types of forcing. The error bars in each panel of Figure 5.5 indicate the std. dev. of the temporal fluctuations of the measured quantities. They do not include any potential systematic errors stemming from, e.g., the numerical scheme or implementation of the forcing algorithm. Thus, we interpret the error bars as a lower limit of the real uncertainty. The dotted and dashed-dotted lines correspond to the model of Federrath et al. (2010), which describes the proportionality parameter b as a function of the turbulent forcing. This model predicts for solenoidal forcing $b = 1/3$ and for compressive forcing $b = 1$. Our measurements agree with the model of Federrath et al. (2010) in the supersonic case for both types of forcing. We see small deviations from the model in the simulations with $\mathcal{M} = 15$, which is caused by our limited resolution (see Figure 5.3). The std. dev.s of the density distribution of the simulation with solenoidal forcing are smaller than the prediction of the model in the subsonic case. In the subsonic regime, the deviations are caused by the thermal pressure, which damps density variations and compressible modes of the velocity field and reduces the measured std. dev. below the model prediction as discussed in Section 5.5. The upper right panel of Figure 5.5 shows the mass-weighted, logarithmic std. dev. $\sigma_{s,M}$ as a function of the r.m.s. Mach number. The dotted and dashed-dotted lines correspond to the standard model for the
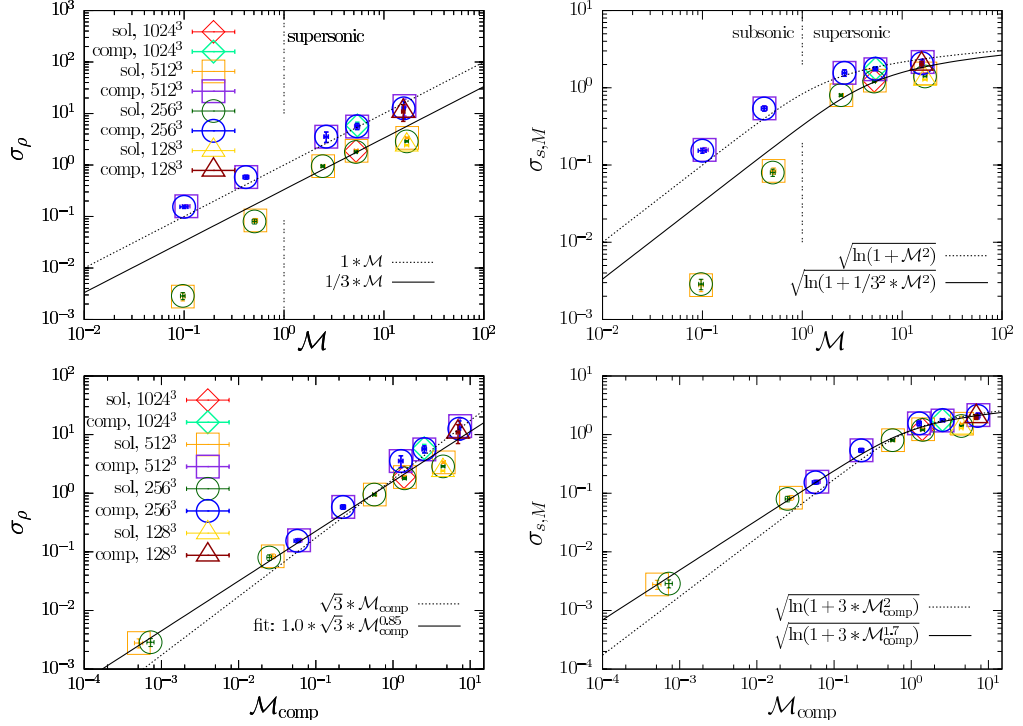
Figure 5.5: The std. dev. of the distribution of the mass density (left) and the std. dev. of the distribution of the logarithm of the mass density (right) as a function of the r.m.s. Mach number (upper panels) and as a function of the compressible part of the r.m.s. Mach number (lower panels). In the upper panels the lines correspond to the model of Federrath et al. (2010) with $b = 1/3$ for solenoidal forcing and $b = 1$ for compressive forcing. In the lower panels the solid lines correspond to a two-parameter fit and the dotted line corresponds to a linear relation between the std. dev. of the mass density and the std. dev. of the compressible part of the r.m.s. Mach number with a proportionality constant $\sqrt{3}$.

logarithmic density variance,

$$\sigma_s^2 = \ln(1 + b^2 \mathcal{M}^2) \tag{5.5}$$

with $b = 1/3$ for solenoidal and $b = 1$ for compressive forcing. Equation (5.5) follows from equations (5.4) and (5.1) and was recently derived analytically by Molina et al. (2012) using the shock-jump conditions and averaging over an ensemble of shock waves. The deviations of our numerical data from this standard model are only significant for solenoidal forcing in the subsonic regime, while our data are in excellent agreement with equation (5.5) for both solenoidal and compressive forcing in the supersonic regime, given our resolution dependence of the $\mathcal{M} = 15$ data points (see Figure 5.3, right panel). Our results are in agreement with Kowal et al. (2007), who found deviations from the linear relation with σ_ρ in the subsonic regime with solenoidal forcing, and with Passot and Vázquez-Semadeni (1998), who analysed one-dimensional simulations with only compressive forcing and $0.5 \leq \mathcal{M} \leq 3$ and found the linear relation between $\mathcal{M}$ and σ_ρ with $b = 1$. Price et al. (2011) analysed three dimensional simulations with purely solenoidal forcing and r.m.s. Mach numbers in between $2 \leq \mathcal{M} \leq 20$ and found $b = 1/3$ in excellent agreement with our result. As they did not analyse the subsonic regime with solenoidal forcing they did not observe the large deviations in the subsonic regime. Our analysis complements these studies with measurements in both the subsonic and supersonic regime and for purely compressive forcing.

5.7 Physical origin of density fluctuations in turbulent flows

Studying the continuity equation (3.1), one can argue that variations of the density can only be caused by the divergence of the velocity field. Given that a vector field can be decomposed in a gradient field and a rotation field and that the divergence of a rotation field vanishes, we conclude that the density variations can only be caused by the compressible modes of the velocity. A similar model has also been suggested by Federrath et al. (2010), where the parameter b in equations (5.1) and (5.5) was approximated by the ratio of compressible to total velocity fluctuations. As we want to understand the physical origin of the density fluctuations, we replace the r.m.s. Mach number and the b-parameter with the compressible part of the r.m.s. Mach number, $\mathcal{M}_{comp}$, in equation (5.1), where $\mathcal{M}$ is in fact the std. dev. of the velocity distribution, and b is proportional to the ratio of compressible to total velocity fluctuations and depends on the forcing. The lower panels of

Figure 5.5 show the density fluctuations as a function of $\mathcal{M}_{\text{comp}}$. The data points show a clear correlation. The different behaviour of the simulations driven with solenoidal and compressive forcing are significantly reduced. We added in Figure 5.5 a function (dotted line) for the relation $\sigma_\rho = \sqrt{3}\mathcal{M}_{\text{comp}}$, which is the simplest model for this relation assuming isotropy. The factor of $\sqrt{3}$ is due to the fact that we use the distribution of the compressible modes of the velocity field averaged over the three directions of the coordinate system

$$\mathcal{M}_{\text{comp}}^{\text{tot}} = \sqrt{\mathcal{M}_{\text{comp},x}^2 + \mathcal{M}_{\text{comp},y}^2 + \mathcal{M}_{\text{comp},z}^2} \tag{5.6}$$
$$= \sqrt{3}\mathcal{M}_{\text{comp}} \,.$$

Our simple model fits the data, but shows deviations for the simulations with solenoidal forcing and the lowest and highest Mach numbers. The deviations for the $\mathcal{M} = 15$ simulation are again caused by the resolution dependency of σ_ρ. Additionally, we perform a fit of our data (black solid line) with two free parameters,

$$\sigma_\rho = \alpha\sqrt{3}\mathcal{M}_{\text{comp}}^\beta \tag{5.7}$$

for the density relation. We obtain a normalisation $\alpha = 1.0 \pm 0.1$ and a slope $\beta = 0.85 \pm 0.04$. For the s-relation we transform the fitted function with equation (5.4). The measurements of the std. dev. of the density have larger deviations from the model as the measurements of the std. dev. of s. However, the model fits the measurements in both cases and provides a good description for the data points in the subsonic regime with solenoidal forcing, which are strongly influenced by sound waves. We conclude that the thermal pressure damps the velocities in compressible modes in a way that the relation between the velocities in compressible modes and the density variations in a turbulent medium is in a statistical equilibrium state, even if the medium is strongly influenced by sound waves. The deviation of the scaling exponent from the simple model can be interpreted as additional dissipative effects, which are proportional to $\mathcal{M}_{\text{comp}}$. An example for these physical processes, which influence our analysis, are individual shocks causing deviations from the log-normal distributed density PDF. However, systematic errors with a dependency on the r.m.s. Mach number could also cause deviations from the linear scaling and would be another possible interpretation for our fitted scaling exponent.

The shown relation between the std. dev. of the density and the compressible part of the r.m.s. Mach number in principle enables us to measure the kinetic energy in compressible modes in giant molecular clouds, without knowing the absolute r.m.s. Mach number, the driving mechanism or the sound speed. The relations shown in the bottom panels of Figure 5.5 are valid in both, the subsonic and supersonic regime.

5.8 Summary and conclusions

We have investigated the influence of solenoidal (divergence-free) and compressive (curl-free) forcing on the PDF of the mass density in subsonic and supersonic turbulence with a set of three-dimensional numerical simulations. We analysed the relation between the std. dev. of the mass density distribution and the r.m.s. Mach number. We found a new relation between the std. dev. of the mass density and the std. dev. of the compressible part of the velocity field, $\sigma_\rho \propto \mathcal{M}_{comp}$. Our main results are as follows:

- Compressive forcing yields mass density PDFs with std. dev.s proportional to the r.m.s. Mach number with $b = 1$. For solenoidal forcing, we measure $b = 1/3$ in the supersonic regime. Our findings are in agreement with previous studies, which however only explored different subsets of the full parameter space investigated here. We also found deviations of our measurements from the linear relation with solenoidal forcing in the subsonic regime. These deviations from the linear relation can be explained with sound waves, which damp the faint compressible velocities and prevent the medium from producing over-densities.

- We found a unique relation between the std. dev. of the mass density and the compressible modes of the velocity field with a fit to our data. Our new relation is independent of the driving mechanism and still holds in the subsonic regime, where the flow is mainly influenced by sound waves. It does not show a strong influence on the resolution and other effects, which may cause a non-Gaussian distribution of the density.

- Our relation enables us for the first time to measure the kinetic energy in compressible modes in units of the sound speed, without knowing the r.m.s. Mach number, the driving mechanism or the sound speed of the medium. This measurement can be used to distinguish between subsonic and supersonic compressive turbulent motions. It will in principle allow us to measure the composition of the kinetic energy in the interstellar medium by combining independent measurements of the total r.m.s. Mach number (e.g. Burkhart et al., 2009) and the std. dev. of the density distribution (Brunt et al., 2010; Brunt, 2010; Schneider et al., 2012).

Chapter 6

Hierarchical Bayesian analysis of the velocity power-spectrum in supersonic turbulence

The co-authors of this study are Rahul Shetty, Philipp Girichidis, and Ralf S. Klessen (Konstandin et al., 2014). The forcing routine was implemented by Philipp Girichidis.

Turbulence is a dominant feature operating in gaseous flows across nearly all scales in astrophysical environments. Accordingly, accurately estimating the statistical properties of such flows is necessary for developing a comprehensive understanding of turbulence. We develop and employ a hierarchical Bayesian fitting method to estimate the parameters describing the scaling relationships of the velocity power spectra of supersonic turbulence. We demonstrate the accuracy and other advantages of this technique compared with ordinary linear regression methods. Using synthetic power spectra, we show that the Bayesian method provides accurate parameter and error estimates. Commonly used normal linear regression methods can provide estimates that fail to recover the underlying slopes, up to 70% of the instances, even when considering the 2σ uncertainties. Additionally, we apply the Bayesian methods to analyse the statistical properties of compressible turbulence in three-dimensional numerical simulations. We model driven, isothermal, turbulence with root mean square Mach numbers in the highly supersonic regime $\mathcal{M} \approx 15$. We study the influence of purely solenoidal (divergence-free) and purely compressive (curl-free) forcing on the scaling exponent of the power spectrum. In simulations with solenoidal forcing and 1024^3 resolution, our results indicate that there is no extended inertial range with a constant scaling exponent. The bottleneck effect results in a curved

power spectrum at all wave numbers and is more pronounced in the transversal modes compared with the longitudinal modes. Therefore, this effect is stronger in stationary turbulent flows driven by solenoidal forcing compared to the compressive one. The longitudinal spectrum driven with compressive forcing is the only spectrum with constant scaling exponent $\zeta = -1.94 \pm 0.01$, corresponding to slightly shallower slopes than the Burger's prediction.

6.1 Motivation

Turbulence is a critical component of gaseous flows on nearly all scales, as it is intimately related to many physical properties of the medium, such as the morphology, mixing characteristics, and thermal structure. Turbulence is known to play a strong if not dominant role in a variety of systems, from terrestrial incompressible flows (e.g. combustion engines, aerodynamics) to highly supersonic compressible flows often occurring in astrophysical environments. Consequently, accurately characterising the statistical properties of turbulence is necessary for developing a comprehensive understanding of fluid dynamics across a wide range of different environments.

The statistical properties of turbulence, such as the power spectrum, may serve as diagnostics for distinguishing between different models. In the astrophysical context, for instance, these are analytical and numerical models describing accretion disks in protoplanetary systems (see e.g. Meschiari, 2012), the dynamics of the interstellar medium relevant for star formation (see e.g. Mac Low and Klessen, 2004; McKee and Ostriker, 2007), the formation of star clusters and galaxies (Hopkins, 2012) and galaxy evolution (Iannuzzi and Dolag, 2012). Turbulence theory is also important in the description of the diffuse interstellar medium (Elmegreen and Scalo, 2004) and for galactic or protogalactic dynamos (Brandenburg and Subramanian, 2005; Schober et al., 2012). Despite the impact of compressible turbulence across a range of disciplines a comprehensive theoretical understanding remains elusive.

One key assumption of the Kolmogorov (1941b) theory describing incompressible turbulence is that the energy transfer rate from large to small spatial scales ϵ should be constant. With the definition of a velocity fluctuation δu_ℓ at a length scale ℓ and its dynamical time-scale $\tau_\ell = \ell/\delta u_\ell$ one obtains

$$\epsilon \simeq \frac{\delta u_\ell^2}{\tau_\ell} \Leftrightarrow \delta u_\ell \simeq (\epsilon \ell)^{1/3}. \qquad (6.1)$$

This indicates that the velocity fluctuations can be described by a scaling law in the so called *inertial range*, where the energy transfer rate ϵ is constant and the flow is not influenced by viscous damping or the energy injection

mechanism. From the power law behaviour of the velocity fluctuations a scaling law of the Kolmogorov velocity power spectrum $P(k)$ can be derived,

$$P(k) \propto \epsilon^{2/3} k^{-5/3} . \tag{6.2}$$

The kinetic energy is injected on the large scales and cascades to small scales through non-linear coupling, until viscous effects become important with respect to the advective terms. At this "dissipation scale" viscous effects cannot be neglected any more and the kinetic energy is converted into heat (i.e. internal energy). This description has to be extended for compressible turbulence. In the incompressible case, scale locality is crucial for the Richardson-Kolmogorov picture of a cascade with constant energy flux through the scales (Frisch, 1995). The non-local, inter-scale processes of compressible turbulence via shock fronts have to be taken into account. Additionally, the complex interplay between a varying density/pressure distribution with the velocity field may be a dominant processes in a supersonic, compressible flow. Therefore, accurately measuring the scaling exponent of the power spectrum is necessary for gaining a comprehensive understanding of compressible turbulence (e.g. Kaneda et al., 2003; Kritsuk et al., 2007; Lemaster and Stone, 2009; Federrath et al., 2010).

The theoretical predictions for the scaling exponents span only a small range from $-5/3$ in the incompressible Kolmogorov (1941b) case, over -2 in the shock dominated Burgers (1948) case and up to $-19/9$ in the more recent theory of compressible turbulence of Galtier and Banerjee (2011) for the $\rho^{1/3} v$ spectrum. Therefore, a high precision measurement, as well as exact error estimates are needed to distinguish between these model predictions.

Numerical simulations provide a viable avenue for measuring the statistical properties of turbulent flows, and, by extension, testing theoretical descriptions. It is common practise to employ normal χ^2-based regression methods to estimate the scaling exponent of the power spectrum of numerical simulations. Systematic errors, such as the influence of the chosen fitting range, are normally not explicitly treated. In this paper, we explore how common fitting methods, and the associated assumptions, affect the resulting parameter estimates. We develop and compare a hierarchical Bayesian technique with ordinary fitting methods, with the goal of quantifying how well the power spectrum in numerical simulations follow an exact power law. We focus here on the description of the methods and a comparison with other methods.

Bayesian inference has the advantage that uncertainties in the data are rigorously and self-consistently treated (e.g. Kelly, 2007; Gelman et al., 2004). Additionally, Bayesian methods are well suited for hierarchical problems,

where different datasets, such as individual snapshots, can be analysed simultaneously, providing parameter estimates of both the individuals as well as for the whole population. In astrophysics, Bayesian methods have been developed for analysing observational data, such as turbulence in the ISM (Shetty et al., 2012), analysis of dust extinction (Foster et al., 2013) and spectral energy distributions (Kelly et al., 2012). Here, we apply a general hierarchical model for the statistical analyses of turbulence in numerical simulations. We demonstrate that the Bayesian method has important advantages, including accurate parameter estimation, over traditional non-hierarchical χ^2-based methods.

6.2   Caveats of the ordinary fitting methods

In practice, when analysing numerical simulations the scaling exponent is often measured by linear regression in a log-log plot of the time-averaged power spectrum, or on a $k^{5/3}$ or k^2 compensated spectrum (e.g. Kaneda et al., 2003; Kritsuk et al., 2007; Lemaster and Stone, 2009; Federrath et al., 2010). We describe in the following four common assumptions/methods that lead either to inaccurate scaling parameter estimates, or to complications in interpreting the results.

First, in a doubly logarithmic plot it is often difficult to verify if the best-fit regression line accurately reproduces the data. Many functions may appear to follow a power law in a doubly logarithmic plot. For example, if the scaling exponent varies slightly with k, a simple linear regression in log-space often does not reveal such fluctuations. To demonstrate this caveat we perform three fits in slightly varying ranges on the simulation with solenoidal forcing and 1024^3 grid cells (Figure 6.1). The resulting fitting parameters are listed in the Figure. All fits indicate a power law behaviour over a range $\Delta k \approx 10$, although the measured slopes change significantly. The reason for this is the curved behaviour of the power spectrum, which does not follow a power law over an extended range, as we will further discuss in Section 6.5. Hence, a qualitative validation whether the fit can reproduce the measured data is needed.

Second, the k extent of the inertial range is not known a priori. The above example demonstrates the influence of the chosen fitting range. It shows that the estimated slopes strongly depend on the extent in k, because the power-spectrum slope of the data is not necessarily constant in k. Depending on the data, the measured error of an ordinary linear regression method is very small and does not describe the intrinsic uncertainty of the data (see error estimate in Figure 6.1 and also Section 6.4), so that this cannot be used
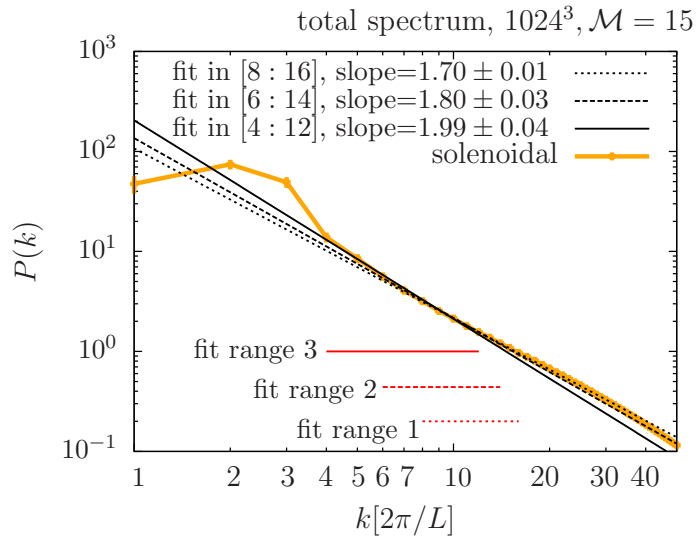
Figure 6.1: Time-averaged power spectrum of the simulation with 1024^3 grid cells and solenoidal forcing (orange points and error bars) and three different fits (black solid, dashed and dotted lines). The error bars correspond to the 1σ time variation of the power spectrum. All fits seem to describe the behaviour of the data in different k ranges.

to verify the quality of the chosen fitting range. In this case, an unbiased estimate of the inertial range is very difficult to obtain.

Third, a key assumption in a χ^2 linear regression is that the uncertainties are independently and normally distributed. The common practice of fitting in log space implicitly assumes that the uncertainties are normally distributed in log space. Usually the power spectra are averaged to minimise their time-dependence and to reduce the uncertainties and the scatter. However, averaging data also assumes that the uncertainties of the data are Gaussian or at least symmetrically distributed. Hence, both methods are based on the assumption of a Gaussian/symmetric scatter, but for the linear space as well as for the log space. Therefore, performing the averaging in linear space and the χ^2 fitting in log space is not consistent and violates this underlying assumption.

Finally, information such as the time variation and the intrinsic scatter contained in the data may be neglected when averaging data. Hierarchical models exploit all the information in the data, simultaneously estimating model parameters on multiple levels. In the next Section we introduce a hierarchical Bayesian method to account for these issues for analysing the

turbulent power spectra of numerical simulations.

6.3   Hierarchical Bayesian inference

To address the issues described above, we develop a hierarchical Bayesian fitting method. Hierarchical[1] modelling provides significant advantages when the dataset is naturally structured into two or more groups. For instance, the hydrodynamic simulations provide spatial information of all relevant quantities, such as the fluid densities and velocities, at a series of snapshots in time. The data is therefore structured into temporal groups. We can assess the variation in the spectrum by analysing the datasets on the individual time-level, as well as estimate the parameters of the mean spectrum. Bayesian methods are well suited for estimating model parameters on multiple levels in a hierarchical model.

With Bayes' theorem the probability $\mathcal{P}$ of a set of parameters $\boldsymbol{\theta}$ given the observed data $\mathbf{D}$ can be calculated

$$\mathcal{P}(\boldsymbol{\theta}|\mathbf{D}) \propto \mathcal{P}(\mathbf{D}|\boldsymbol{\theta})\mathcal{P}(\boldsymbol{\theta})\,, \tag{6.3}$$

where $\mathcal{P}(\mathbf{D}|\boldsymbol{\theta})$ is the probability of the set of data $\mathbf{D}$ given the set of parameters $\boldsymbol{\theta}$, known as the likelihood function $\mathcal{L}(\mathbf{D}|\boldsymbol{\theta})$. $\mathcal{P}(\boldsymbol{\theta})$ is referred to as the prior and is the probability of the set of parameters. We will define $\boldsymbol{\theta}$ in detail below. The outcome of Bayesian inference is the probability of the model parameters $\boldsymbol{\theta}$ given the data $\mathbf{D}$ and is called posterior distribution. To evaluate the posterior, we perform a Markov Chain Monte Carlo (MCMC) sampling of $\boldsymbol{\theta}$ for constructing the product of the prior and likelihood. The result of the Bayesian inference, the posterior, is the joint probability distribution of the parameters. The errors in each measured quantity are assumed to be drawn from some a priori defined distributions described by one of the parameters. For a detailed description of the Bayesian inference method, we refer the reader to the standard textbooks about statistical methods (Gelman et al., 2004; Kruschke, 2011; Wakefield, 2013).

In the following we will describe the construction of the Bayesian model, using the standard statistical notation. We describe how quantities are conditionally related, such that $x|y$ refers to a variable x given a value of y. Characterising values and their distribution, like $x|\mu,\, \sigma^2 \sim \mathcal{N}\left(\mu,\, \sigma^2\right)$ denotes that x is drawn from a normal distribution

$$\mathcal{N}\left(x|\mu,\, \sigma^2\right) = \frac{1}{\sqrt{2\pi}\sigma} \exp\left(\frac{-(x-\mu)^2}{2\sigma^2}\right)\,, \tag{6.4}$$

---

[1]Hierarchical modelling is often referred to as "multi-level" or "random-effects" modelling (Gelman and Hill, 2007).

given the mean value μ and the variance σ^2. We also employ gamma distributions

$$\mathcal{G}(x|s,\,r) = \frac{r^s}{\Gamma(s)}x^{s-1}\exp\left(-rx\right), \tag{6.5}$$

for the inverse of the variance with s and r the shape and rate parameters, respectively, and Γ the gamma function. Before performing the fit we standardise the data, i.e. we transform it with

$$\widetilde{y} \equiv \frac{y - \mu_y}{\sigma_y}, \quad \widetilde{x} \equiv \frac{x - \mu_x}{\sigma_x}, \tag{6.6}$$

where μ and σ indicate the mean and the standard deviation. This has the advantages that we know exactly the parameter range over which we have to sample with the "hyperpriors" (see definition further below).

In a Bayesian model all quantities are drawn from some prior defined distributions. Therefore, we assume that the velocity power spectrum $P(k,t)$ follows a power law, i.e. a linear function in log-log space. Additionally, we include a scatter term $\delta_s(k_i, t_j)$, which measures the deviations from a perfect power law,

$$\log P(k_i, t_j) = A(t_j) + \log k_i * \zeta(t_j) + \delta_s(k_i, t_j). \tag{6.7}$$

This equation describes the relationship between the parameters on the individual level in the hierarchy. The intercept $A(t_j)$, the power-law index $\zeta(t_j)$ and the scatter $\delta_s(k_i,\,t_j)$ of each individual time snapshot t_j must be drawn from the prior conditional probability distributions

$$A(t_j)|\overline{A}, \overline{\sigma_A^2} \sim \mathcal{N}\left(\overline{A}, \overline{\sigma_A^2}\right), \tag{6.8}$$

$$\zeta(t_j)|\overline{\zeta}, \overline{\sigma_\zeta^2} \sim \mathcal{N}\left(\overline{\zeta}, \overline{\sigma_\zeta^2}\right), \tag{6.9}$$

$$\delta_s(k_i,\,t_j)|\sigma_\Delta^2(t_j) \sim \mathcal{N}\left(0, \sigma_\Delta^2(t_j)\right), \tag{6.10}$$

$$1/\sigma_\Delta^2(t_j)|\overline{s}, \overline{r} \sim \mathcal{G}\left(\overline{s}, \overline{r}\right). \tag{6.11}$$

The model uses normal distributions for the slope, intercept and the scatter and a gamma distribution for the inverse of the variance of the scatter term. The inverse of the variance is also called precision. We chose a gamma distribution for the precision of the scatter to have a really broad prior, as we would like to rely on the data and not the priors.

Those quantities that depend on t_j refer to individual time frames. For instance, $\zeta(t_j)$ is the slope of the time snapshot t_j whereas $\overline{\zeta}$ refers to the group slope of the whole dataset. The fitting results of each relationship

above depend on quantities from the higher group level of the hierarchy, i.e. describe the time-averaged behaviour of the power spectrum. The prior assumptions for this final level, which are called "hyperpriors", are

$$\overline{A} \sim \mathcal{N}\left(0, 10\right), \tag{6.12}$$

$$\overline{\zeta} \sim \mathcal{N}\left(0, 100\right), \tag{6.13}$$

$$1/\overline{\sigma_A^2} \sim \mathcal{G}\left(0.1, 0.1\right), \tag{6.14}$$

$$1/\overline{\sigma_\zeta^2} \sim \mathcal{G}\left(0.1, 0.1\right), \tag{6.15}$$

$$\overline{s}|m, d = m^2/d^2, \tag{6.16}$$

$$\overline{r}|m, d = m/d^2, \tag{6.17}$$

$$m \sim \mathcal{G}\left(1, 0.1\right), \tag{6.18}$$

$$d \sim \mathcal{G}\left(1, 0.1\right). \tag{6.19}$$

The model contains the mean, m, and standard deviation, d, of the scatter term, as they are more intuitive than the shape and rate parameters of the gamma distribution. The mean μ and variance σ^2 of a gamma distribution with shape s and rate r is defined as, $\mu = s/r$ and $\sigma = s/r^2$, respectively.

Recall that we normalize the data with equation (6.6), so that the averaged intercept is zero and the standardized slope is just the correlation $corr(x, y) \in [-1 : 1]$. Therefore, we have broad "hyperpriors" in the model, such that the fixed values in (6.12)-(6.19), e.g. the group slope, is drawn from a normal distribution with mean $\mu = 0$ and $\sigma^2 = 100$. All values in (6.12)-(6.19) do affect the number of samples until the Markov Chain Monte Carlo method converges, but assuming sufficient sampling and that the "true" values lie inside the priors, they do not affect the end results of the Bayesian inference. For a more detailed description of the construction of a Bayesian model we refer the reader to standard textbooks of statistical data analysis (Gelman et al., 2004; Kruschke, 2011; Wakefield, 2013) or recent publications using similar models (Kelly, 2007; Shetty et al., 2013, 2014).

In summary, this Bayesian method explicitly treats the common fitting issues mentioned in the last Section. That is, variations of the scaling exponents with time yield a larger variance of the group slope. Fluctuations of the scaling exponents with k increase the group scatter $\sigma_\Delta^2(t_j)$. Variations and uncertainties of the measured data are also treated self-consistently. Both individual and also the global parameters are estimated simultaneously, avoiding any data-averaging. Since defining a fitting range introduces a large uncertainty, we test the Bayesian model on synthetic data in the next Section, where we fit over a k range of seven points to obtain the "local" slope of the power spectrum.

6.4 Test with synthetic data

We verify the hierarchical Bayesian model with synthetic data and compare it with normal linear regression (LR) methods. We create a synthetic dataset with 121 realisations according to the Bayesian model (equations $(6.7)-(6.11)$), where the group intercepts, the slopes and the scatter-precision follow distributions with mean values of $(5, -2, 1000)$ and standard deviations of $(1, 0.4, 200)$. These parameters for creating the synthetic data reflect the averaged behaviour of the measured power spectra in log-log space, where we slightly overestimate the variation in time. The synthetic data are distributed logarithmically on the x-axis instead of homogeneously distributed, as we will apply the methods in log-log space. Figure 6.2 shows the slope measured in a fitting range $\Delta k = 6$ (with seven points) as a function of the point in the centre of the fitting range for different methods. As we fixed the size of the fitting range in linear space its width is decreasing with k in log space, which we will discuss further below. The hierarchical model rigorously accounts for a number of uncertainties. The posterior probability distribution function (PDF) contains the resulting fit parameters, for both the group and the individuals. For example, the width of the PDF, or highest density interval (HDI), of the group slope and intercept yields the range in plausible parameters, considering the measurement uncertainty or insufficient statistics, caused by fitting only seven points.

Figure 6.2 shows estimates for two different parameters of the synthetic data. The group slope of the spectra with a 2σ-HDI uncertainty estimate, as well as the 1σ variation of the slopes with time without an uncertainty estimate. The green circles correspond to the Bayesian measurement of the group slope $\overline{\zeta}$ (the mean value in equation 6.9 and 6.13) and its 2σ-HDI interval (green, solid, thick lines), whereas the grey, dashed, thin lines quantify the variations of the slope in time using the maximum likelihood value of the standard deviation $\overline{\sigma_\zeta}$ in equation (6.9) and (6.14). To mimic hierarchical modelling using a normal linear regression we perform a fit on each individual time realisation and collect the slopes and error estimates in two histograms. The mean value of the resulting histogram with 121 error estimates gives a measurement of the averaged error of the fits (yellow, solid, thick lines). The mean value of the resulting histogram with 121 slopes provides an estimate of the group slope (blue squares) and its 1σ-HDI measures the variation in time (blue, dashed, thin lines). The red crosses correspond to a normal linear regression method applied to the spectra averaged in log space.

All methods in Figure 6.2 have a comparable accuracy for estimating the maximum likelihood slope, which does not depend on the scale in the shown range, whereas the error estimates are significantly different. With
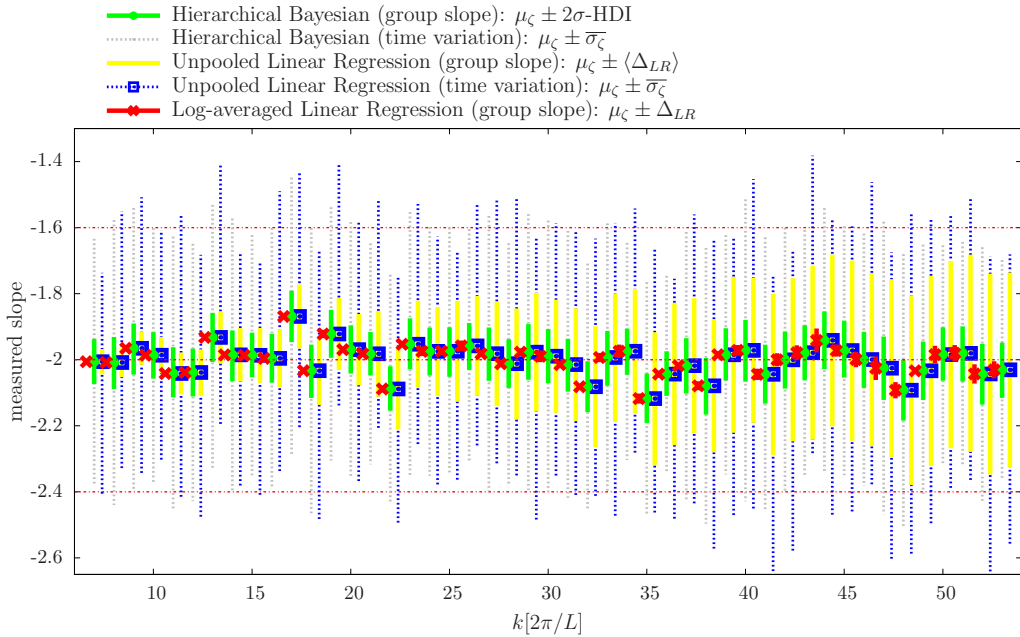
Figure 6.2: Test on synthetic data with a slope of -2 and time variation of 0.4 (indicated by the horizontal dashed-dotted lines). The ordinate indicates estimates of the group slope, from three different methods, over an extent of $\Delta k = 6$, plotted with the centre value of k on the abscissa . We compare the Hierarchical Bayesian, an unpooled linear regression to mimic hierarchical modelling with ordinary linear regression, and an ordinary linear regression applied to the spectra averaged in log-space. With the former two methods we estimate the variation of the slope with time (dashed thin lines) as well as the uncertainty of the group slope (thick solid lines). The results of the log-averaged linear regression is shifted slightly to the left, whereas these of the unpooled method are slightly shifted to the right for clarity. The creation of the synthetic data and the employed methods are discussed in more detail in Section 6.4.

normal linear regression applied to the log-averaged spectra, in nearly all cases (71%) the true slope lies outside the error interval (the red crosses are in most cases larger than the uncertainty intervals). Alternatively, the error estimates of the 'unpooled' linear regression (yellow, solid, thick) contain the correct value in all but one case, and the Bayesian method (green, solid, thick) contain the correct value in 92% of all cases. The uncertainty interval of the unpooled linear regression should contain the correct value in $68\% = 1\sigma$, as we calculate it with the mean value of the histogram of the individual errors. It increases systematically with k, which is due to an interplay of the decreasing width of the fitting range with k in log space and the increasing importance of the scatter with k, making this method impractical for a high precision measurement of the scaling exponent of the power-spectrum. On the other hand, both the unpooled linear regression model (blue, dashed, thin) as well as the hierarchical Bayesian model (grey, dashed, thin) recover the variation with time of the group slope of 0.4.

Figure 6.2 indicates that the regression method can have a major influence on the results, especially the error estimate, and should be chosen carefully. The ordinary linear regression applied to the averaged spectrum stand out negatively, as its error estimate of the mean slope totally fails. The implementation of a method to mimic hierarchical modelling using a normal χ^2-linear regression can recover the time variation of the group slopes, but its measurement of the averaged error between the individuals cannot be used to quantify the uncertainty of the group slope, as it strongly depends on the scale k and gets too large to distinguish between the different theoretical models. This is caused by an interplay of two effects. First, as we assume a fixed distribution for the scatter the relative importance of the scatter increases with k, which the unpooled linear regression cannot handle. Second, as we fix the fitting range in linear space, but fit in log-log space the effective width of the fitting range decreases with k, influencing the error estimate for the unpooled linear regression method. The Bayesian method, on the other hand, recovers all information about the slope with a high precision and valid error estimates.

6.5   The velocity power spectrum in numerical simulations

Figure 6.3 shows the total spectra for solenoidal (orange) and compressive (purple) forcing, compensated with k^2, and for the simulation with 1024^3 resolution. It clearly indicates that the compressive forcing yields a spec-
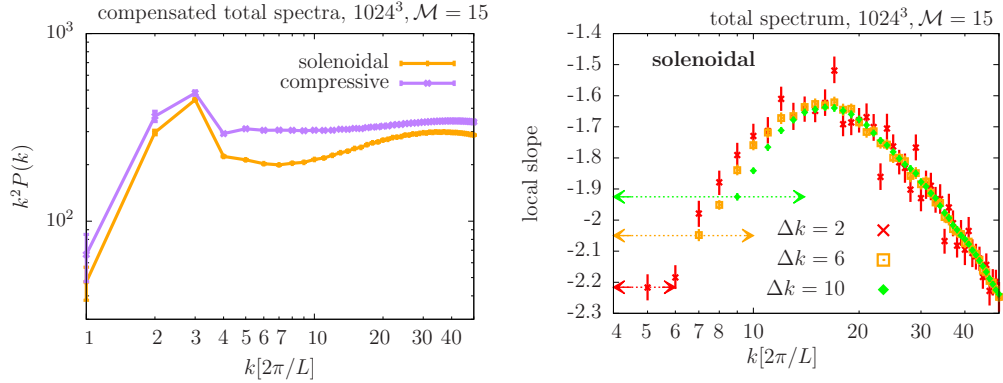
Figure 6.3: Left: Total spectra for solenoidal (orange) and compressive (purple) forcing, compensated with k^2, and 1024^3 resolution. Right: Measured local group slope of the Bayesian method as a function of the window centre k for three different fitting window sizes $\Delta k = 2, 6, 10$ (red, orange, green) performed on the total spectrum of the simulation with 1024^3 grid points and solenoidal forcing.

trum following the Burgers prediction over an extended range, whereas the solenoidal forcing yields a curved spectrum. The bump of energy at intermediate scales $k \approx 20 - 40$ is caused by a phenomenon normally known as the bottleneck effect (e.g. Dobler et al., 2003; Schmidt et al., 2006; Donzis and Sreenivasan, 2010). We will discuss its influence on the spectra in detail further below using the Bayesian estimate of the scaling exponent.

Next, we test how the extent of the fitting range influences the measured scaling exponents. We do this on the measured spectra instead of synthetic data and therefore use the simulation with solenoidal forcing and 1024^3 resolution. Figure 6.3 shows the measured group slope $\overline{\zeta}(k)$ as a function of the centre of the fitting range k for three different widths of the fitting range $\Delta k = 2, 6, 10$ (thereby including 3, 7, 11 points). Increasing the fitting range decreases the uncertainty in the measured scaling exponent. It also averages the high-frequency scatter out, without changing the global functionality on k. On low k values the measurements with small fitting windows estimate steeper slopes. But this is not a systematic error included by the small fitting ranges. It can be explained by the changing slopes of the power spectra in the given ranges. We indicate the k ranges of the different fitting windows on the first point of each measurement as a horizontal dashed line. The fitting ranges of all measurements start at $k = 4$, where the forcing routine has no direct influence any more. Figure 6.3 shows that the spectrum is strongly curved with a steep area at low wave numbers and gets systematically shal-
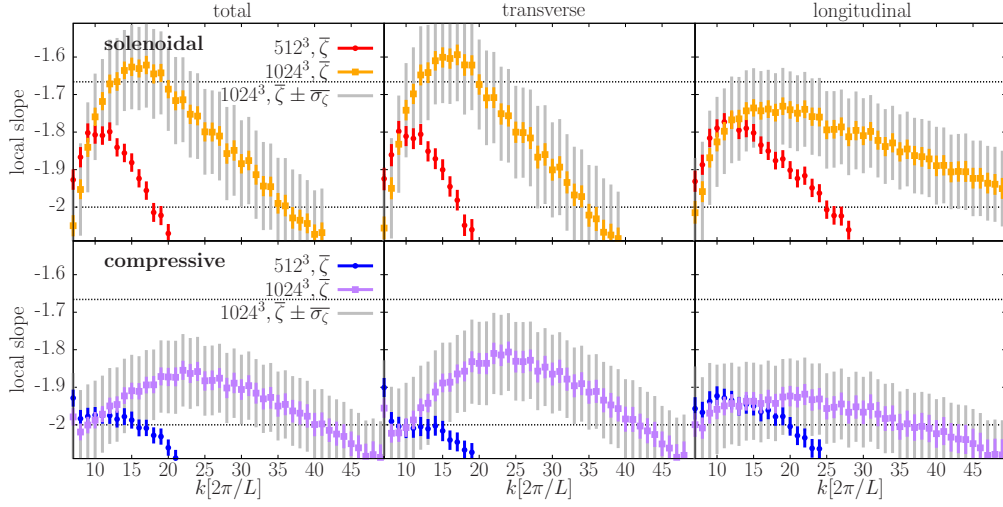
Figure 6.4: Local group slope as a function of the centre of the fitting window k with a size of $\Delta k = 6$ applied to the total (left), transverse (middle), and longitudinal (right) spectra of the simulations with 512^3, 1024^3 resolution (red/orange and blue/purple), solenoidal (upper panels) and compressive (bottom panels) forcing. The grey error bars indicate the time variation of the slope at each k for the 1024^3 simulations. The horizontal dotted lines indicate Kolmogorov $-5/3$ scaling and a Burgers -2 scaling behaviour.

lower with increasing k. So the steep part at small scales $k \approx 5$ influences the first measurement of the $\Delta k = 10$ curve at $k = 9$ (first green measurement), whereas the measurement with $\Delta k = 2$ at $k = 9$ is only influenced by the slope in $k \in (8 : 10)$ and is therefore systematically shallower (fifth red point). Figure 6.3 indicates that the scaling exponents of the solenoidal run span the whole range of theoretical predictions in the scale range $k \in (5 : 15)$.

Figure 6.4 shows the local group slope measured with window size $\Delta k = 6$ as a function of the centre of the fitting range k for solenoidal (upper panels) and compressive forcing mechanism (bottom panels), each for different resolutions 512^3 and 1024^3 (red/orange and blue/purple, respectively), and from left to right the local slope of the total, transverse and longitudinal decomposed spectra. The grey error bars indicate the time variation of the slope at each k only for the 1024^3 simulations. As we measure k in units of $2\pi/L$ with constant L for different resolution, the spectra should overlap on the large scales (low k). The spectra with 512^3 and 1024^3 resolution deviate from each other already on the large scales, indicating that they are not converged with resolution. All spectra are curved in the displayed range with a slope of ≈ -2 at large scales close to the forcing routine, a shallow area at
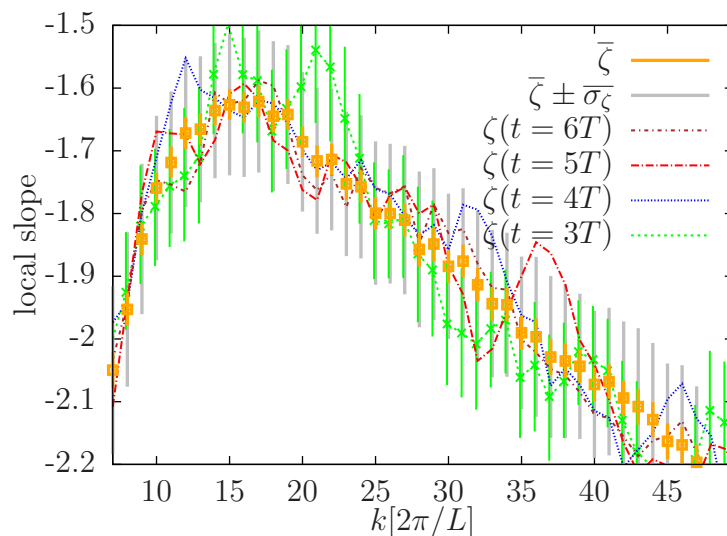
Figure 6.5: Same as in the left, upper panel of figure 6.4. In addition, we show the estimates of the slope in the individual times $t \in (3, 4, 5, 6)[T]$ to illustrate the high time variation. We provide only the uncertainty interval of the $t = 3[T]$ individual slope estimation and skip these for the other times for clarity.

intermediate scales, and systematically decreasing slopes in the range, where the numerical dissipation can no longer be neglected. This "bump" is more pronounced for the transverse spectra than for the longitudinal and is still increasing with resolution. Its peak appears for solenoidal forcing on larger scales and with shallower slopes than for compressive forcing. The longitudinal spectrum in the simulation with compressive forcing is the only case with a constant slope over an extended range $k \in (10 : 32)$, which corresponds to 102, 32 grid cells. Applying the Bayesian model to this range produces a group slope $\overline{\zeta} = -1.94$ with the small 2σ-HDI $[-1.95 : -1.93]$ and a standard deviation for the time variations $\overline{\sigma_\zeta} = 0.04$.

The simulation data indicate large temporal variations of the slopes ζ with variance $\overline{\sigma_\zeta} \approx 0.1 - 0.2$ (grey error bars in figure 6.4) for a window size of $\Delta k = 6$, which is independent of the forcing, k scale, and the mode of the analysed spectra. Increasing the fitting range decreases the temporal fluctuations (compare with the fit results $k \in (10 : 32)$ for the longitudinal spectrum and compressive forcing stated above). Figure 6.5 shows the same as the left, upper panel of figure 6.4, but in addition it provides the estimates of the individual slopes at the times $t \in (3, 4, 5, 6)[T]$ to illustrate the

fluctuations of the slope ζ for different times.

6.6 Discussion and interpretation

The measurements show that the power spectra are curved and not converged at a resolution of 512^3 and 1024^3 grid cells. An accumulation of kinetic energy just before the dissipation wave number is a phenomenon called "bottleneck effect" (e.g. Dobler et al., 2003; Schmidt et al., 2006; Donzis and Sreenivasan, 2010). We interpret the bump in the slopes as an influence of a numerical, non-physical bottleneck effect for several reasons. First, its peak appears in a region where we expect the bottleneck effect to occur (Donzis and Sreenivasan, 2010). Second, the height of the bump is still varying with resolution. And third, we rely on numerical dissipation. The bottleneck effect peaks at $k = 16, 23$ for the 1024^3 simulations with solenoidal and compressive forcing, respectively. It is more pronounced in the transverse than in the longitudinal spectrum indicating that the dissipation of the transverse modes of the velocity field is fainter than of the longitudinal modes. Increasing the number of shocks in a simulation by changing the forcing modes from solenoidal to compressive at constant Mach number decreases the amplitude of the bottleneck effect. We interpret this with the non-local energy flux through the scales introduced by shocks, which allows the flow to jump over a range of scales instead of transporting it steadily through the scales. However, a detailed study of the energy fluxes of the different velocity modes is necessary to validate this interpretation.

The reason for the large fluctuations in the slope ζ measured at different times can be explained as follows. Employing a constant forcing amplitude in (3.4) fixes the resulting Mach number only in a statistical sense. The actual energy and and momentum injection varies with time depending on the correlation of the density field and the forcing field. If the forcing pattern overlaps by chance with a high density region, more energy gets injected, causing time fluctuations in the velocity field. These are visible on the power spectra yielding the variations of the slopes with time.

6.7 Summary

We introduced a hierarchical Bayesian method for estimating the scaling exponent of the velocity power spectrum. We validated it on synthetic data and compared it with ordinary linear regression models applied to the log averaged power spectrum and an unpooled linear regression method to mimic

hierarchical modelling. We demonstrate that the ordinary linear regression model, applied to the averaged spectra, produces parameter estimates that fail to recover the underlying slope $\approx 70\%$ of the time, within the 2σ uncertainties. With the unpooled linear regression method the time variation of the slope can be accurately recovered, but the error estimate of the mean slope systemically increases with the scale k up to ≈ 0.2 at $k = 30$. The hierarchical Bayesian method avoids the caveats of the linear regression methods and can recover the underlying mean behaviour of the power spectrum, its time variation, as well as all errors and uncertainties estimates on these quantities. Therefore, the Bayesian method provides more information, and because of the correct error estimate, more robust parameter estimates of the power spectrum. Additionally, we implemented a routine to apply the hierarchical Bayesian method to fitting windows, where we change the sizes and placements systematically, to estimate the uncertainty caused by defining a fitting range.

To demonstrate the improvements of such an analysis we applied it to a "standard" simulation setup for analysing supersonic turbulence (e.g. Federrath et al., 2010; Kritsuk et al., 2007). The simulations have 1024^3 resolution, a root mean square Mach number of $\mathcal{M} \approx 15$, large scale forcing field (decomposed in solenoidal and compressive modes), an isothermal equation of state and artificial numerical dissipation. Our findings are:

1. The resolution study with 512^3 and 1024^3 showed that the spectra are still varying significantly and are not converged with resolution.

2. Independent of the forcing mechanism, we can rule out with $2\sigma = 95\%$ certainty that neither the total, nor the transverse spectra show an extended range where the power spectra stay constant. They start at $k = 4$ with a slope of ≈ -2 for solenoidal (compressive) forcing, reach a bump with shallower slopes of $\approx -1.6\,(-1.8)$ at intermediate scales $k \approx 16\,(23)$ and get systematically steeper in the dissipation range.

3. We interpret the bump in the slopes as numerical, non-physical bottleneck effect caused by the artificial numerical dissipation. The bottleneck bump is more pronounced and appears on larger scales in the transverse spectra in comparison with the longitudinal spectra.

4. We find that the forcing method has a more dominant influence on the longitudinal spectra, such that the solenoidal forcing yields the same curved spectrum and the compressive one yields a spectrum with a constant slope in the range $k \in (10 : 32)$ of -1.94 with the 2σ-HDI $-1.95 : -1.93$ and a standard deviation for the time variations $\overline{\sigma_\zeta} = 0.04$.

5. We measured the variation of the slope ζ with time $\overline{\sigma_\zeta} \approx 0.1 - 0.2$ for a window size of $\Delta k = 6$, which is independent of the forcing, k scale, and the mode of the analysed spectra. As observations measure only one time realisation of the power spectrum this uncertainty has to be taken into account.

Chapter 7

Summary and outlook

7.1 Summary

In this thesis, we performed a systematic analysis of the statistical properties of supersonic, isothermal turbulence. Turbulent flows occur on virtually all scales and in a variety of systems ranging from common incompressible terrestrial to highly supersonic and compressible flows. It arises in many astrophysical contexts, for instance, in the accretion disks of protoplanetary systems, in the interstellar medium, which is relevant for GMC and star formation, and in the intracluster medium (ICM). Supersonic turbulence is likely responsible for the complex and filamentary density structures observed in molecular clouds and influences the statistical occurrence of star formation. Despite of these applications, the theoretical understanding of compressible turbulence is still poor and analytical derivations are rare.

We studied a series of high-resolution, hydrodynamical grid simulations and examined the effects of solenoidal (divergence-free) and compressive (curl-free) forcing as well as varying Mach numbers on the parameters describing the statistical state of the system in both the Lagrangian and Eulerian frameworks. The probability density functions of the gas density, the velocity, and the velocity increments were measured. Structure functions and power spectra were investigated to quantify the two-point correlation properties of compressible turbulence and we compared the scaling exponents with intermittency models. Additionally, we employed a hierarchical Bayesian fitting method to estimate the parameters describing the scaling relationships of the velocity power spectra of supersonic turbulence and demonstrated the accuracy and other advantages of this technique compared with ordinary linear regression methods. We found that the mode of the forcing mechanism has an influence on all above mentioned measurements at a fixed root mean

square Mach number.

The study in Chapter 4 showed that the turbulent medium, driven by the compressive forcing, is more intermittent, has a larger fractal dimension of the most dissipative structures, and excites stronger head-on collisions and shock fronts, which shows a correlation between high density and low velocity, compared to the solenoidal driven medium. A comparison with simulations of incompressible turbulence shows that intermittency is stronger in a supersonic, compressible medium. Additionally, we found that the influence of the different forcings is stronger in the Eulerian than in the Lagrangian framework and that the Lagrangian framework exhibits a more intermittent behaviour than the Eulerian one.

Chapter 5 demonstrated that the solenoidal forcing yields a density PDF close to a log-normal distribution. In contrast, the compressive forcing yields distributions of the mass density that shows stronger deviations from the log-normal shape in the wings of the distribution. Compressive forcing yields density PDFs with std. dev.s proportional to the r.m.s. Mach number with $b = 1$, whereas solenoidal forcing yields $b = 1/3$. We found a unique relation between the std. dev. of the mass density and the compressible modes of the velocity field, which is independent of the driving mechanism and still holds in the subsonic regime, where the flow is mainly influenced by sound waves.

Chapter 6 revealed that compressive forcing yields steeper power spectra than solenoidal forcing. However, the turbulent power spectra are still varying significantly and are not converged with 512^3 and 1024^3 resolution at intermediate scales. Independent of the forcing mechanism, we can rule out that neither the total, nor the transverse spectra show an extended range where the power spectra stay constant. We found a 'bump' in the slopes at intermediate scales and interpreted it as the bottleneck effect. The bottleneck bump is more pronounced and appears on larger scales in the transverse spectra in comparison with the longitudinal spectra. Analysing the decomposed longitudinal spectra showed that the solenoidal forcing yields the same curved spectrum and the compressive one yields a spectrum with a constant slope.

7.2 Outlook

We present first two concrete ideas, how to proceed in the analysis of supersonic, isothermal turbulence, before we will discuss open questions concerning supersonic turbulence in the context of star formation.

The relation between the std. dev. of the density and the std. dev. of the longitudinal velocity (Chapter 5) suggests that these global one-point

statistical properties are not independent and can be expressed with only one parameter. If such a relation also exists for the two-point statistics, like power spectra or structure functions, the statistical properties of the density field are fully described by the velocity field. This means that a theory of compressible turbulence has to describe 'only' the properties of the transverse and longitudinal velocity fields. We showed in Chapter 4 and 5 that the velocity and the log-density in a turbulent flow are drawn from a normal distribution. By measuring the statistical parameters of the density and velocity distribution individually, what is normally done (see e.g. Federrath et al., 2010; Kritsuk et al., 2007; Konstandin et al., 2012a), one uses the assumption that these parameters are statistically independent distributed.

The Ansatz to model the global, one-point, statistical properties of isothermal, supersonic turbulent flow with a multivariate Gaussian (see Section 3.2.5 for the definition)

$$(\log(\rho), \mathbf{v}) \sim \mathcal{N}(\boldsymbol{\mu}, \boldsymbol{\Sigma}) , \tag{7.1}$$

can be implemented in a Bayesian framework, which does not contain the assumption that the parameters are independently distributed and measures the correlation of all parameters self-consistently. Isotropy leads to two independently random variables describing the statistical properties of the flow, the logarithm of density and the averaged velocity component $(\log(\rho), v_i)$. The study in Chapter 5 indicates a strong correlation between the longitudinal component of the velocity and the density field leading to the Ansatz $(\log(\rho), v_\perp, v_\parallel)$, which could also result in a two dimensional parameter space, if the longitudinal component and the log-density can be expressed by each other. The matrix $\mathbf{A}$ in (3.15) also plays in the interpretation an important role, as it contains the information of the basis vectors of the parameter space.

In order to express the statistical properties of a turbulent flow only with the $(v_\perp, v_\parallel)$ fields, we have to show that the correlation properties of the density field are a function of these variables and can be calculated. Therefore, we have to understand the velocity and density power spectra in detail. In the Appendix 8 we derive expressions for the energy fluxes occurring in supersonic turbulence. We introduce a new energy term measuring the amount of energy contained in the density field for the isothermal case. Measurements of these transfer functions in numerical simulations will provide informative insights in the dominant processes of supersonic turbulence.

Although supersonic turbulence is important for developing a theory of star formation, the interplay with other processes, like gravity, is not fully understood. There are many numerical studies of star formation in a turbulent medium with gravity (see Mac Low and Klessen, 2004; Federrath and

Klessen, 2012, and references therein), but they are either focusing on the influence of the turbulent properties on the statistical description of the star formation process or limited to one-point statistics such as the power-law tail of the density PDF in a self-gravitating system (Girichidis et al., 2013; Schneider et al., 2013). As far as we know, the influence of gravity on the turbulent properties, like the PDF of the velocity increments, their Gaussianity, and intermittency, is not well understood and a description of gravity in a turbulent framework is missing. Gravity adds another source term in the Euler equations, which will result in a different description of the density energy-reservoir yielding new energy fluxes between the gravitational potential and the kinetic energy. We plan on adding gravity to the theoretical description presented in Appendix 8 and investigate the influence on the energy transfer terms as well as the power spectra of the different energy reservoirs.

Glover et al. (2010a) showed that CO forms within a dynamical time scale, whereas the formation of H_2 typically needs more time (Glover et al., 2010b) and is more sensitive to the number density. Micic et al. (2012) pointed out that the H_2 formation is enhanced in a more shock dominated turbulent medium influencing the cooling rates of a fresh formed GMC. As the dynamical evolution of a cloud is rapid and the time scale is comparable to the time scale of most chemical processes, like the freez-out of molecules on the surface of dust grains, the dynamics and the chemistry of the gas are strongly coupled. The back reaction of this chemical network and the connected cooling processes on the statistical properties of the turbulence is not well understood and needs to be quantified further. In a first step we will analyse the influence of dropping the isothermal assumption and replacing it with a polytropic equation of state on the statistical properties. This adds another energy reservoir, the internal energy, with which the kinetic energy cascade can interact. The heating and cooling processes interact via the pressure term with the density and velocity field. This will change the kinetic energy spectrum and the correlation properties. A full chemical network will change this picture again, as the chemical processes depend strongly on the local temperature and density such that the heating and cooling (and the connected energy fluxes) correlate with regions of high densities and temperatures.

Chapter 8

Appendix: The energy fluxes in supersonic turbulence

The ideas presented here were developed together with J. Graham, R. Klessen, and W. Schmidt.

8.1 Energy fluxes of an incompressible medium

The inertial range in Kolmogorov phenomenology for an incompressible medium is intimately connected to the ideal invariant of kinetic energy. This can be shown with the Euler equation

$$\frac{\partial \mathbf{v}}{\partial t} + (\mathbf{v} \cdot \boldsymbol{\nabla}) \, \mathbf{v} + \frac{\boldsymbol{\nabla} p}{\rho} = 0 \,, \tag{8.1}$$

where $\mathbf{v}$ is the velocity field and $p = c_s^2 \rho$ is the pressure of an isothermal gas. We neglected the forcing and the dissipation term and assume that the average energy input from the external forcing equals the average energy loss by the dissipation in the steady state. We derive the time evolution of the kinetic energy density $e_{inc} = v^2/2$, by taking the dot product of equation (8.1) with $\mathbf{v}$

$$\frac{\partial e_{inc}}{\partial t} + \boldsymbol{\nabla} \left(\mathbf{v} e_{inc} \right) - e_{inc} \boldsymbol{\nabla} \cdot \mathbf{v} + \mathbf{v} \cdot \frac{\boldsymbol{\nabla} p}{\rho} = 0 \,, \tag{8.2}$$

where the third and fourth term vanish assuming incompressibility. Assuming a convenient boundary condition (e.g. fields, which converge to zero at infinity, or periodic fields) implies for a given vector field $\mathbf{f}$

$$\int_{\infty}^{\infty} \mathrm{d}\mathbf{r} \, \boldsymbol{\nabla}\mathbf{f} = 0 \,, \tag{8.3}$$

such that the total kinetic energy is conserved in the Kolmogorov framework

$$\frac{\partial e_{inc}}{\partial t} = 0\,. \tag{8.4}$$

The Fourier analogue of the energy equation (8.2) is the spectral energy density balance equation, which can be derived by Fourier transforming (8.1), assuming incompressibility, and multiplying the result with the complex conjugated velocity $\widehat{\mathbf{v}}^*(\mathbf{k})$

$$\frac{\partial \widehat{\mathbf{v}}(\mathbf{k}) \cdot \widehat{\mathbf{v}}^*(\mathbf{k})}{2\partial t} + \widehat{\mathbf{v}}^*(\mathbf{k}) \cdot [\widehat{(\mathbf{v} \cdot \boldsymbol{\nabla})\,\mathbf{v}}](\mathbf{k}) = 0 \tag{8.5}$$

where the first term is the time derivative of the spectral energy density and the second is the energy transfer function. Parseval's theorem guarantees that the spectral energy density integrates to the total energy. The transfer function is conservative, which can be shown with the Parseval's theorem and the Gauss theorem

$$\int_0^\infty \mathrm{d}\mathbf{k}\ \widehat{\mathbf{v}}(\mathbf{k})^* \cdot [\widehat{(\mathbf{v} \cdot \boldsymbol{\nabla})\,\mathbf{v}}](\mathbf{k}) \tag{8.6}$$

$$= \int_0^\infty \mathrm{d}\mathbf{r}\ \boldsymbol{\nabla}\,(\mathbf{v}e_{inc}) - e_{inc}\boldsymbol{\nabla} \cdot \mathbf{v} = 0\,, \tag{8.7}$$

and measures the rate of kinetic energy received at wave number k from exchange with all other wave numbers of kinetic energy.

8.2   Energy fluxes of a compressible medium

To derive the scale dependent energy distributions in isothermal, compressible turbulence we start with the Euler equation

$$\frac{\partial \rho\mathbf{v}}{\partial t} + (\mathbf{v} \cdot \boldsymbol{\nabla})\,\rho\mathbf{v} + \rho\mathbf{v}\,(\boldsymbol{\nabla} \cdot \mathbf{v}) = -c_s^2\boldsymbol{\nabla}\rho\,. \tag{8.8}$$

Adding (8.1) multiplied with $1/2\rho\mathbf{v}$ and (8.8) with $1/2\mathbf{v}$ results in an equation describing the time evolution of the kinetic energy density $e_K = 1/2\rho v^2$ in normal space

$$\partial_t e_K + \boldsymbol{\nabla}\,(\mathbf{v}e_K) = -c_s^2\mathbf{v} \cdot \boldsymbol{\nabla}\rho\,. \tag{8.9}$$

From this equations we can already conclude that the kinetic energy is no invariant, because of the pressure term $c_s^2\mathbf{v} \cdot \boldsymbol{\nabla}\rho$, which states that work against density gradients acts as a sink of kinetic energy.

To derive the spectral energy distribution we perform first the Fourier transformation of (8.1) and (8.8), then multiplying (8.1) with $1/2\widehat{(\rho\mathbf{v})}^*(k)$ and the complex conjugated (8.8) with $1/2\widehat{\mathbf{v}}(k)$, and adding the results gives

$$\partial_t E_K(k) = T_{KK}(k) + T_{SK}(k) \tag{8.10}$$

with

$$E_K(k) = \frac{1}{2}\widehat{\rho\mathbf{v}}^*(k) \cdot \widehat{\mathbf{v}}(k)\,, \tag{8.11}$$

$$
\begin{aligned}
T_{KK}(k) = & -\frac{1}{2}\widehat{(\rho\mathbf{v})}^*(k) \cdot [\widehat{(\mathbf{v} \cdot \boldsymbol{\nabla})\,\mathbf{v}}](k) \\
& -\frac{1}{2}\widehat{\mathbf{v}}(k) \cdot [\widehat{(\mathbf{v} \cdot \boldsymbol{\nabla})\,\rho\mathbf{v}}]^*(k) \\
& -\frac{1}{2}\widehat{\mathbf{v}}(k) \cdot [\widehat{\rho\mathbf{v}\,(\boldsymbol{\nabla} \cdot \mathbf{v})}]^*(k)\,,
\end{aligned}
\tag{8.12}
$$

$$T_{SK}(k) = -\frac{c_s^2}{2}\widehat{\rho\mathbf{v}}^*(k) \cdot \widehat{\boldsymbol{\nabla}s}(k) - \frac{c_s^2}{2}\widehat{\mathbf{v}}(k) \cdot \widehat{\boldsymbol{\nabla}\rho}^*(k)\,. \tag{8.13}$$

$E_K(k)$ is the spectral kinetic energy distribution, $T_{KK}(k)$ is the energy transfer of kinetic energy from all other wave numbers to E_K at k, and T_{SK} is the transfer from the density field to the kinetic energy at k. The energy transfer T_{KK} is conservative

$$\int_0^\infty d\mathbf{k}\; T_{KK} = \int_0^\infty d\mathbf{r}\; \boldsymbol{\nabla}\,(\mathbf{v}e_K) = 0\,, \tag{8.14}$$

whereas T_{SK} is not. We can write the scale-by-scale cumulative kinetic energy equation

$$\partial_t \mathcal{E}(k) + \Pi_{KK}(k) + \Pi_{SK}(k) = 0\,, \tag{8.15}$$

where the cumulative spectral energy is defined as,

$$\mathcal{E}(k) = \int_0^k d\mathbf{k'}\; E_K(\mathbf{k'})\,, \tag{8.16}$$

and similar definitions for the fluxes. The assumptions of a constant energy flux in the steady state in the inertial range $\epsilon = const$ results in

$$\epsilon \approx \Pi_{KK}(k) + \Pi_{SK}(k)\,. \tag{8.17}$$

If it turns out that $\Pi_{SK}(k) \ll \Pi_{KK}$ for some range in k we have

$$\epsilon \approx \Pi_{KK}(k) \sim \left\langle \boldsymbol{\nabla} \cdot \left(\mathbf{v}\rho v^2/2\right)\right\rangle \Rightarrow \epsilon = \rho\frac{v^3}{\ell}\,, \tag{8.18}$$

which is the result of Kritsuk et al. (2007); Galtier and Banerjee (2011). We now see the implicit assumption in this framework is that $T_{SK} \approx 0$ over the kinetic inertial range.

In the isothermal case the internal energy cannot be part of a conserved total energy equation, as energy must be removed from the system to keep the temperature constant. The internal energy is for a polytropic gas normally defined as $E_I = p/(\gamma - 1)$, which diverges for the isothermal case $\gamma = 1$. Therefore, we define a new energy

$$e_S = c_s^2 \rho \log\left(\frac{\rho}{\rho_0}\right) = c_s^2 \rho s \,, \tag{8.19}$$

which was already used in Galtier and Banerjee (2011) without any discussion. The energy in density fluctuations can be defined positive definite by the choice of ρ_0.

For the next step we write down the continuity equation

$$\frac{\partial}{\partial t}\rho + \boldsymbol{\nabla} \cdot (\rho \mathbf{v}) = 0 \,, \tag{8.20}$$

$$\frac{\partial}{\partial t}s + \mathbf{v} \cdot \boldsymbol{\nabla} s = -\boldsymbol{\nabla} \cdot \mathbf{v} \,. \tag{8.21}$$

First we Fourier transform (8.20) and (8.21), then we add (8.20) complex conjugated and multiplied with $c_s^2 \hat{s}(k)$ to (8.21) multiplied with $c_s^2 \hat{\rho}^*$, which results in

$$\partial_t E_S(k) = T_{SS}(k) + T_{KS}(k) \,, \tag{8.22}$$

where

$$E_S(k) = c_s^2 \hat{\rho}^*(k)\hat{s}(k) \,, \tag{8.23}$$

$$T_{SS}(k) = -c_s^2 \hat{\rho}^*(k)\widehat{\mathbf{v} \cdot \boldsymbol{\nabla} s}(k) - c_s^2 \hat{\rho}^*(k)\widehat{\boldsymbol{\nabla} \cdot \mathbf{v}}(k) \,, \tag{8.24}$$

$$T_{KS} = -c_s^2 \hat{s}(k)\left[\widehat{\boldsymbol{\nabla} \cdot \rho \mathbf{v}}\right]^*(k) \,. \tag{8.25}$$

The energy transfer in the density fluctuations is conservative

$$\int_0^\infty \mathrm{d}\mathbf{k}\, T_{SS} = \int_0^\infty \mathrm{d}\mathbf{r}\, \boldsymbol{\nabla}\left(\mathbf{v}p\right) = 0 \,, \tag{8.26}$$

whereas the transfer functions T_{KS} and T_{SK} are alone not conservative, together they built a conserved exchange of energy between the two reservoirs

$$\int_0^\infty \mathrm{d}\mathbf{k}\, T_{KS} + T_{SK} = \int_0^\infty \mathrm{d}\mathbf{r}\, \boldsymbol{\nabla}\left(\mathbf{v}e_S\right) = 0 \,. \tag{8.27}$$

Combining everything, we define the total energy

$$e_{total} = e_K + e_S \,, \tag{8.28}$$

which is a conserved quantity

$$\frac{\mathrm{d}e_{total}}{\mathrm{d}t} = \frac{\partial e_{total}}{\partial t} + \boldsymbol{\nabla} \left(\mathbf{v}(e_{total} + p)\right) = 0 \,, \tag{8.29}$$

and results in the spectral balance equation

$$\partial/\partial t \; E_{total}(k) = T_{KK}(k) + T_{SK}(k) + T_{KS}(k) + T_{SS}(k) \,. \tag{8.30}$$

With the definition of the cumulative transfer of energy describing the flux of energy through the scale k due to interaction between fluid motions and density fluctuations

$$\Pi_{SKS}(k) = - \int_0^k \mathrm{d}\mathbf{k'} \; T_{SK}(\mathbf{k'}) + T_{KS}(\mathbf{k'}) \,, \tag{8.31}$$

we can write down the scale-by-scale conserved flux of energy through the wave number k

$$\Pi_{total}(k) = \Pi_{KK}(k) + \Pi_{SS}(k) + \Pi_{SKS}(k) \,, \tag{8.32}$$

which is the total amount of energy transferred through the scale k and satisfies the Parseval-Gauss condition.

8.3   Energy fluxes of a compressible medium decomposed in curl field and source field

The Helmholtz theorem reads for the Fourier transformed velocity field

$$\widehat{\mathbf{v}}(\mathbf{k}) = \widehat{\mathbf{v}_\perp}(\mathbf{k}) + \widehat{\mathbf{v}_\parallel}(\mathbf{k}) \tag{8.33}$$

$$= \mathbf{k} \times \frac{1}{4\pi} \int \frac{\mathbf{k'} \times \widehat{\mathbf{v}}(\mathbf{k'})}{|k - k'|} \mathrm{d}^3 k' \tag{8.34}$$

$$- \mathbf{k} \frac{1}{4\pi} \int \frac{\mathbf{k'} \cdot \widehat{\mathbf{v}}(\mathbf{k'})}{|k - k'|} \mathrm{d}^3 k' \tag{8.35}$$

with the divergence-free, curl field, transversal component $\widehat{\mathbf{v}_\perp}(\mathbf{k})$ and the curl-free, gradient field, longitudinal component $\widehat{\mathbf{v}_\parallel}(\mathbf{k})$. The kinetic energy

E_K (8.11) can be decomposed in Fourier space

$$
\begin{aligned}
E_K(k) &= \frac{1}{2}\widehat{\rho\mathbf{v}}^{*}(k)\cdot\widehat{\mathbf{v}}(k)\\
&= \frac{1}{2}\left(\widehat{\rho\mathbf{v}}_{\perp}^{*}(k)+\widehat{\rho\mathbf{v}}_{\parallel}^{*}(k)\right)\cdot\left(\widehat{\mathbf{v}}_{\perp}(k)+\cdot\widehat{\mathbf{v}}_{\parallel}(k)\right)\\
&= \frac{1}{2}\widehat{\rho\mathbf{v}}_{\perp}^{*}(k)\cdot\widehat{\mathbf{v}}_{\perp}(k)+\widehat{\rho\mathbf{v}}_{\parallel}^{*}(k)\cdot\widehat{\mathbf{v}}_{\parallel}(k)\\
&= E_{K,\perp}(k)+E_{K,\parallel}(k)\,.
\end{aligned}
\tag{8.36}
$$

Fourier transforming equation (8.1) and (8.8), complex conjugate (8.8), and splitting the velocity in the transverse and longitudinal modes gives

$$
\left[\frac{\partial\left(\widehat{\mathbf{v}_{\perp}(\mathbf{k})+\mathbf{v}_{\parallel}(\mathbf{k})}\right)}{\partial t}\right]
$$
$$
+\left[(\mathbf{v}\cdot\boldsymbol{\nabla})\left(\widehat{\mathbf{v}_{\perp}(\mathbf{k})+\mathbf{v}_{\parallel}(\mathbf{k})}\right)\right]
$$
$$
+[-\widehat{c_s^2\boldsymbol{\nabla}s}]=0\,,
\tag{8.37}
$$

and

$$
\left[\frac{\partial\left(\widehat{\rho\mathbf{v}_{\perp}(\mathbf{k})+\rho\mathbf{v}_{\parallel}(\mathbf{k})}\right)}{\partial t}\right]^{*}
$$
$$
+\left[(\mathbf{v}\cdot\boldsymbol{\nabla})\left(\widehat{\rho\mathbf{v}_{\perp}(\mathbf{k})}+\rho\mathbf{v}_{\parallel}(\mathbf{k})\right)\right]^{*}
$$
$$
+\left[\left(\rho\mathbf{v}_{\perp}(\mathbf{k})+\widehat{\rho\mathbf{v}_{\parallel}(\mathbf{k})}\right)(\boldsymbol{\nabla}\cdot\mathbf{v})\right]^{*}
$$
$$
+[-\widehat{c_s^2\boldsymbol{\nabla}\rho}]^{*}=0\,.
\tag{8.38}
$$

where the square brackets indicate the terms, which have to be Fourier transformed. Now we take the dot product with the decomposed momentum $\frac{1}{2}\widehat{\rho\mathbf{v}}_{\perp}^{*}(\mathbf{k})$ and velocity $\frac{1}{2}\widehat{\mathbf{v}}_{\perp}^{*}(\mathbf{k})$ on (8.37) and (8.38). As the Fourier transformation of a sum can be divided into two terms we get after adding these equations

$$
\begin{aligned}
&\partial_t E_{K,\perp}(k)\\
&+\frac{1}{2}\widehat{\rho\mathbf{v}}_{\perp}^{*}(\mathbf{k})\partial_t\widehat{\mathbf{v}}_{\parallel}(\mathbf{k})\\
&+\frac{1}{2}\widehat{\mathbf{v}}_{\perp}(\mathbf{k})\partial_t\widehat{\rho\mathbf{v}}_{\parallel}^{*}(\mathbf{k})\\
&+T_{KK,\perp}+T_{KK,\perp\parallel}+T_{SK,\perp}=0\,,
\end{aligned}
\tag{8.39}
$$

with

$$T_{SK,\perp}(k) = -\frac{c_s^2}{2}\widehat{\rho\mathbf{v}_\perp}^*(k) \cdot \widehat{\boldsymbol{\nabla}s}(k) - \frac{c_s^2}{2}\widehat{\mathbf{v}}_\perp(k) \cdot \widehat{\boldsymbol{\nabla}\rho}^*(k) = 0 \,, \qquad (8.40)$$

which vanishes because the transverse velocity and momentum are perpendicular and the gradient fields are parallel to $\mathbf{k}$. For the energy flux in the transverse mode we get

$$\begin{aligned}
T_{KK,\perp}(k) = &- \frac{1}{2}\widehat{\rho\mathbf{v}}_\perp^*(k) \cdot [\widehat{(\mathbf{v} \cdot \boldsymbol{\nabla})\,\mathbf{v}_\perp}](k) \\
&- \frac{1}{2}\widehat{\mathbf{v}}_\perp(k) \cdot [\widehat{(\mathbf{v} \cdot \boldsymbol{\nabla})\,\rho\mathbf{v}_\perp}]^*(k) \\
&- \frac{1}{2}\widehat{\mathbf{v}}_\perp(k) \cdot [\widehat{\rho\mathbf{v}_\perp\,(\boldsymbol{\nabla} \cdot \mathbf{v})}]^*(k) \,, \qquad (8.41)
\end{aligned}$$

and for the energy flux between the modes

$$\begin{aligned}
T_{KK,\perp\|}(k) = &- \frac{1}{2}\widehat{\rho\mathbf{v}}_\perp^*(k) \cdot \left[\widehat{(\mathbf{v} \cdot \boldsymbol{\nabla})\,\mathbf{v}_\|}\right](k) \\
&- \frac{1}{2}\widehat{\mathbf{v}}_\perp(k) \cdot \left[\widehat{(\mathbf{v} \cdot \boldsymbol{\nabla})\,\rho\mathbf{v}_\|}\right]^*(k) \\
&- \frac{1}{2}\widehat{\mathbf{v}}_\perp(k) \cdot \left[\widehat{\rho\mathbf{v}_\|\,(\boldsymbol{\nabla} \cdot \mathbf{v})}\right]^*(k) \,. \qquad (8.42)
\end{aligned}$$

The flux $T_{KK,\perp}(k)$ is conservative

$$\int_0^\infty \mathrm{d}k \, T_{KK,\perp}(k) = \int_0^\infty \mathrm{d}r \, \boldsymbol{\nabla}\,(\mathbf{v}E_\perp) = 0 \,, \qquad (8.43)$$

whereas the flux $T_{KK,\perp\|}(k)$ is not. However, the sum of the fluxes $T_{KK,\perp\|}(k)$ and $T_{KK,\|\perp}(k)$ are conservative

$$\int_0^\infty \mathrm{d}k \, T_{KK,\perp\|}(k) + T_{KK,\|\perp}(k) = \int_0^\infty \mathrm{d}r \, \boldsymbol{\nabla}\,\left(\mathbf{v}\rho\mathbf{v}_\perp\mathbf{v}_\|\right) = 0 \,. \qquad (8.44)$$

The last missing step to derive the spectral energy balance equation is to discuss the mixed terms in (8.39). Because of orthogonality in Fourier space we can write

$$\begin{aligned}
&\widehat{\rho\mathbf{v}}_\perp^*(\mathbf{k})\partial_t\widehat{\mathbf{v}}_\|(\mathbf{k}) + \widehat{\mathbf{v}}_\perp(\mathbf{k})\partial_t\widehat{\rho\mathbf{v}}_\|^*(\mathbf{k}) \\
&= (-1)\left(\widehat{\rho\mathbf{v}}_\|^*(\mathbf{k})\partial_t\widehat{\mathbf{v}}_\perp(\mathbf{k}) + \widehat{\mathbf{v}}_\|(\mathbf{k})\partial_t\widehat{\rho\mathbf{v}}_\perp^*(\mathbf{k})\right) \,, \qquad (8.45)
\end{aligned}$$

showing its symmetry.

Bibliography

Anselmet, F., Gagne, Y., Hopfinger, E. J., and Antonia, R. A. (1984). High-order velocity structure functions in turbulent shear flows. *Journal of Fluid Mechanics*, 140:63–89.

Ballesteros-Paredes, J., Hartmann, L. W., Vázquez-Semadeni, E., Heitsch, F., and Zamora-Avilés, M. A. (2011a). Gravity or turbulence? Velocity dispersion-size relation. MNRAS, 411:65–70.

Ballesteros-Paredes, J., Klessen, R. S., and Vázquez-Semadeni, E. (2003). Dynamic Cores in Hydrostatic Disguise. ApJ, 592:188–202.

Ballesteros-Paredes, J., Vázquez-Semadeni, E., Gazol, A., Hartmann, L. W., Heitsch, F., and Colín, P. (2011b). Gravity or turbulence? - II. Evolving column density probability distribution functions in molecular clouds. MNRAS, 416:1436–1442.

Banerjee, S. and Galtier, S. (2013). Exact relation with two-point correlation functions and phenomenological approach for compressible magnetohydrodynamic turbulence. Phys. Rev. E, 87:013019.

Beck, C. (2004). Superstatistics in hydrodynamic turbulence. *Physica D Nonlinear Phenomena*, 193:195–207.

Beck, R. (1996). The influence of spiral arms on interstellar magnetic fields. *Nachr. Akad. Wiss. Göttingen II, Jahrg. 1996, Nr. 4, p. 262 - 270*, 1996:262–270.

Beetz, A., Gollwitzer, C., Richter, R., and Rehberg, I. (2008). Response of a ferrofluid to traveling-stripe forcing. *Journal of Physics Condensed Matter*, 20(20):204109.

Benzi, R., Biferale, L., Fisher, R., Lamb, D. Q., and Toschi, F. (2010). Inertial range Eulerian and Lagrangian statistics from numerical simulations of isotropic turbulence. *Journal of Fluid Mechanics*, 653:221–244.

Benzi, R., Ciliberto, S., Tripiccione, R., Baudet, C., Massaioli, F., and Succi, S. (1993). Extended self-similarity in turbulent flows. Phys. Rev. E, 48:29.

Bhatnagar, P. L., Gross, E. P., and Krook, M. (1954). A Model for Collision Processes in Gases. I. Small Amplitude Processes in Charged and Neutral One-Component Systems. *Physical review*, 94:511–525.

Bigiel, F., Leroy, A., Walter, F., Brinks, E., de Blok, W. J. G., Madore, B., and Thornley, M. D. (2008). The Star Formation Law in Nearby Galaxies on Sub-Kpc Scales. *TODO* ApJ, 136:2846–2871.

Birnir, B. (2013). The Kolmogorov-Obukhov Statistical Theory of Turbulence. *Journal of NonLinear Science*, 23:657–688.

Boldyrev, S., Nordlund, Å., and Padoan, P. (2002). Supersonic Turbulence and Structure of Interstellar Molecular Clouds. Phys. Rev. Lett., 89(3):031102.

Boltzmann, L. (1872). *Weitere Studien über das Wärmegleichgewicht unter Gasmolekülen.*

Brandenburg, A. and Subramanian, K. (2005). Astrophysical magnetic fields and nonlinear dynamo theory. Phys. Rep., 417:1–209.

Brunt, C. M. (2003). The Universality of Turbulence in the Molecular Interstellar Medium and Its Exploitation as a Distance Estimator. ApJ, 584:293–315.

Brunt, C. M. (2010). The density variance - Mach number relation in the Taurus molecular cloud. Å, 513:A67.

Brunt, C. M., Federrath, C., and Price, D. J. (2010). A method for reconstructing the variance of a 3D physical field from 2D observations: application to turbulence in the interstellar medium. MNRAS, 403:1507–1515.

Brunt, C. M., Heyer, M. H., and Mac Low, M.-M. (2009). Turbulent driving scales in molecular clouds. A&A, 504:883–890.

Burgers, J. (1948). *Advances in Applied Mechanics I.*

Burkhart, B., Falceta-Gonçalves, D., Kowal, G., and Lazarian, A. (2009). Density Studies of MHD Interstellar Turbulence: Statistical Moments, Correlations and Bispectrum. *The Astrophysical Journal*, 693:250–266.

Burkhart, B. and Lazarian, A. (2012). The Column Density Variance-Sonic Mach Number Relationship.

Burkhart, B., Stanimirović, S., Lazarian, A., and Kowal, G. (2010). Characterizing Magnetohydrodynamic Turbulence in the Small Magellanic Cloud. ApJ, 708:1204–1220.

Chapman, S. (1916). On the Law of Distribution of Molecular Velocities, and on the Theory of Viscosity and Thermal Conduction, in a Non-Uniform Simple Monatomic Gas. *Royal Society of London Philosophical Transactions Series A*, 216:279–348.

Chapman, S. and Cowling, T. G. (1970). *The mathematical theory of non-uniform gases. an account of the kinetic theory of viscosity, thermal conduction and diffusion in gases.*

Chen, S. Y., Dhruva, B., Kurien, S., Sreenivasan, K. R., and Taylor, M. A. (2005). Anomalous scaling of low-order structure functions of turbulent velocity. *Journal of Fluid Mechanics*, 533:183–192.

Choudhuri, A. R. (1998). *The physics of fluids and plasmas : An introduction for astrophysicists.* Cambridge University.

Colella, P. and Woodward, P. R. (1984). The Piecewise Parabolic Method (PPM) for Gas-Dynamical Simulations. *Journal of Computational Physics*, 54:174–201.

Dame, T. M., Hartmann, D., and Thaddeus, P. (2001). The Milky Way in Molecular Clouds: A New Complete CO Survey. ApJ, 547:792–813.

Dame, T. M., Ungerechts, H., Cohen, R. S., de Geus, E. J., Grenier, I. A., May, J., Murphy, D. C., Nyman, L.-A., and Thaddeus, P. (1987). A composite CO survey of the entire Milky Way. ApJ, 322:706–720.

De Morgan, A. and De Morgan, S. (1872). *A Budget of Paradoxes.*

Dekel, A. and Krumholz, M. R. (2013). Steady outflows in giant clumps of high-z disc galaxies during migration and growth by accretion. MNRAS, 432:455–467.

Dobbs, C. L., Krumholz, M. R., Ballesteros-Paredes, J., Bolatto, A. D., Fukui, Y., Heyer, M., Mac Low, M.-M., Ostriker, E. C., and Vázquez-Semadeni, E. (2013). Formation of Molecular Clouds and Global Conditions for Star Formation. Protostars and planets 6, Conference Series.

Dobler, W., Haugen, N. E., Yousef, T. A., and Brandenburg, A. (2003). Bottleneck effect in three-dimensional turbulence simulations. Phys. Rev. E, 68:026304.

Donzis, D. A. and Sreenivasan, K. R. (2010). The bottleneck effect and the Kolmogorov constant in isotropic turbulence. *Journal of Fluid Mechanics*, 657:171–188.

Dubey, A., Fisher, R., Graziani, C., Jordan, IV, G. C., Lamb, D. Q., Reid, L. B., Rich, P., Sheeler, D., Townsley, D., and Weide, K. (2008). Challenges of Extreme Computing using the FLASH code. In N. V. Pogorelov, E. Audit, & G. P. Zank, editor, *Numerical Modeling of Space Plasma Flows*, volume 385 of *Astronomical Society of the Pacific Conference Series*, page 145.

Dubrulle, B. (1994). Intermittency in fully developed turbulence: Log-Poisson statistics and generalized scale covariance. *Physical Review Letters*, 73:959–962.

Elmegreen, B. G. (2008). Variations in Stellar Clustering with Environment: Dispersed Star Formation and the Origin of Faint Fuzzies. *The Astrophysical Journal*, 672:1006–1012.

Elmegreen, B. G. and Scalo, J. (2004). Interstellar Turbulence I: Observations and Processes. ARA&A, 42:211–273.

Enskog, D. (1917). *Kinetische Theorie der Vorgaenge in maessig verduennten Gasen. I. Allgemeiner Teil.*

Federrath, C. and Klessen, R. S. (2012). The Star Formation Rate of Turbulent Magnetized Clouds: Comparing Theory, Simulations, and Observations. ApJ, 761:156.

Federrath, C., Klessen, R. S., and Schmidt, W. (2008). The Density Probability Distribution in Compressible Isothermal Turbulence: Solenoidal versus Compressive Forcing. ApJ, 688:L79–L82.

Federrath, C., Klessen, R. S., and Schmidt, W. (2009). The Fractal Density Structure in Supersonic Isothermal Turbulence: Solenoidal Versus Compressive Energy Injection. *The Astrophysical Journal*, 692:364–374.

Federrath, C., Roman-Duval, J., Klessen, R. S., Schmidt, W., and Mac Low, M. (2010). Comparing the statistics of interstellar turbulence in simulations and observations. Solenoidal versus compressive turbulence forcing. Å, 512:A81.

Foster, J. B., Mandel, K. S., Pineda, J. E., Covey, K. R., Arce, H. G., and Goodman, A. A. (2013). Evidence for grain growth in molecular clouds: A Bayesian examination of the extinction law in Perseus. MNRAS, 428:1606–1622.

Frisch, U. (1995). *Turbulence. The legacy of A. N. Kolmogorov.* Cambridge University.

Fryxell, B., Olson, K., Ricker, P., Timmes, F. X., Zingale, M., Lamb, D. Q., MacNeice, P., Rosner, R., Truran, J. W., and Tufo, H. (2000). FLASH: An Adaptive Mesh Hydrodynamics Code for Modeling Astrophysical Thermonuclear Flashes. *Astronomy and Astrophysics, Supplement*, 131:273–334.

Gaensler, B. M., Haverkorn, M., Burkhart, B., Newton-McGee, K. J., Ekers, R. D., Lazarian, A., McClure-Griffiths, N. M., Robishaw, T., Dickey, J. M., and Green, A. J. (2011). Low-Mach-number turbulence in interstellar gas revealed by radio polarization gradients. Nature, 478:214–217.

Gagne, Y. and Hopfinger, E. J. (1979). High order dissipation correlations and structure functions in an axisymmetric jet and a plane channel flow. In *2nd Symposium on Turbulent Shear Flows*, page 11.

Galtier, S. and Banerjee, S. (2011). Exact Relation for Correlation Functions in Compressible Isothermal Turbulence. *Physical Review Letters*, 107(13):134501.

Gelman, A., Carlin, J. B., Stern, H. S., and Rubin, D. B. (2004). *Bayesian Data Analysis, 2nd edn. Chapman & Hall.*

Gelman, A. and Hill, J. (2007). *Data analysis using regression and multilevel/hierarchical models.*

Girichidis, P., Konstandin, L., Whitworth, A. P., and Klessen, R. S. (2013). On the evolution of the density pdf in strongly self-gravitating systems. *TODO.*

Glover, S. C. O., Federrath, C., Mac Low, M.-M., and Klessen, R. S. (2010a). Modelling CO formation in the turbulent interstellar medium. MNRAS, 404:2–29.

Glover, S. C. O., Federrath, C., Mac Low, M.-M., and Klessen, R. S. (2010b). Simulating the chemistry and dynamics of molecular clouds. *Highlights of Astronomy*, 15:405–405.

Glover, S. C. O. and Mac Low, M.-M. (2007a). Simulating the Formation of Molecular Clouds. I. Slow Formation by Gravitational Collapse from Static Initial Conditions. ApJS, 169:239–268.

Glover, S. C. O. and Mac Low, M.-M. (2007b). Simulating the Formation of Molecular Clouds. II. Rapid Formation from Turbulent Initial Conditions. ApJ, 659:1317–1337.

Gotoh, T., Fukayama, D., and Nakano, T. (2002). Velocity field statistics in homogeneous steady turbulence obtained using a high-resolution direct numerical simulation. *Physics of Fluids*, 14:1065–1081.

Gurvitch, A. (1960). Experimental research on frequency spectra of atmospheric turbulence. *Tzv. Akad. Nauk SSSR*, 1042.

Hartmann, L., Ballesteros-Paredes, J., and Heitsch, F. (2012). Rapid star formation and global gravitational collapse. MNRAS, 420:1457–1461.

Hennebelle, P. and Audit, E. (2007). On the structure of the turbulent interstellar atomic hydrogen. I. Physical characteristics. Influence and nature of turbulence in a thermally bistable flow. A&A, 465:431–443.

Hennebelle, P. and Chabrier, G. (2008). Analytical Theory for the Initial Mass Function: CO Clumps and Prestellar Cores. *The Astrophysical Journal*, 684:395–410.

Hennebelle, P. and Chabrier, G. (2009). Analytical Theory for the Initial Mass Function. II. Properties of the Flow. *The Astrophysical Journal*, 702:1428–1442.

Hennebelle, P. and Chabrier, G. (2011). Analytical Star Formation Rate from Gravoturbulent Fragmentation. *The Astrophysical Journal, Letters*, 743:L29.

Heyer, M. H. and Brunt, C. M. (2004). The Universality of Turbulence in Galactic Molecular Clouds. ApJ, 615:L45–L48.

Hill, A. S., Benjamin, R. A., Kowal, G., Reynolds, R. J., Haffner, L. M., and Lazarian, A. (2008). The Turbulent Warm Ionized Medium: Emission Measure Distribution and MHD Simulations. ApJ, 686:363–378.

Hopkins, P. F. (2012). An excursion-set model for the structure of giant molecular clouds and the interstellar medium. MNRAS, 423:2016–2036.

Iannuzzi, F. and Dolag, K. (2012). On the orbital and internal evolution of cluster galaxies. MNRAS, 427:1024–1033.

Ishihara, T., Gotoh, T., and Kaneda, Y. (2009). Study of High - Reynolds Number Isotropic Turbulence by Direct Numerical Simulation. *Annual Review of Fluid Mechanics*, 41:165–180.

Kaneda, Y., Ishihara, T., Yokokawa, M., Itakura, K., and Uno, A. (2003). Energy dissipation rate and energy spectrum in high resolution direct numerical simulations of turbulence in a periodic box. *Physics of Fluids*, 15:L21–L24.

Karman, T. and Howarth, L. (1938). On the Statistical Theory of Isotropic Turbulence. volume 164, pages 192–215.

Kelly, B. C. (2007). Some Aspects of Measurement Error in Linear Regression of Astronomical Data. ApJ, 665:1489–1506.

Kelly, B. C., Shetty, R., Stutz, A. M., Kauffmann, J., Goodman, A. A., and Launhardt, R. (2012). Dust Spectral Energy Distributions in the Era of Herschel and Planck: A Hierarchical Bayesian-fitting Technique. ApJ, 752:55.

Kida, S. and Orszag, S. A. (1990). Energy and spectral dynamics in forced compressible turbulence. *Journal of Scientific Computing*, 5:85–125.

Kitsionas, S., Federrath, C., Klessen, R. S., Schmidt, W., Price, D. J., Dursi, L. J., Gritschneder, M., Walch, S., Piontek, R., Kim, J., Jappsen, A.-K., Ciecielag, P., and Mac Low, M.-M. (2009). Algorithmic comparisons of decaying, isothermal, supersonic turbulence. A&A, 508:541–560.

Klessen, R. S. (2000). One-Point Probability Distribution Functions of Supersonic Turbulent Flows in Self-gravitating Media. *The Astrophysical Journal*, 535:869–886.

Klessen, R. S. (2011). Star Formation in Molecular Clouds. In Charbonnel, C. and Montmerle, T., editors, *EAS Publications Series*, volume 51 of *EAS Publications Series*, pages 133–167.

Klessen, R. S., Ballesteros-Paredes, J., Vázquez-Semadeni, E., and Durán-Rojas, C. (2005). Quiescent and Coherent Cores from Gravoturbulent Fragmentation. *The Astrophysical Journal*, 620:786–794.

Klessen, R. S., Krumholz, M. R., and Heitsch, F. (2011). Numerical Star-Formation Studies - A Status Report. *Advanced Science Letters*, 4:258–285.

Kolmogorov, A. (1941a). The Local Structure of Turbulence in Incompressible Viscous Fluid for Very Large Reynolds' Numbers. *Akademiia Nauk SSSR Doklady*, 30:301–305.

Kolmogorov, A. N. (1941b). Dissipation of Energy in Locally Isotropic Turbulence. *Akademiia Nauk SSSR Doklady*, 32:16.

Kolmogorov, A. N. (1962). A refinement of previous hypotheses concerning the local structure of turbulence in a viscous incompressible fluid at high Reynolds number. *Journal of Fluid Mechanics*, 13:82–85.

Konstandin, L., Federrath, C., Klessen, R. S., and Schmidt, W. (2012a). Statistical properties of supersonic turbulence in the Lagrangian and Eulerian frameworks. *Journal of Fluid Mechanics*, 692:183–206.

Konstandin, L., Girichidis, P., Federrath, C., and Klessen, R. S. (2012b). A New Density Variance-Mach Number Relation for Subsonic and Supersonic Isothermal Turbulence. ApJ, 761:149.

Konstandin, L., Shetty, R., Girichidis, P., and Klessen, R. S. (2014). Hierarchical Bayesian analysis of the velocity power-spectrum in supersonic turbulence. *submitted to* MNRAS.

Kowal, G. and Lazarian, A. (2007). Scaling Relations of Compressible MHD Turbulence. *The Astrophysical Journal, Letters*, 666:L69–L72.

Kowal, G., Lazarian, A., and Beresnyak, A. (2007). Density Fluctuations in MHD Turbulence: Spectra, Intermittency, and Topology. *The Astrophysical Journal*, 658:423–445.

Kritsuk, A. G., Norman, M. L., Padoan, P., and Wagner, R. (2007). The Statistics of Supersonic Isothermal Turbulence. *The Astrophysical Journal*, 665:416–431.

Krumholz, M. R., Bate, M. R., Arce, H. G., Dale, J. E., Gutermuth, R., Klein, R. I., Li, Z.-Y., Nakamura, F., and Zhang, Q. (2014). Star Cluster Formation and Feedback.

Kruschke, J. K. (2011). *Doing bayesian data analysis: a tutorial with R and BUGS*. Elsevier, Amsterdam.

Larson, R. B. (1981). Turbulence and star formation in molecular clouds. MNRAS, 194:809–826.

Lemaster, M. N. and Stone, J. M. (2008). Density Probability Distribution Functions in Supersonic Hydrodynamic and MHD Turbulence. *The Astrophysical Journal, Letters*, 682:L97–L100.

Lemaster, M. N. and Stone, J. M. (2009). Dissipation and Heating in Supersonic Hydrodynamic and MHD Turbulence. ApJ, 691:1092–1108.

Lesieur, M. (1993). *Turbulence in fluids*. Fluid mechanics and its applications ; 1 ; Fluid mechanics and its applications. Kluwer.

Li, Y., Klessen, R. S., and Mac Low, M. (2003). The Formation of Stellar Clusters in Turbulent Molecular Clouds: Effects of the Equation of State. *The Astrophysical Journal*, 592:975–985.

Lorre, C., Prady, B., and Aronsohn, L. (2013). The Big Bang Theory, season 7, episode 16, minute 1:22. *Warner Bros.*

Mac Low, M. and Klessen, R. S. (2004). Control of star formation by supersonic turbulence. *Reviews of Modern Physics*, 76:125–194.

Mandelbrot, B. B. (1972). Possible refinement of the lognormal hypothesis concerning the distribution of energy dissipation in intermittent turbulence. In Rosenblatt, M. and van Atta, C., editors, *Statistical Models and Turbulence*, volume 12 of *Lecture Notes in Physics, Berlin Springer Verlag*, pages 333–351.

Maurer, J., Tabeling, P., and Zocchi, G. (1994). Statistics of Turbulence between Two Counterrotating Disks in Low-Temperature Helium Gas. *EPL (Europhysics Letters)*, 26:31–36.

Maxwell, J. C. (1860). *Illustration of the Dynamical Theory of Gases- Part I: On the Motions and Collisions of Perfecly Elastic Spheres*, volume 19-4. Taylor & Francis.

McKee, C. F. and Ostriker, E. C. (2007). Theory of Star Formation. *Annual Review of Astronomy and Astrophysics*, 45:565–687.

Meschiari, S. (2012). Planet Formation in Circumbinary Configurations: Turbulence Inhibits Planetesimal Accretion. ApJ, 761:L7.

Micic, M., Glover, S. C. O., Federrath, C., and Klessen, R. S. (2012). Modelling H_2 formation in the turbulent interstellar medium: solenoidal versus compressive turbulent forcing. MNRAS, 421:2531–2542.

Molina, F. Z., Glover, S. C. O., Federrath, C., and Klessen, R. S. (2012). The Density Variance–Mach Number Relation in Supersonic Turbulence: I. Isothermal, magnetised gas. *TODO*.

Mordant, N., Delour, J., Léveque, E., Arnéodo, A., and Pinton, J. (2002). Long Time Correlations in Lagrangian Dynamics: A Key to Intermittency in Turbulence. *Physical Review Letters*, 89(25):254502.

Mordant, N., Metz, P., Pinton, J.-F., and Michel, O. (2005). Acoustical technique for Lagrangian velocity measurement. *Review of Scientific Instruments*, 76(2):025105.

Nietzsche, F. (1883). *Also sprach Zarathustra - Ein Buch für alle und keinen*.

Obukhov, A. M. (1962). Some Specific Features of Atmospheric Turbulence. J. Geophys. Res., 67:3011.

Padoan, P. and Nordlund, Å. (2002). The Stellar Initial Mass Function from Turbulent Fragmentation. *The Astrophysical Journal*, 576:870–879.

Padoan, P. and Nordlund, Å. (2011). The Star Formation Rate of Supersonic Magnetohydrodynamic Turbulence. *The Astrophysical Journal*, 730:40.

Padoan, P., Nordlund, A., and Jones, B. J. T. (1997). The universality of the stellar initial mass function. *Monthly Notices of the Royal Astronomical Society*, 288:145–152.

Passot, T. and Vázquez-Semadeni, E. (1998). Density probability distribution in one-dimensional polytropic gas dynamics. *Physical Review E*, 58:4501–4510.

Passot, T., Vázquez-Semadeni, E. C., and Pouquet, A. (1994). *A turbulent model for the interstellar medium.*, page 246.

Pope, S. B. (2000). *Turbulent Flows*.

Price, D. J. and Federrath, C. (2010). A comparison between grid and particle methods on the statistics of driven, supersonic, isothermal turbulence. MNRAS, 406:1659–1674.

Price, D. J., Federrath, C., and Brunt, C. M. (2011). The Density Variance-Mach Number Relation in Supersonic, Isothermal Turbulence. *The Astrophysical Journal, Letters*, 727:L21.

Richardson, L. F. (1920). The Supply of Energy from and to Atmospheric Eddies. *Royal Society of London Proceedings Series A*, 97:354–373.

Richardson, L. F., Wagner, A., and Dietzius, R. (1922). An observational test of the geostrophic approximation in the stratosphere. *Quarterly Journal of the Royal Meteorological Society*, 48:328–341.

Scalo, J. and Elmegreen, B. G. (2004). Interstellar Turbulence II: Implications and Effects. *Annual Review of Astronomy and Astrophysics*, 42:275–316.

Schmidt, W., Federrath, C., Hupp, M., Kern, S., and Niemeyer, J. C. (2009). Numerical simulations of compressively driven interstellar turbulence. I. Isothermal gas. *Astronomy and Astrophysics*, 494:127–145.

Schmidt, W., Federrath, C., and Klessen, R. (2008). Is the Scaling of Supersonic Turbulence Universal? *Physical Review Letters*, 101(19):194505.

Schmidt, W., Hillebrandt, W., and Niemeyer, J. C. (2006). Numerical dissipation and the bottleneck effect in simulations of compressible isotropic turbulence. *Comp. Fluids*, 35:353–357.

Schneider, N., André, P., Könyves, V., Bontemps, S., Motte, F., Federrath, C., Ward-Thompson, D., Arzoumanian, D., Benedettini, M., Bressert, E., Didelon, P., Di Francesco, J., Griffin, M., Hennemann, M., Hill, T., Palmeirim, P., Pezzuto, S., Peretto, N., Roy, A., Rygl, K. L. J., Spinoglio, L., and White, G. (2013). What Determines the Density Structure of Molecular Clouds? A Case Study of Orion B with Herschel. ApJ, 766:L17.

Schneider, N., Csengeri, T., Hennemann, M., Motte, F., Didelon, P., Federrath, C., Bontemps, S., Di Francesco, J., Arzoumanian, D., Minier, V., André, P., Hill, T., Zavagno, A., Nguyen-Luong, Q., Attard, M., Bernard, J.-P., Elia, D., Fallscheer, C., Griffin, M., Kirk, J., Klessen, R., Könyves, V., Martin, P., Men'shchikov, A., Palmeirim, P., Peretto, N., Pestalozzi, M., Russeil, D., Sadavoy, S., Sousbie, T., Testi, L., Tremblin, P., Ward-Thompson, D., and White, G. (2012). Cluster-formation in the Rosette molecular cloud at the junctions of filaments. *Astronomy and Astrophysics*, 540:L11.

Schober, J., Schleicher, D., Federrath, C., Klessen, R., and Banerjee, R. (2012). Magnetic field amplification by small-scale dynamo action: Dependence on turbulence models and Reynolds and Prandtl numbers. Phys. Rev. E, 85(2):026303.

She, Z. and Leveque, E. (1994). Universal scaling laws in fully developed turbulence. *Physical Review Letters*, 72:336–339.

Shetty, R., Beaumont, C. N., Burton, M. G., Kelly, B. C., and Klessen, R. S. (2012). The linewidth-size relationship in the dense interstellar medium of the Central Molecular Zone. MNRAS, 425:720–729.

Shetty, R., Kelly, B. C., and Bigiel, F. (2013). Evidence for a non-universal Kennicutt-Schmidt relationship using hierarchical Bayesian linear regression. MNRAS, 430:288–304.

Shetty, R., Kelly, B. C., Rahman, N., Bigiel, F., Bolatto, A. D., Clark, P. C., Klessen, R. S., and Konstandin, L. K. (2014). Indications of a sub-linear and non-universal Kennicutt-Schmidt relationship. MNRAS, 437:L61–L65.

Sreenivasan, K. R. and Dhruva, B. (1998). Is There Scaling in High-Reynolds-Number Turbulence? *Progress of Theoretical Physics Supplement*, 130:103–120.

Stutzki, J., Bensch, F., Heithausen, A., Ossenkopf, V., and Zielinsky, M. (1998). On the fractal structure of molecular clouds. *Astronomy and Astrophysics*, 336:697–720.

Tassis, K. (2007). The star formation law in a multifractal ISM. *Monthly Notices of the Royal Astronomical Society*, 382:1317–1323.

Toschi, F. and Bodenschatz, E. (2009). Lagrangian Properties of Particles in Turbulence. *Annual Review of Fluid Mechanics*, 41:375–404.

van Atta, C. W. and Park, J. (1972). Statistical self-similarity and inertial subrange turbulence. In Rosenblatt, M. and van Atta, C., editors, *Statistical Models and Turbulence*, volume 12 of *Lecture Notes in Physics, Berlin Springer Verlag*, pages 402–426.

van Dyke, M. (1982). An album of fluid motion. *NASA STI/Recon Technical Report A*, 82:36549.

Vazquez-Semadeni, E. (1994). Hierarchical Structure in Nearly Pressure-less Flows as a Consequence of Self-similar Statistics. *The Astrophysical Journal*, 423:681.

Waagan, K., Federrath, C., and Klingenberg, C. (2011). A robust numerical scheme for highly compressible magnetohydrodynamics: Nonlinear stability, implementation and tests. *Journal of Computational Physics*, 230:3331–3351.

Wakefield, J. (2013). *Bayesian and frequentist regression methods.* Springer Series in Statistics.

Wilczek, M. (2010). *Statistical and Numerical Investigations of Fluid Turbulence.*

Wilczek, M., Daitche, A., and Friedrich, R. (2011). On the velocity distribution in homogeneous isotropic turbulence: correlations and deviations from Gaussianity. *Journal of Fluid Mechanics*, 676:191–217.

Xu, H., Ouellette, N. T., and Bodenschatz, E. (2006). Multifractal Dimension of Lagrangian Turbulence. Phys. Rev. Lett., 96:114503.

Danksagung

Allen voran bedanke ich mich bei Angelika Stau, die mich immer tatkräftig unterstützt hat und mir gerade beim Schreiben dieser Arbeit den Rücken freigehalten hat. Ohne sie wäre diese Arbeit nicht in dieser Form entstanden. Zudem bedanke ich mich bei meiner Familie und bei meinen Freunden für ihre verständnisvolle Unterstützung.

Für die ausgezeichnete Betreuung während meiner Zeit als Doktorand am Institut für Theoretische Astrophysik möchte ich mich bei Ralf S. Klessen sehr herzlich bedanken. Die vielseitigen Diskussionen mit ihm haben mein Bild der Sternentstehung und Turbulenz nachhaltig beeinflusst. Außerdem möchte ich mich für seine uneingeschränkte Unterstützung auch in schwierigen Entscheidungen bedanken.

Für die wertvollen Kommentare und Hilfestellungen zu einer Vorversion dieser Arbeit bedanke ich mich bei Rahul Shetty. Aber, ich bin vielen Kollegen für ihre Hilfe zu Dank verpflichtet. Die zahlreichen, informellen Diskussionen und der stete Austausch, der erst durch das herausragend gute Arbeitsklima am ITA ermöglicht wurde, haben mein Verständnis der relevanten Physik deutlich erweitert. Auch die Diskussionen mit meinen Koauthoren der Publikationen haben mich geprägt und ihnen gebührt besonderer Dank.

Für die gute Arbeitsatmosphäre am ITA muss ich mich bei unzähligen Personen bedanken. Meinen Bürokollegen, Christian, Jennifer, Johanna und Juan, möchte ich danken. Ich habe die Zeit mit ihnen in unserem Büro sehr genossen. Außerdem möchte ich der "Café-Moro-Gruppe", bestehend aus oben genannten und Jonathan, László, Rahul, und Volker, für die regen Gespräche während der Kaffeepausen danken. Ein besonderer Dank gebührt Philipp Girichids für die täglichen Diskussionen zur Strukturentstehung in astrophysikalischen Systemen und Hilfestellungen zu nachhaltiger Programmierung. Bei Rahul Shetty bedanke ich mich nicht nur für die tägliche Betreuung, sondern auch für die unzähligen Diskussionen auf Arbeits- und privater Ebene, die mich nachhaltig geprägt haben.

Sie alle haben mir eine schöne und erfolgreiche Zeit in Heidelberg beschert.